# Dissipative Atom Optics with
# Cold Metastable Helium Atoms

PROEFSCHRIFT

DOOR

ARMAND EUGÈNE ALBERT KOOLEN

GEBOREN TE HEERLEN

*aan mijn ouders*
*en aan Brigitte*

# Contents

# Chapter 1

# Introduction

## 1 Studying laser-atom interactions with an atomic beam setup

The simplest system for studying laser-atom interactions [1] consists of a single atom, initially residing in a carefully prepared quantum state, interacting with a well-defined light field. In general both energy and momentum can be transferred between the light field and the atom. Hence the influence of the light field on the atom is reflected by the change in the atom's internal (electronic) and external (motional) state. Many experimental techniques have been devised to observe these changes. The systems under consideration can often be described by a relatively simple Hamiltonian, allowing their dynamics to be accurately predicted by theory. Thus, many textbook "Gedanken experiments" are now experimentally accessible.

Usually a large experimental effort is required to prepare the atom in the desired initial quantum state. In particular, the multitude of laser cooling techniques [2], devised and refined over the last two decades, have enabled the production of atomic samples of unprecedented quality. Nowadays, laser cooled atomic beams [3], atomic clouds produced in a magneto-optical trap (MOT) [4], atomic fountains [5], and Bose-Einstein condensates (BEC) [6–9] are used to study laser-atom interactions.

Bose-Einstein condensation in a weakly interacting gas of rubidium atoms was first observed in 1995 [6]. Since then, many groups around the world have produced phase-coherent atomic samples in rubidium, sodium [7], lithium [8], and even hydrogen [9]. Recently, condensates have found their way into the field of atom optics [10], where their excellent properties (ultra-low temperature, high density and well-defined quantum state) are used to perform high-resolution experiments [11–15].

Laser-cooled atomic beams are often a good choice if the atoms need to have a relatively large and well-defined initial velocity ($> 50$ ms$^{-1}$) in the experiment. Furthermore, beam experiments can be performed in such a way that the atoms pass the light field one after the other. This is quite different from BEC experiments, where typically thousands or even millions of atoms are present in the light field at the same time. Especially in quantum optics experiments that use small high-Q
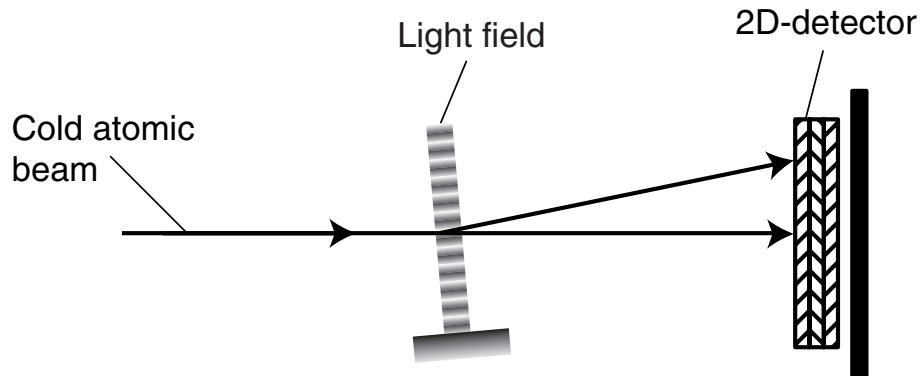
Figure 1.1: Schematic view of the setup used in the experiments described in this thesis. Atoms in the cold atomic beam are deflected by the light field, which is observed on a two-dimensional position-sensitive single-atom detector.

cavities, the simultaneous presence of more than one atom in the cavity alters the dynamics of the system considerably [16].

An atom that absorbs a photon from a light field can re-emit it by either spontaneous or stimulated emission. In spontaneous emission, the atom emits the photon in a random direction leading to a randomly directed recoil kick. Even the internal state of the atom after spontaneous decay can be a random variable. The process of absorption followed by spontaneous emission makes laser cooling possible, since it allows for dissipation of atomic kinetic energy. The corresponding force, known as the spontaneous radiation force, can therefore be used to cool atoms. Light fields that contain intensity gradients can also transfer net momentum to the atom through absorption/stimulated emission cycles. The corresponding force, known as the dipole force, does not contain a random component and can be used to coherently manipulate the motion of the atom. The dipole force is extensively used in the domain of atom optics.

In this thesis we will use an ultra-high precision metastable helium beam as a source of atoms, each of them carefully prepared in a well-defined electronic and motional quantum state. The transverse momentum distribution of the atoms in the beam is sub-recoil collimated, i.e., well below the momentum of a single 1083 nm photon. The beam is used to study the influence of both the dipole force and the spontaneous radiation force in detail. Specifically, we look at the angular distribution of spontaneous recoils (which mirror dipole radiation patterns) and at large-angle Bragg scattering of atoms from a standing light wave. For this purpose, we have placed a two-dimensional position-sensitive single-atom detector in the far-field that measures the change in transverse atomic momentum with sub-recoil precision. A schematic view of the setup, used in the experiments presented in this thesis, is shown in Fig. 1.1.

The atomic beam setup is constructed with a number of specific experiments in cavity Quantum Electrodynamics and atom optics in mind, including photon number measurements in optical cavities and atomic wavepacket tomography. These planned experiments will be briefly introduced at the end of this chapter.
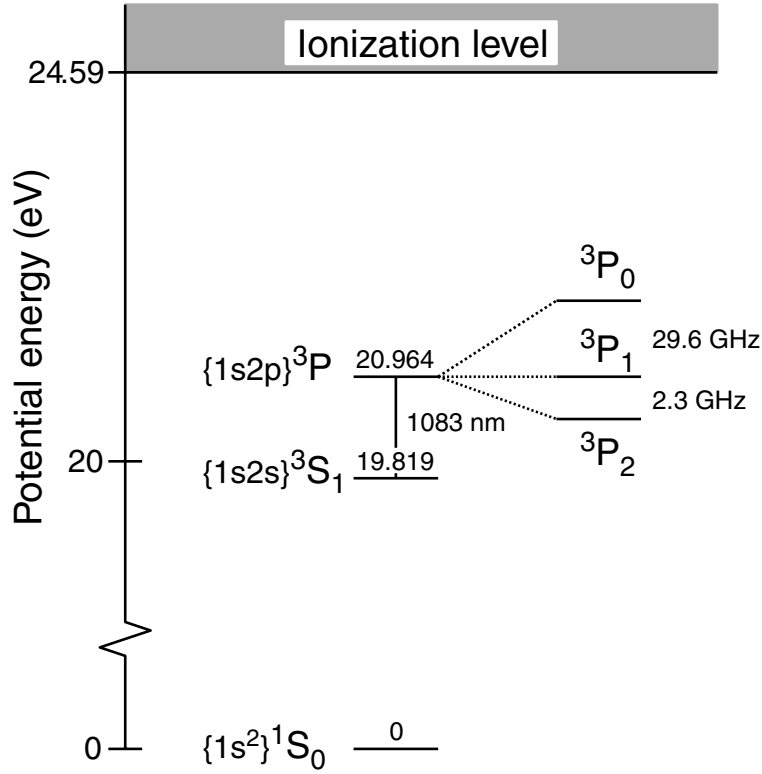
Figure 1.2: Part of the level scheme of helium. In this thesis we will exclusively use the $\{1s2s\}^3S_1 \to \{1s2p\}^3P_2$ transition at the optical wavelength $\lambda = 1083$ nm.

## 2   Atomic beam setup

Observing atomic diffraction with a detector placed in the far-field requires the use of a light atom, such that a relatively large deflection angle can be obtained for a single photon recoil. Furthermore, one should be able to laser cool the atoms in order to prepare a high-quality atomic beam. Also, the atoms have to be detected with high efficiency and sub-recoil precision. Metastable helium in the $\{1s2s\}^3S_1$ state seems to be an excellent choice in this respect [17, 18].

Figure 1.2 shows part of the level scheme of helium. The $\{1s2s\}^3S_1$ state can be populated by exciting ground state atoms $(\{1s^2\}^1S_0)$ by electron impact. The metastable $\{1s2s\}^3S_1$ state (in this thesis often denoted by He*) has a lifetime in excess of two hours, which is caused by strict selection rules preventing the radiative decay back to the $\{1s^2\}^1S_0$ ground state [19]. Laser cooling can be done on the $\{1s2s\}^3S_1 \to \{1s2p\}^3P_2$ transition at the optical wavelength $\lambda = 1083$ nm. It is a closed transition with a 98.8 ns radiative lifetime of the $\{1s2p\}^3P_2$ state. Absorption of a single 1083 nm photon by a metastable helium atom results in a velocity change $v_R = \hbar k/M = 0.092$ ms$^{-1}$ (also known as the recoil velocity), with $k$ the wavenumber of the light and $M$ the mass of the atom.

Knops [17, 18] showed that the photon number experiment and the wavepacket tomography experiment require a He* beam that satisfies rather stringent conditions with respect to the longitudinal velocity distribution $P(v_\parallel)$, the perpendicular

velocity distribution $P(v_\perp)$, and the beam diameter $d_{\text{beam}}$. First of all, the beam has to be slow, $v_\parallel < 400 \text{ ms}^{-1}$, to make sure that the acquired transverse momentum leads to a relatively large deflection angle. It also has to be highly monochromatic, $\sigma v_\parallel / v_\parallel = \sqrt{\langle v_\parallel^2 \rangle}/v_\parallel < 2 \times 10^{-2}$, to ensure both well-defined deflection angles and a well-defined interaction time with the light field. Furthermore, it has to be ultra-collimated in both transverse dimensions, $\sigma v_\perp = \sqrt{\langle v_\perp^2 \rangle} < 0.1 v_R = 9 \times 10^{-3} \text{ ms}^{-1}$, in view of the fact that absorption or emission of a photon changes the atomic velocity by the recoil velocity $v_R$. The 2D-detector has to be placed at least 2 m behind the light field to obtain the required degree of sub-recoil detection precision with a typical detector resolution of 100 $\mu$m. Finally, the atomic beam diameter $d_{\text{beam}}$ should not exceed 25 $\mu$m to ensure that it is narrower than the minimum diameter of the light fields used in the experiments.

# 3  Contents of thesis

The first part of this thesis deals with the construction and characterization of an ultra-high precision atomic beam setup. In the second part of this thesis, the beam setup is used to perform atom optics experiments.

Chapter 2 describes the construction of the atomic beam setup. Several laser cooling mechanisms are used to transform the ensemble of hot He* atoms leaving the source into a slow, monochromatic and ultra-collimated atomic beam. The transverse velocity distribution of the atoms in the beam is collimated to below one tenth of the recoil velocity associated with a 1083 nm photon.

In the experiments described in this thesis, the ultra-high precision atomic beam interacts with a well-defined light field. The momentum transfer between the light field and the atoms causes the latter to be deflected. In chapter 3 we describe the two-dimensional position-sensitive single-atom detector that is used to observe the deflection with high precision. Here, we also use the 2D-detector to fully characterize both the motional and the electronic state of the atoms in the beam.

An atom experiencing spontaneous emission will emit a photon in a random direction. The angular distributions of dipole radiation are expected to be anisotropic. Furthermore, they depend on the polarization of the emitted photon. Two distinct distributions, associated with decay via either a $\pi$- or a $\sigma$-transition, can be identified. In chapter 4 we let the atoms in the beam interact with a weak running wave, which causes some of the atoms to spontaneously emit a photon. The recoil associated with the emitted photon causes the atoms to be deflected. The corresponding deflection patterns are measured on the 2D-detector and immediately reflect the angular distributions of spontaneous emission. A state-selective deflection technique, based on the Stern-Gerlach effect, is used to distinguish between $\pi$- and $\sigma$-transitions.

In chapter 5 we let the atomic beam interact with an off-resonant standing light wave. The cold atoms in the beam, which behave like plane atomic waves, are diffracted by the periodic dipole potential. By tuning the experimental parameters into the so-called Bragg regime, the motional state of each atom is prepared into a

coherent superposition of only two momentum states. Thus, the standing light wave acts as a coherent beam splitter for atoms: each "splitted" atomic wavepacket moves along two spatially separated paths at the same time. The splitting ratio of the beam splitter can be tuned with the intensity of the standing light wave. In this chapter we produce a tunable coherent beam splitter for atoms with two well-defined output ports and a maximum splitting angle of 5.9 mrad. This leads to a macroscopic path separation of up to 12 mm on the 2D-detector. Atoms that undergo spontaneous emission during the Bragg scattering process can easily be identified on the 2D-detector due to the acquired random photon recoil. This allows for a selective removal of these atoms from the measurement.

# 4 Future experiments

## 4.1 Photon number measurement in a high-finesse optical cavity

In the first planned experiment, diffraction of atoms from a light field stored in a single mode of a high-finesse optical cavity will be used to provide a direct demonstration of the quantization of the electromagnetic field. Instead of storing information on the photon statistics of the cavity field in the electronic state of the atom, as reported by Brune *et al.* [20], this information can also be stored in the motional state of the atom [21–24]. We plan to use our high-finesse optical cavity with a measured reflective finesse of $6.5 \times 10^5$ for the fundamental $TEM_{00}$ mode [17]. The average photon number in the cavity is chosen to be well below unity. In this regime the classical approximation, in which the light field has a well-defined amplitude, breaks down and quantum effects become observable. The corresponding atomic diffraction pattern observed on the 2D-detector should then provide a clear signature of field quantization. Even the average photon number can be extracted from the diffraction pattern under the right experimental conditions. To make the required "snapshot" of the field, the atom has to traverse the light field in less than the cavity damping time. This regime can not be addressed with atoms from a MOT or a fountain [16], due to their relatively low velocity. The optimal longitudinal velocity of the He* beam for this experiment is around $250 \text{ ms}^{-1}$ [17].

Furthermore, a "single-atom laser" [25] can be build by exciting the atoms with a classical light wave perpendicular to and overlapping with the cavity mode. The excited atoms can transfer photons from the perpendicular light wave into the cavity mode. Here, a single atom acts as a gain medium to produce a cavity field containing several photons on average. The population of the cavity mode can be monitored by measuring the light leaking out of the cavity. The single-atom laser is a true "inversionless" laser since the incoherent excitation by the perpendicular light wave does not lead to population inversion. The lasing is caused by a fundamental asymmetry between the rate of absorption and stimulated emission, the latter being significantly higher in the regime of low intra-cavity photon numbers.

## 4.2   Quantum tomography of atomic motion

Another possible experiment, using a classical light field, constitutes the measurement of the full density matrix associated with the center-of-mass motion of an ensemble of one-dimensional atomic wavepackets. The density matrix can be reconstructed by measuring a set of tomographic projections of the associated Wigner function [26, 27]. The wavepackets are produced by sending the cold atomic beam through a mechanical transmission grating. These wavepackets are then sent through the nodes of an off-resonant standing light wave. The dipole potential, which is approximately harmonic near the nodes, rotates the Wigner function over an angle that can be controlled with the intensity of the standing light wave. A set of tomographic projections of the Wigner function over an angle-interval of $\pi$ radians is sufficient to reconstruct the Wigner function and thus the corresponding density matrix. With free evolution of atomic wavepackets, instead of interaction with a light field, rotation angles up to $\pi/2$ have been achieved [28]. With the same method full reconstruction has been achieved of the wavefunction associated with an electromagnetic field state [29] and the center-of-mass motion of a single trapped ion [30].

# References

[1] C. Cohen-Tannoudji, J. Dupont-Roc, and G. Grynberg, *Atom-photon interactions: basic processes and applications* (John Wiley & Sons, New York, 1992).

[2] H.J. Metcalf and P. van der Straten, *Laser cooling and trapping* (Springer, New York, 1999).

[3] W.D. Phillips, J.V. Prodan, and H.J. Metcalf, J. Opt. Soc. Am. B **2**, 1751 (1985).

[4] E. Raab, M. Prentiss, A. Cable, S. Chu, and D.E. Pritchard, Phys. Rev. Lett. **59**, 2631 (1987).

[5] M. Kasevich, E. Riis, S. Chu, and R.G. DeVoe, Phys. Rev. Lett. **63**, 612 (1989).

[6] M.H. Anderson, J.R. Ensher, M.R. Matthews, C.E. Wieman, and E.A. Cornell, Science **269**, 198 (1995).

[7] K.B. Davis, M.-O. Mewes, M.R. Andrews, N.J. van Druten, D.S. Durfee, D.M. Kurn, and W. Ketterle, Phys. Rev. Lett. **75**, 3969 (1995).

[8] C.C. Bradley, C.A. Sacket, J.J. Tollett, and R.G. Hulet, Phys. Rev. Lett. **75**, 1687 (1995); C.C. Bradley, C.A. Sacket, and R.G. Hulet, Phys. Rev. Lett. **78**, 985 (1997).

[9] D.G. Fried, T.C. Killian, L. Willmann, D. Landhuis, S.C. Moss, D. Kleppner, and T.J. Greytak, Phys. Rev. Lett. **81**, 3811 (1998).

[10] See the special issue on atom optics and interferometry in Appl. Phys. B **54** (1992).

[11] Yu. B. Ovchinnikov, J.H. Müller, M.R. Doery, E.J.D. Vredenbregt, K. Helmerson, S.L. Rolston, and W.D. Phillips, Phys. Rev. Lett. **83**, 284 (1999).

[12] M. Kozuma, L. Deng, E.W. Hagley, J. Wen, R. Lutwak, K. Helmerson, S.L. Rolston, and W.D. Phillips, Phys. Rev. Lett. **82**, 871 (1999).

[13] L. Deng, E.W. Hagley, J. Wen, M. Trippenbach, Y. Band, P.S. Julienne, J.E. Simsarian, K. Helmerson, S.L. Rolston, and W.D. Phillips, Nature **398**, 218 (1999).

[14] E.W. Hagley, L. Deng, M. Kozuma, J. Wen, K. Helmerson, S.L. Rolston, and W.D. Phillips, Science **283**, 1706 (1999).

[15] S. Inouye, T. Pfau, S. Gupta, A.P. Chikkatur, A. Görlitz, D.E. Pritchard, and W. Ketterle, Nature **402**, 641 (1999).

[16] P. Münstermann, T. Fischer, P.W.H. Pinkse, and G. Rempe, Opt. Comm. **159**, 63 (1999); P. Münstermann, T. Fischer, P. Maunz, P.W.H. Pinkse, and G. Rempe, Phys. Rev. Lett. **82**, 3791 (1999); P. Münstermann, T. Fischer, P. Maunz, P.W.H. Pinkse, and G. Rempe, Phys. Rev. Lett. **84**, 4068 (2000).

[17] R.M.S. Knops, *Quantum optics with a cold helium beam*, Ph.D. thesis, Eindhoven University of Technology (1998).

[18] R.M.S. Knops, A.E.A. Koolen, H.C.W. Beijerinck, and K.A.H. van Leeuwen, Laser Physics **9**, 286 (1999).

[19] J.R. Woodworth and H. Warren Moos, Phys. Rev. A **12**, 2455 (1975).

[20] M. Brune, F. Schmidt-Kaler, A. Maali, J. Dreyer, E. Hagley, J.M. Raimond, and S. Haroche, Phys. Rev. Lett. **76**, 1800 (1996).

[21] P. Meystre, E. Schumacher, and S. Stenholm, Opt. Comm. **73**, 443 (1989).

[22] M.J. Holland, D.F. Walls, and P. Zoller, Phys. Rev. Lett. **67**, 1716 (1991).

[23] V.M. Akulin, Fam Le Kien, and W.P. Schleich, Phys. Rev. A **44**, R1462 (1991).

[24] A.M. Herkommer, V.M. Akulin, and W.P. Schleich, Phys. Rev. Lett. **69**, 3298 (1992).

[25] K. An, J.J. Childs, R.R. Dasari, and M.S. Feld, Phys. Rev. Lett. **73**, 3375 (1994).

[26] S.H. Kienle, D. Fischer, W.P. Schleich, V.P. Yakovlev, and M. Freyberger, Appl. Phys. B **65**, 735 (1997).

[27] M. Freyberger and S.H. Kienle, Phys. Rev. A **56**, 195 (1997).

[28] Ch. Kurtsiefer, T. Pfau, and J. Mlynek, Nature **386**, 150 (1997).

[29] D.T. Smithey, M. Beck, M.G. Raymer, and A. Faridani, Phys. Rev. Lett. **70**, 1244 (1993).

[30] D. Leibfried, D.M. Meekhof, C. Monroe, B.E. King, W.M. Itano, and D.J. Wineland, J. Mod. Opt. **44**, 2485 (1997).

# Chapter 2

# A collimated, slow and monochromatic beam of metastable helium atoms

## 1 Introduction

The experiments described in this thesis can only be done if we use a He* beam that satisfies a number of stringent criteria: the atomic beam has to be slow, $v_\parallel < 400$ ms$^{-1}$, and highly monochromatic, $\sigma v_\parallel / v_\parallel < 2 \times 10^{-2}$, while at the same time it has to be ultra-collimated in both transverse dimensions, $\sigma v_\perp < 0.1 \hbar k / M = 9 \times 10^{-3}$ ms$^{-1}$, and narrow, $d_{\text{beam}} = 25$ $\mu$m. In other words, the beam has to be both extremely cold and narrow. As we will see from this chapter, these requirements are not easy to meet if one also requires a beam flux well above 1 s$^{-1}$.

Standard design atomic sources for metastable noble gases produce rather hot atomic beams that do not satisfy the criteria mentioned above. Fortunately, with the advent of laser cooling, it has become possible to manipulate the motion of neutral atoms in many ways. In particular, the techniques developed in the last two decades have enabled the production of ever colder atomic samples. Temperatures of 3 nK have been achieved in one dimension [1]. In combination with the more conventional evaporative cooling technique [2], it has led to the observation of Bose-Einstein condensation (BEC) in weakly interacting atomic gases, where both low temperatures and high atomic densities are required [3].

The idea to cool neutral atoms to very low temperatures using almost resonant laser light was first proposed by Wineland and Dehmelt [4] and Hänsch and Schawlow [5] in 1975. The first experimental results by Chu *et al.* [6] date back to 1985. Since then, the field has expanded rapidly with applications in many areas of atomic physics, such as ultra-high resolution spectroscopy [7] and atom optics [8].

The techniques of laser manipulation can not only be used to cool atoms in either one, two or three dimensions but it can also serve as a tool for producing optical elements for neutral atoms [9]. Unlike in traditional optics, the dissipative nature of laser cooling allows an increase in phase-space density of an atomic sample. In this chapter we will use several optical elements to manipulate the motion of metastable helium atoms, such that an atomic beam is created that satisfies all the criteria mentioned above.

# 2   Spontaneous radiation force

Consider a two-level atom interacting with a single resonant running laser wave. By absorbing a photon from the laser, the atom obtains the photon's momentum which is directed along the laser beam. By emitting the photon, the atom obtains an additional recoil, equal in size but opposite to the momentum of the re-emitted photon. Over many absorption/spontaneous emission cycles, the emission recoils average out to zero, while the absorption momenta add up to an average force $\vec{F} = \hbar \vec{k} \Gamma n_e$. This force is called the spontaneous radiation force, or radiation force in short. It is proportional to the photon momentum $\hbar \vec{k}$, with $k = |\vec{k}| = 2\pi/\lambda$ the wavenumber of the photon, and to the spontaneous emission rate $\Gamma n_e$, with $\Gamma$ the decay rate of the excited state and $n_e$ the excited state population. Absorption of a photon from the laser beam followed by stimulated emission into the same laser beam does not transfer any net momentum to the atom, hence does not produce a force. For resonant excitation the excited state population is given by $n_e = s/(2(s + 1))$, with the on-resonance saturation parameter $s$ given by $s = I/I_0$, in which $I$ is the laser intensity. The saturation intensity $I_0$ depends on the atomic transition involved. The radiation force saturates for $I \to \infty$, giving a maximum force of $\vec{F}_{\mathrm{max}} = \hbar \vec{k} \Gamma/2$. For metastable helium atoms, excited on the $\{2s\}^3S_1 \to \{2p\}^3P_2$ transition at $\lambda = 1083$ nm, the radiation force yields a maximum acceleration of $4.7 \times 10^5$ ms$^{-2}$. For off-resonant excitation one has to take into account the Lorentzian-shaped profile of the transition. For a single running wave the radiation force then takes the form

$$\vec{F} = \frac{\hbar \vec{k} \Gamma s}{2(1 + s + \{2\Delta_{\mathrm{eff}}/\Gamma\}^2)},$$

(2.1)

in which $\Delta_{\mathrm{eff}}$ is the effective detuning from resonance.

## 2.1   Velocity-dependent radiation force

In a coordinate frame moving along with the atom, the effective detuning $\Delta_{\mathrm{eff}}$ is not only determined by the laser detuning $\Delta_{\mathrm{L}} = \omega_{\mathrm{L}} - \omega_0$, with $\omega_{\mathrm{L}}$ the laser frequency and $\omega_0$ the frequency of the atomic transition, but also contains a contribution $\Delta_{\mathrm{D}} = -\vec{k} \cdot \vec{v}$ due to the Doppler effect. Thus, the radiation force depends on the atomic velocity component along the direction of the laser. The velocity-dependence of the radiation force forms the basis for the standard laser cooling mechanism known as "Doppler cooling" or "optical molasses" [9].

Consider an atom interacting with a standing laser wave, produced by two counterpropagating running laser waves of the same frequency and intensity. The laser light is slightly red-detuned with respect to the atomic transition, thus $\Delta_{\mathrm{L}} < 0$. An atom moving slowly along one of the laser beams will see the other counterpropagating laser beam slightly blue-shifted by the Doppler effect, and consequently closer to resonance. It will absorb more photons per unit of time from the counterpropagating laser than from the copropagating laser. Hence, it will experience a net force $F$ opposite to its own velocity $v$, i.e., a decelerating force. Around $v = 0$ the decelerating force is proportional to the velocity and can be regarded as a pure friction force,
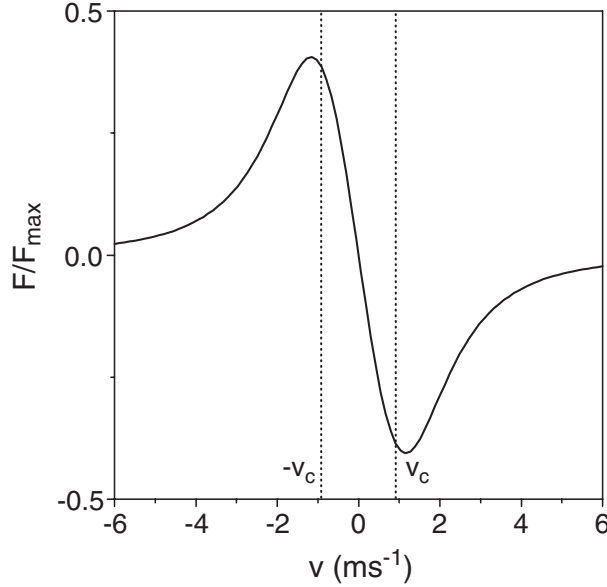
Figure 2.1: Velocity-dependence of the decelerating force in Doppler cooling on the helium $\{2s\}^3S_1 \rightarrow \{2p\}^3P_2$ transition. Here: $\Delta_L = -\Gamma/2$ and $s = 2$. The decelerating force acts as a pure friction force between $-v_c$ and $v_c$.

which dampens the atomic motion. For $s \ll 1$ the friction force can be approximated by [10]

$$F = \frac{8\hbar k^2 s(\Delta_L/\Gamma)v}{\left(1 + \{2\Delta_L/\Gamma\}^2\right)^2} \equiv -\beta v, \tag{2.2}$$

in which $\beta$ ($\geq 0$) is the damping coefficient. Figure 2.1 shows the decelerating force for optimal cooling ($\Delta_L = -\Gamma/2$ and $s = 2$) as a function of the atomic velocity for the transition in helium as mentioned above. Atoms with a velocity below the so-called capture velocity $v_c = -\Delta_L/k$ experience the pure friction force. Using three orthogonal pairs of laser beams, the atoms are cooled in three dimensions [6]. Note that such a three-dimensional optical molasses merely cools the atoms but lacks the ability to trap them, since there is no position-dependent force that drives the atoms back to a single equilibrium position in space. In this chapter we will collimate an atomic beam, i.e., cool it in two dimensions by two orthogonal pairs of laser beams [11].

## 2.2   Position-dependent radiation force

In a magnetic field, each atomic level is shifted by an amount $\Delta E = -\vec{\mu} \cdot \vec{B} = \mu_B B g_i m_i$, with $\vec{\mu}$ the magnetic moment of the atom, $\mu_B$ the Bohr magneton, $B$ the magnetic field, $g_i$ the Landé factor of level $|i\rangle$ and $m_i$ the magnetic quantum number with respect to the quantization axis defined by the field. Thus, the effective detuning $\Delta_{\text{eff}}$ will also contain a contribution $\Delta_B = \mu_B B(g_e m_e - g_g m_g)/\hbar$. In the case of an inhomogeneous magnetic field $\vec{B}(\vec{r})$, the radiation force of Eq. 2.1 will become position-dependent. Combining both velocity- and position-dependent forces allows

for efficient cooling *and* trapping of atoms in a so-called "Magneto-Optical Trap" (MOT) [12]. In this chapter we will use two-dimensional versions of the MOT to efficiently focus [11] and compress [13] an atomic beam. The position-dependent force can also be used to decelerate atoms from thermal velocities down to even zero velocity [14]. We will use this so-called "Zeeman shift compensated slowing" technique to produce a highly monochromatic atomic beam.

## 2.3   Cooling limits

The minimum temperature of an atomic sample achieved by pure Doppler cooling is called the Doppler limit [6]. Its existence can be understood by the fact that the Doppler cooling process inevitably incorporates a small heating mechanism. The Doppler limit is reached when both the cooling and the heating mechanism are in equilibrium. The heating process is caused by the fluctuations of the atomic momentum due to the random direction of spontaneous emission and due to the randomness in the number of absorbed photons. The momentum transfer during cooling resembles a random walk through momentum space with finite steps of $\hbar\vec{k}$. Even though the average momentum of an atomic sample can be become arbitrarily small, the momentum spread and thus the temperature is limited to a finite value, the so-called Doppler temperature $T_D$.

The temperature of an atomic sample is usually defined for each motional degree of freedom separately by $k_B T_i/2 = M\langle v_i^2\rangle/2$, with $i \in \{x, y, z\}$ and $M$ the mass of the atom. The Doppler temperature depends on the number of dimensions occupied by cooling laser beams. For a one-dimensional ($N = 1$) model of optical molasses it is derived that $T_D = \hbar\Gamma/(2k_B)$ [10]. For metastable helium atoms cooled on the $\{2s\}^3S_1 \rightarrow \{2p\}^3P_2$ transition this amounts to $T_D = 39\ \mu$K, with the corresponding Doppler velocity $v_D = \sqrt{\langle v^2\rangle} = 0.28$ ms$^{-1}$. In a higher dimensional ($N \in \{2, 3\}$) model of optical molasses, the Doppler limit per dimension is essentially the same provided $2Ns \ll 1$: the minimum temperature hardly increases as long as the atoms are not yet saturated by adding another pair of laser beams [10]. A low value of $s$, however, results in a low cooling rate. Thus, in systems where the molasses can only be applied during a short time, such as in an atomic beam setup, one often has to use higher values of $s$ to reach low temperatures.

A photon can be spontaneously emitted in each direction, resulting in a recoil that is not only restricted to the dimensions occupied by the cooling laser beams. This means that part of the momentum spread, that causes the heating, can be transferred to the non-cooled dimensions. For this reason, the real Doppler temperatures are slightly lower for one- and two-dimensional cooling than derived above. Strictly speaking, the Doppler temperature depends on the shape of the angular spontaneous emission radiation distributions. In chapter 4 we will see that these radiation distributions do not have to be isotropic and depend on the polarization of the emitted photons. This can cause anisotropic Doppler temperatures.

By exploiting the internal degrees of freedom of the atom in the light field combined with a polarization gradient or a magnetic field, it is possible to cool below the Doppler limit [15–18]. Again, a lower limit is encountered, which is caused by the
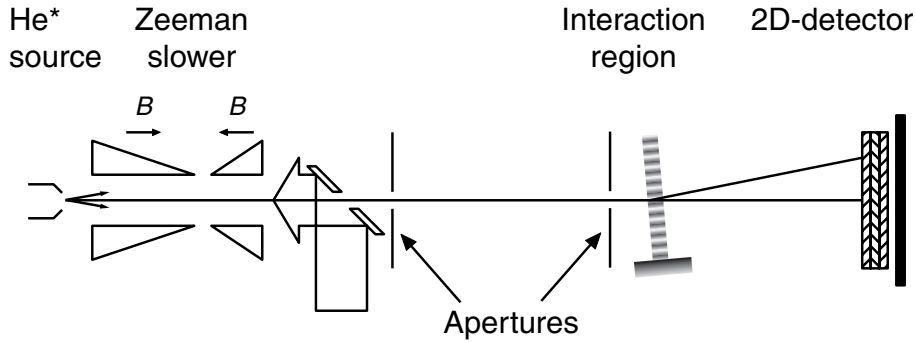
Figure 2.2: The minimum configuration, with one laser cooling section, that can produce the required ultra-collimated, slow and monochromatic beam of metastable helium atoms.

finite recoil energy $\varepsilon_R = \hbar^2 k^2/(2M)$ associated with the absorption or emission of a single photon. The so-called recoil temperature is found to be $T_R = 2\varepsilon_R/k_B$. In the case of metastable helium cooled on the $\{2s\}^3S_1 \rightarrow \{2p\}^3P_2$ transition this amounts to $T_R = 4\,\mu$K, with the associated recoil velocity $v_R = 0.092\,\mathrm{ms}^{-1}$.

Cooling below the recoil limit requires that the spontaneous emission process is turned off for atoms that are already cold enough. This can either be solved by using a dark state of which the population is made velocity-selective (VSCPT) [19], or by a scheme based on Raman transitions within the Zeeman multiplet [20]. In this chapter we will only deal with Doppler cooling, although the use of a two-dimensional MOT allows, in theory, for reaching sub-Doppler temperatures.

# 3   Overview of the atomic beam setup

In this section we will introduce the necessary elements of the setup, required to produce a He* beam that satisfies all the criteria put forward in chapter 1. It will become evident that a number of laser cooling sections are needed to obtain the required "bright" atomic beam. The performance of each laser cooling section can be expressed in the phase-space brightness $B$, which is equal to the number of atoms per second per unit of phase-space area ($\mathrm{mm}^2\,\mathrm{mrad}^2$). In particular, the center-line phase-space brightness $B_0$ is important, i.e., the brightness near the axis in the propagation direction of the atoms. Knops [21, 22] simulated the performance of each of these laser cooling sections using a numerical Monte-Carlo approach. Based on these results he made a design for a setup that should satisfy all the criteria. In the rest of this section we will follow his approach while adding some modifications, where a different implementation was chosen.

## 3.1   Minimum configuration

The minimum configuration that produces the required cold atomic beam is shown in Fig. 2.2 and consists of a source, a Zeeman slower, and a pair of collimating aper-
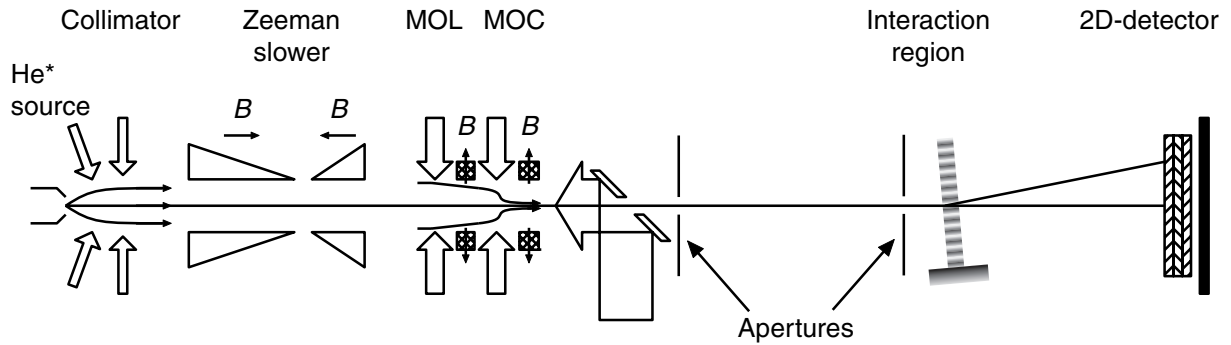
Figure 2.3: The final configuration, with four laser cooling sections, that is capable of producing an atomic beam flux well above 1 s$^{-1}$.

tures. The experiments, described in chapter 1, also require an interaction region and a two-dimensional position-sensitive detector.

Knops [21,22] found that an ordinary liquid-nitrogen cooled supersonic discharge source produces a He* beam with a velocity distribution centered around 1300 ms$^{-1}$ with $\sigma v_{\parallel} = 210$ ms$^{-1}$, a center-line brightness $B_0 = 1.0 \times 10^9$ s$^{-1}$ mm$^{-2}$ mrad$^{-2}$ and a center-line intensity of $2 \times 10^{14}$ s$^{-1}$ sr$^{-1}$. In order to produce a slow (here we take $v_{\parallel} = 250$ ms$^{-1}$) and sufficiently monochromatic ($\sigma v_{\parallel}/v_{\parallel} < 2 \times 10^{-2}$) beam of He*, one needs to add a Zeeman slower. A disadvantage of the slowing process is that the beam divergence increases considerably, due to both diffusion in the transverse velocity direction and reduction of the longitudinal velocity component. Thus, the beam brightness is dramatically reduced by the Zeeman slower. Simulations show that behind the Zeeman slower $B_0 = 6.8 \times 10^2$ s$^{-1}$ mm$^{-2}$ mrad$^{-2}$. Finally, the atomic beam has to be collimated and narrowed such that $\sigma v_{\perp} < 0.1 v_R = 9 \times 10^{-3}$ ms$^{-1}$ and $d_{\text{beam}} = 25$ $\mu$m. This is done by using two apertures of 60 $\mu$m and 25 $\mu$m in diameter, respectively, separated by 2 m. Such a mechanical collimator, however, has a phase-space acceptance area $A$ of merely $4.4 \times 10^{-7}$ mm$^2$ mrad$^2$. The final atomic beam flux $\dot{N}$ can now be estimated, resulting in $\dot{N} = B_0 A = 3.0 \times 10^{-4}$ s$^{-1}$ or one atom per hour! Evidently, this minimum configuration has to be extended with additional laser cooling sections to increase $B_0$ significantly.

## 3.2 Final configuration

Figure 2.3 shows the setup that is going to be used in this thesis. It contains three extra transverse laser cooling stages in order to bring the beam flux above 1 s$^{-1}$.

**Magneto-optical lens and compressor**

First, two transverse laser cooling stages are added in order to compress the broad atomic beam behind the Zeeman slower into a narrow one. For helium this is most efficiently done by using a combination of a magneto-optical lens (MOL) [11] and a magneto-optical compressor (MOC) [13]. The MOL and the MOC exploit both the velocity- and the position-dependence of the radiation force. The MOC can com-

press atoms within a small capture area into a narrow beam. The MOL effectively increases this capture area by prefocusing the broad atomic beam into the MOC. For this purpose, the MOC is placed near the focus of the MOL (the focal length is typically 0.6 m). The simulated signal gain is considerable: a factor of $6.3 \times 10^4$ can be achieved. The beam behind the MOC has a diameter of 0.2 mm and a brightness $B_0 = 4.3 \times 10^7 \, \text{s}^{-1} \, \text{mm}^2 \, \text{mrad}^2$, resulting in: $\dot{N} = 19 \, \text{s}^{-1}$.

### Collimator

Furthermore, the brightness can be enhanced by adding a transverse cooling section directly behind the source. It guides the atoms that leave the source within a certain angle with respect to the beam axis, the so-called capture angle, into a parallel beam. For this purpose, a two-dimensional optical molasses with a curved wavefront is used. With a saturation parameter $s = 7.5$, the maximum capture angle is around 25 mrad. The phase-space brightness behind the Zeeman slower can then be increased by a factor of 28. This brings the simulated beam flux up to $5.3 \times 10^2 \, \text{s}^{-1}$, which would be sufficient for the experiments performed in this thesis. Thus, the configuration of Fig. 2.3 gives a factor of $1.8 \times 10^6$ higher beam flux than the minimum configuration of Fig. 2.2!

### Doppler cooler

In the quantum tomography experiment, described in chapter 1, the effective beam flux is 10 times lower due to the 10% open fraction of the free standing transmission gratings. For this experiment the beam flux can be increased by an additional factor of 80 by adding a short Doppler cooling section behind the MOC. Behind the MOC, the divergence of the beam is of the order of 10 mrad rms. This translates into a velocity spread of 2.5 ms$^{-1}$ rms, which is far above the Doppler limit of 0.28 ms$^{-1}$. In the Doppler cooling section, this spread is reduced to the Doppler limit. We will not implement this extra cooling section in this thesis.

## 4   Mechanical design

The cavity QED experiments that use an ultra-high finesse optical cavity, as described in chapter 1, put extreme requirements on the level of mechanical vibrations allowed in the setup. As many sources of vibrations as possible have to be eliminated in order to keep the mirror separation stable to within $10^{-12}$ m.

First of all, we use turbomolecular vacuum pumps with a magnetically suspended rotor, that produce roughly a factor of ten less vibrations than turbomolecular pumps with conventional bearings. The flow of liquid nitrogen through the atomic beam source and cooling water through the Zeeman magnets also introduces vibrations. The critical parts of the setup have to be isolated from these vibrations. Therefore, the setup consists of two mechanically isolated parts mounted on separate frames, connected only by bellows. An artist's impression of the experimental

Collimator

Source

Zeeman slower

MOL  MOC

Interaction
chamber

2D-detector
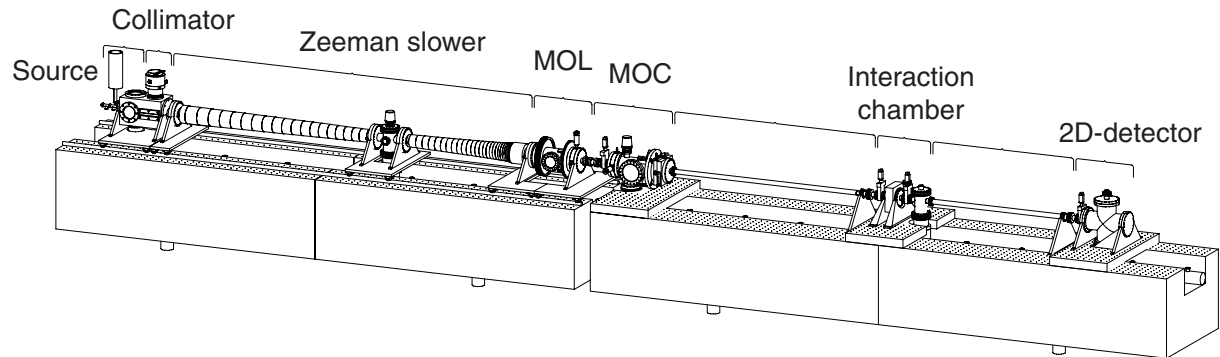
Figure 2.4: Artist's impression of the experimental setup. The total length of the setup amounts to 9.5 m.

Collimator

Source

Zeeman
slower

MOL  MOC

Interaction
chamber

2D-detector

Scroll pump

Turbomolecular pump

Pressure gauge

Valve

Bellows

Scroll pump
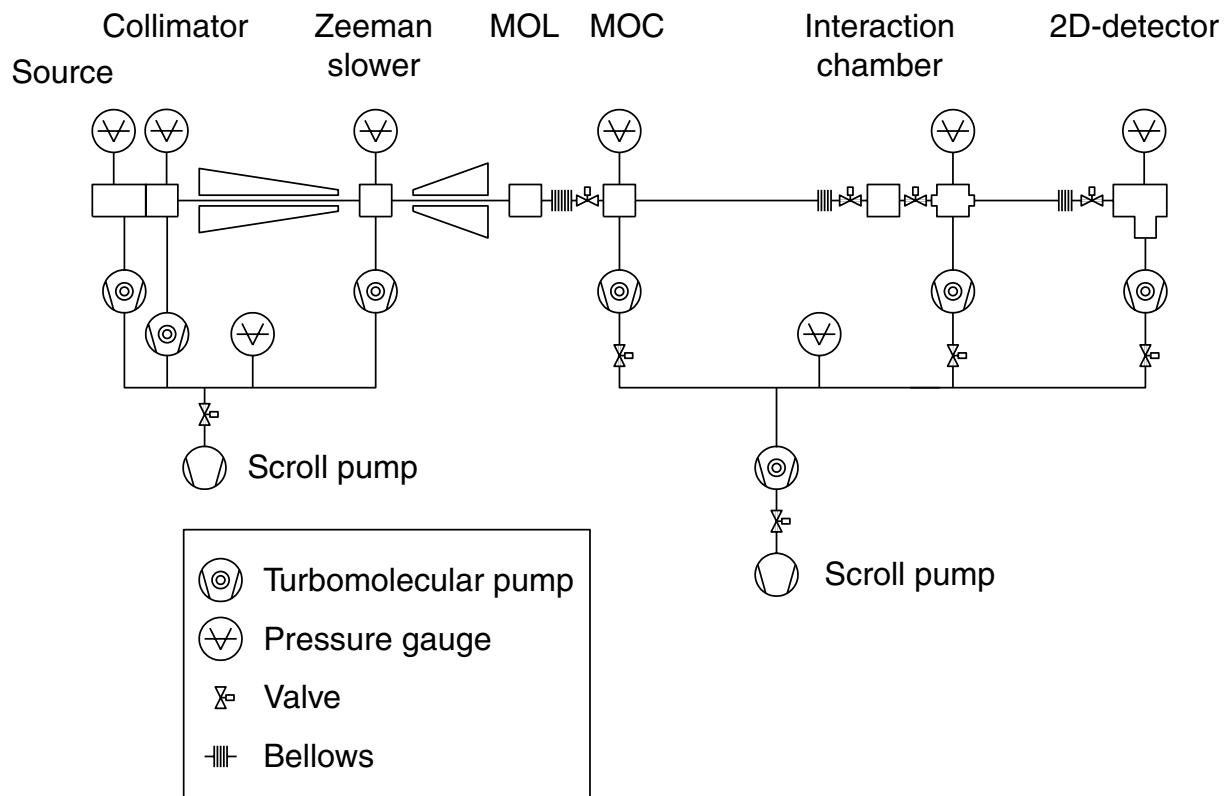
Figure 2.5: Schematic view of the vacuum setup.

setup is shown in Fig. 2.4. On the first frame the source, the collimator, the Zeeman slower, and the magneto-optical lens are located. On the second frame the magneto-optical compressor, the interaction chamber, and the detector are situated. The second frame rests on airmounts for isolation from floor vibrations.

The supporting frames are made from PVC construction foam (brand name Klegecell), enclosed by aluminum plates. The foam/aluminum sandwich combines high rigidity, which is necessary to retain the beam center-line stability, with low weight and good vibration damping properties.

Thermal fluctuations in the environment (air drafts, local heat sources) can cause the frames to distort. Under typical conditions, we have measured the bending angle of one of the frames with respect to a laser beam mounted on one side during 24 hours. The drift of this angle stays within 10 $\mu$rad. For atoms traveling from the interaction chamber to the detector this translates to a displacement of 20 $\mu m$, which is well within the detector resolution. The aluminum top plates of the frame serve double duty as optical table tops: they are equipped with a mounting hole grid for optics mounts.

After the brightening process, the beam is collimated by two apertures. The position of these apertures has to be adjustable, while their suspension has to be very rigid to minimize sensitivity for vibrations. We have developed such a suspension, using flexure hinges, which allow for a displacement of 2 mm.

# 5    Vacuum system

Contamination of the vacuum by hydrocarbons could deposit on the mirror surfaces and quickly decrease the finesse of the cavity in cavity QED experiments. The use of turbomolecular pumps with magnetic bearings allows us to construct a completely oil-free vacuum system, which is shown in Fig. 2.5. Each of the two "halves" of the setup is pumped by three Edwards EXT250M turbo pumps, backed by "dry" scroll pumps (Edwards ESDP12). To get rid of the residual gas load of the source, the collimator chamber serves as a differential pumping stage. It is connected to the source chamber by the skimmer hole (1 mm diameter) and to the Zeeman slower via a tubular pump resistance (8 mm inner diameter and 100 mm length). In the second part of the setup, an extra turbo pump is inserted between the turbo pumps and the scroll pump in order to increase the compression ratio. This is necessary to obtain a pressure on the level of $10^{-9}$ mbar in the interaction region and at the 2D-detector.

The vacuum system is controlled and safeguarded by a PLC system, interfaced with a PC for operation of the setup and programming of the PLC. The PLC system provides automatic startup and shutdown procedures and protects the vacuum system against catastrophic operator errors.

DL CL    L1       OI        L2  λ/2   BS

M        Gas discharge cell   λ/4    PBSC    PD
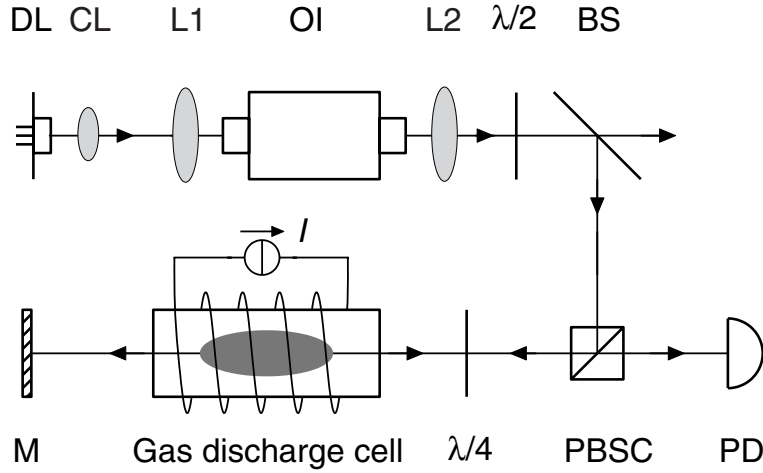
Figure 2.6: Diode laser setup that is frequency-stabilized by saturated absorption spectroscopy. DL: diode laser, CL: collimating lens, OI: optical isolator, L1+L2: telescope to focus the laser light through the optical isolator, $\lambda/2$: half wave plate, BS: beam splitter, PBSC: polarizing beam splitter cube, $\lambda/4$: quarter wave plate, M: mirror, PD: photo-detector.

# 6   Laser setup

All the lasers used for laser cooling are locked to the ${2s}^3S_1 \rightarrow {2p}^3P_2$ transition in helium ($\lambda = 1083.034$ nm, $I_0 = 1.67$ W/m$^2$ for the $|1,+1\rangle \rightarrow |2,+2\rangle$ two-level transition and $\Gamma = 1.022 \times 10^7$ s$^{-1}$). We use DBR diode lasers (Spectra Diode Labs, SDL-6702H1 [23]) with a free-running linewidth of 3 MHz [24] and a maximum output power of 50 mW at a typical injection current of 180 mA. Three diode lasers are used for collimation, slowing and compression of the atomic beam. The output light from each diode is linearly polarized in the vertical $y$-dimension and collimated into an elliptically shaped beam ($2w_x = 4.8$ mm and $2w_y = 1.4$ mm) by an AR-coated aspheric lens (Thorlabs C230TM-C, $f = 4.5$ mm, 0.55 NA). The injection current for the diodes is supplied by home-made diode laser drivers. Each driver is equipped with a controller capable of keeping the temperature of the diode stable to within 1 mK by using the NTC resistor and the Peltier element inside the laser. The drivers can be controlled by computer, allowing digital fine tuning of the injection current in steps of 0.5 $\mu$A. The drivers are also equipped with an analog voltage input for fine tuning of the injection current with 83 $\mu$A/V. The diodes have a typical laser frequency vs. current tunability of 1 MHz/$\mu$A.

## 6.1   Saturated absorption spectroscopy

The lasers for the collimator and the MOL/MOC-combination require only a small detuning from resonance and are frequency locked using saturated absorption spectroscopy [25]. A schematic representation of such a frequency-stabilized diode laser setup is shown in Fig. 2.6. Around 300 $\mu$W of the main laser beam is split off by a beam splitter (BS). After passing a polarizing beam splitter cube (PBSC, Newport) the

light is circularly polarized by a quarter wave plate (Eksma, low order quartz). The $\sigma^+$-light passes an RF (30 MHz) excited discharge in a gas cell, filled with 0.3 mbar helium [26]. It is retro-reflected by a mirror and traces its way back through the gas cell. After passing the quarter wave plate and the PBSC, it is focused onto an InGaAs photo-detector (Hamamatsu G6854-01) equipped with additional pre-amplifier. The $\sigma^+$-$\sigma^+$ configuration pumps the atoms into the $|m_g = +1\rangle$ state, allowing excitation of only the two-level transition. Due to the Doppler shift, both counterpropagating beams saturate atoms with opposite velocity components along the common axis of the laser beams for a given laser frequency. Around resonance both beams start to address the same atoms (with zero velocity) causing a lower total absorption. The Doppler-free part of the absorption profile shows a narrow peak with a FWHM width of 10 MHz, while the Doppler-broadened part has a FWHM width of 2.0 GHz, corresponding to the 400 K temperature in the gas discharge. The transition frequency of the atoms in the gas cell can be changed by applying a magnetic field parallel to the laser. The resulting Zeeman shift changes the level separation between the ground and the excited state.

The Doppler-free absorption signal is turned into a dispersive error signal by applying a small oscillating (1025 Hz) magnetic field over the discharge cell. The modulation in the atomic transition frequency causes a modulated photo-detector signal. Using a lock-in amplifier, the photo-detector signal is transformed into the frequency derivative of the absorption profile. The laser is locked to the zero crossing of the error signal. By applying an additional DC magnetic field over the gas cell, the zero crossing can be frequency shifted, which enables us to detune the laser from resonance by a maximum amount of $\pm 200$ MHz. When in lock, the laser has a frequency stability of around 500 kHz.

## 6.2   Collimator and Zeeman slower

The diode lasers for the collimator and the Zeeman slower are protected from unwanted optical feedback by an optical isolator (collimator laser: ConOptics model 715, 40 dB isolation, 90% transmission; Zeeman laser: OFR IO-D-1083, 47 dB isolation, 75% transmission). We use two lenses to focus the laser light through the isolator, as shown in Fig. 2.6. Additional half wave plates (Eksma, low order quartz) are used to rotate the linear polarization of the light back to vertical.

The collimator laser is frequency locked close to resonance by saturated absorption spectroscopy. The frequency of the Zeeman slower laser is stabilized in a different way, since it requires a detuning larger than 200 MHz (in our case: $\Delta_L/(2\pi) = -740$ MHz). For this purpose, around 150 $\mu$W of both the collimator and the Zeeman laser are optically heterodyned onto a fast InGaAs photo-detector (Hamamatsu G6854-01, 2 GHz bandwidth by 5 V negative bias). The beat signal is further amplified (Phillips Scientific model 6954, 1.5 GHz bandwidth and maximum voltage gain of 100) and fed into a frequency counter (Voltcraft 7023, 1.5 GHz range). The beat frequency is kept at a constant value by a digital feedback loop. In this loop a computer reads the beat frequency via an RS232 port and corrects the frequency of the Zeeman laser by means of the injection current. The counter is set to a gate
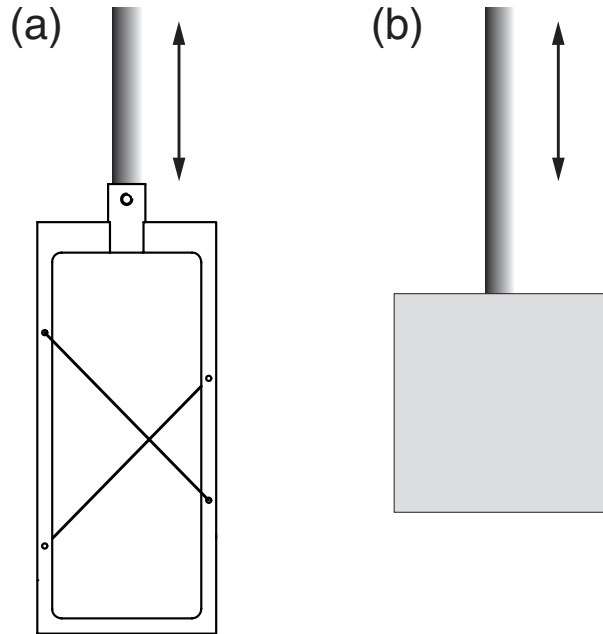
Figure 2.7: Artist's impression of a wire scanner (a) and a knife-edge scanner (b).

time of 100 ms giving a 1 kHz resolution. This allows us to eliminate the drift in the Zeeman laser frequency.

## 6.3   MOL and MOC

The MOL and the MOC use the same laser, that is frequency locked close to resonance ($\Delta_L = -2\Gamma$) by saturated absorption spectroscopy, as shown in Fig. 2.6. Again, an optical isolator (ConOptics model 715) and an additional half wave plate (Eksma) are used behind the laser. The laser power is distributed between the MOL and MOC by a variable ratio beam splitter, sending approximately 35% to the MOL and 65% to the MOC.

# 7   Beam diagnostics

To test the performance of the individual laser cooling sections we use either wire scanners or "knife-edge" scanners. A metastable helium atom in the $\{2s\}^3S_1$ state carries 20 eV of internal energy, enabling the Auger emission of an electron upon impact on a metal surface (typical workfunction of 5 eV) with near unity efficiency. Measuring the Auger current gives the number of metastables per second. The efficiency for impact on stainless steel is found to be nearly the same for metastable helium atoms in the $\{2s\}^3S_1$ and $\{2s\}^1S_0$ state and ranges between 0.70 and 0.95 [27]. In the rest of this chapter we will assume an efficiency of 1, resulting in a lower limit for all the measured beam fluxes.

   An artist's impression of a wire scanner is shown in Fig. 2.7(a). Two stainless steel
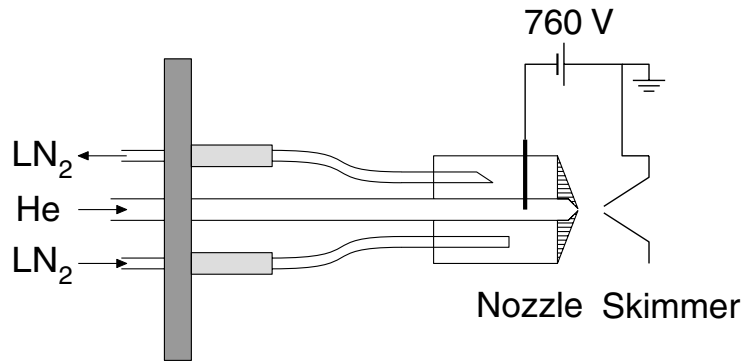
Figure 2.8: The discharge-excited metastable atom source with liquid nitrogen cooling. The discharge is drawn from the electrode through the nozzle to the grounded skimmer.

detection wires of 0.1 mm diameter are mounted on a single, computer-controlled, linear translator. The two wires are placed under right angles with respect to each other, allowing the simultaneous measurement of the beam profile in two dimensions. The use of two wires also allows us to measure the position of the atomic beam with respect to the center-line of the setup. Thus, the proper functioning and alignment of a two-dimensional laser cooling section can be confirmed with just a single scan. A knife-edge scanner is depicted in Fig. 2.7(b). Knife-edge scanners are mounted on the same type of linear translators and can be used to measure integrated beam profiles. Placing them in the beam allows for a fast measurement of the total beam flux.

# 8  Metastable atom source

The beam of metastable helium atoms is produced by a discharge excited supersonic source. The helium atoms are partially excited (fraction $\sim 10^{-4}$) to the metastable $\{2s\}^3S_1$ state by collisions with electrons in the DC discharge.

The source is cooled with liquid nitrogen to reduce the longitudinal velocity of the atoms. This reduces the effective source temperature from 400 K down to 150-200 K. An outline of the source is shown in Fig. 2.8. The source consists of two coaxial tubes: through the inner tube the gas is supplied, while the outer tube is filled with liquid nitrogen. The gas expands through a boron-nitride nozzle (0.1 mm diameter) that is in contact with the flat side of the liquid nitrogen reservoir. Boron-nitride is an electrical insulator with a good thermal conductance. The discharge is drawn from the electrode inside the inner tube through the nozzle to a skimmer, which is grounded. The electrode is at a constant negative voltage. The skimmer hole (1 mm diameter) is placed 10 mm behind the nozzle. Typical operating conditions of the source are a source pressure of 40 mbar and a 5 mA discharge current at a voltage of 760 V.

We use two knife-edge scanners to measure the center-line intensity of the source. They are placed, respectively, 350 mm and 400 mm behind the nozzle. Both knife-
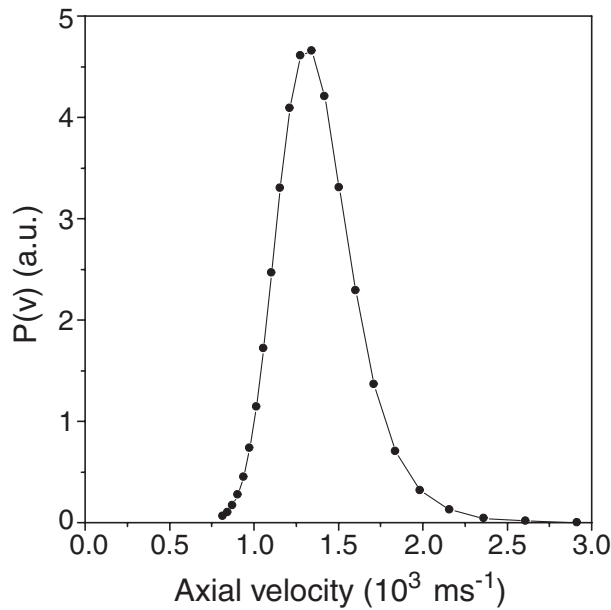
Figure 2.9: Axial velocity distribution of the metastable atoms produced by the source in the TOF-setup.

edge scanners are mounted orthogonally with respect to each other, which allows us to move the knife-edges through the atomic beam in two orthogonal transverse directions. The first knife-edge, at 350 mm, is put at a constant positive voltage of 500 V to draw away the electrons emitted from the second knife-edge scanner, hence preventing space charge buildup. By moving both scanners independently and measuring the Auger current on the second scanner, the center-line intensity of the source is found to be $4 \times 10^{14}$ s$^{-1}$ sr$^{-1}$. This value contains an unknown contribution from both helium atoms in the metastable $\{2s\}^1S_0$ state and XUV-photons. Contributions of 3% and 10% have been reported previously [24, 28]. The knife-edge scanners were permanently removed from the setup after the measurement.

The atomic velocity distribution has been measured using a time-of-flight (TOF) technique [29]. This method involves a mechanical chopper and a metastable atom detector. The detector consists of a stainless steel plate and an electron-multiplier and is situated downstream of the chopper wheel at a distance of 2.5 m. A multichannel analyzer accumulates the data. For the TOF-measurement, the source is placed in a separate vacuum setup, since the chopper wheel and the metastable atom detector can not be easily fitted into the final vacuum setup.

In the TOF-setup the source operates only in a stable way if we use slightly different operating conditions. Using a source pressure of 60 mbar and a 10 mA discharge current at a voltage of 800 V, the measured velocity distribution is centered at $v_\| = 1300$ ms$^{-1}$ with $\sigma v_\| = 210$ ms$^{-1}$. This distribution is shown in Fig. 2.9. Using the enthalpy balance, we can calculate the reservoir temperature $T_0$ of the gas just before it expands through the nozzle: $T_0 = 190$ K. The increase with respect to the liquid nitrogen temperature is caused by heating of the gas by the discharge. Under these operating conditions the center-line intensity is found to be

$2 \times 10^{14}$ s$^{-1}$ sr$^{-1}$ [21, 22].

In the final setup we use a discharge current of only 5 mA, which is half the value used in the TOF-setup. Rooijakkers [28] used a similar source for metastable helium atoms and found that reducing the the current from 10 to 5 mA reduces both the most probable longitudinal velocity and the velocity spread by 10% (in his case from $v_{\parallel} = 1250$ ms$^{-1}$ down to $v_{\parallel} = 1130$ ms$^{-1}$). Applying this result to our setup gives a velocity distribution centered at $v_{\parallel} = 1175$ ms$^{-1}$ with $\sigma v_{\parallel} = 190$ ms$^{-1}$ under normal operating conditions.

# 9    Two-dimensional collimation of the atomic beam

The atoms that leave the source and pass the skimmer form a beam with a maximum divergence angle of 50 mrad. The divergence angle is defined as the angle between the atomic beam axis and the velocity vector of the atom. Under these conditions, the atomic beam diameter will increase by 100 mm for each meter of flight, resulting in a severe decrease of the center-line beam brightness. By placing a two-dimensional Doppler cooling section directly behind the skimmer, the transverse velocity spread (and thus the beam divergence) can be drastically reduced. It produces a collimated beam of atoms and is therefore called the collimator.

Apart from the Zeeman slower, all the laser cooling sections in this chapter operate in two dimensions. For simplicity, we will always describe their theory of operation in just a single dimension. The generalization to two dimensions can not be done in a straightforward way. Usually, the one-dimensional version works better in one dimension than the two-dimensional version does in either of the two dimensions. This is directly related to the fact that the atom has to "divide its time" between the two cooling laser pairs.

## 9.1    Theory of operation

Ideally, the collimated atomic beam contains a large number of atoms and has a low divergence. The beam flux is proportional to the square of the capture angle $\theta_c = v_c/v_{\parallel} = -\Delta_L/kv_{\parallel}$. The decrease in beam divergence is determined by the damping coefficient $\beta$, as described in Eq. 2.2. Although a large laser detuning results in a high beam flux, it also causes a relatively high beam divergence, due to the low value of $\beta$. Alternatively, choosing $\Delta_L = -\Gamma/2$ results in the best collimation at the expense of a high beam flux.

This problem can be solved by using the so-called "curved wavefront" technique [30, 31], which is schematically depicted in Fig. 2.10. At the beginning of the cooling section, the propagation vector $\vec{k}$ of the light field is under a small angle $\alpha$. Due to the curvature of the wavefront the angle $\alpha$ is gradually reduced until it reaches zero at the end of the cooling section. This effectively produces a spatially chirped laser detuning, that ranges from $\Delta_L - kv_{\parallel}\alpha$ at the beginning of the light field to $\Delta_L$ at the end of the light field. Thus, at the beginning of the light field, the atoms with velocity $v_{\perp} = -\Delta_L/k + v_{\parallel}\alpha$ experience the maximum decelerating force, as can
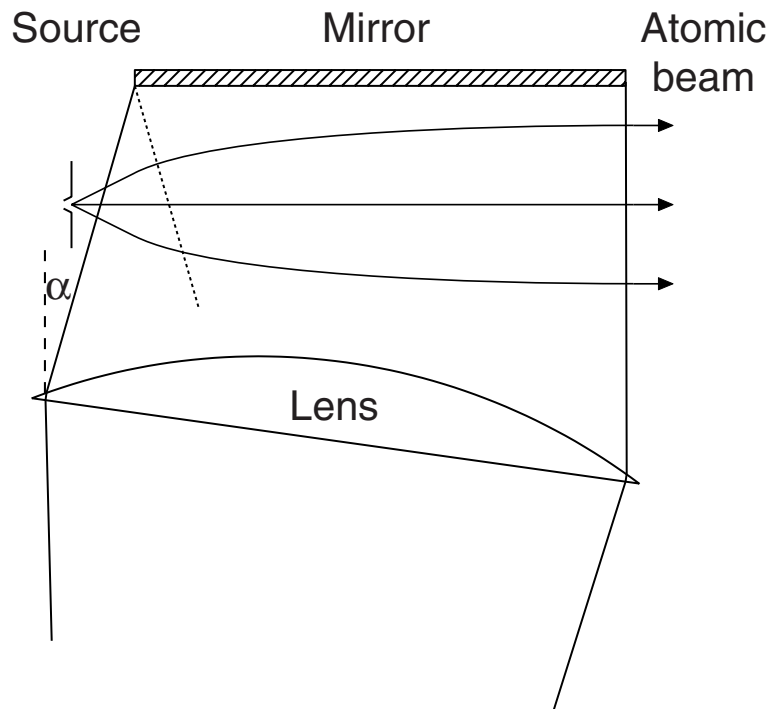
Figure 2.10: Collimation with a curved wavefront technique. The initial "chirp" angle $\alpha$ is not drawn to scale.
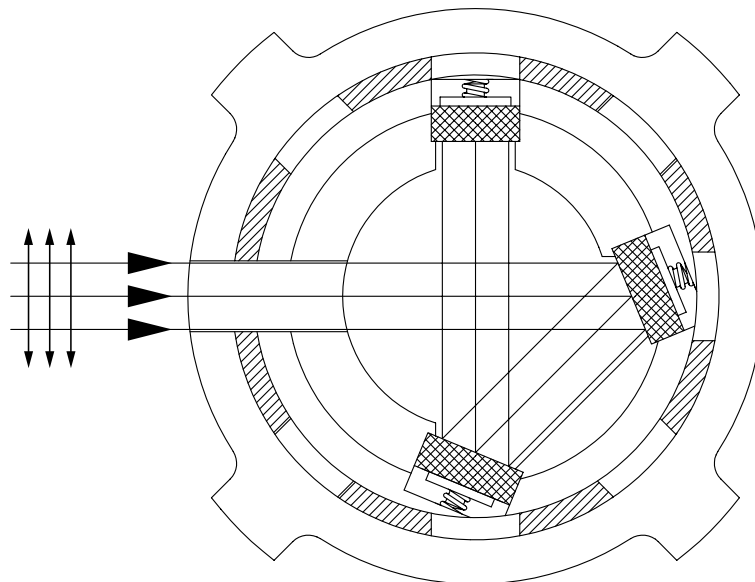


Figure 2.11: Collimator mirror section. Three mirrors are used to recycle a single laser beam such that it illuminates the atomic beam from four sides. The arrows indicate the orientation of the linear polarization of the light.

be seen from Eq. 2.1. This sweeps the atoms to a lower transverse velocity, where they pile up with the atoms originally occupying this lower velocity class. The spatial chirp keeps the atoms at resonance, such that all the atoms within the initial capture angle ($\theta_c = -\Delta_L/kv_{\parallel} + \alpha$) finally end up at $v_{\perp} = -\Delta_L/k$. Ideally, with $\Delta_L = -\Gamma/2$, the atoms feel both counterpropagating laser beams at the end of the cooling section, resulting in a beam divergence that is limited by the Doppler velocity $v_D$.

The atoms can only "lock" to the chirped resonance velocity if the initial angle $\alpha$ is limited to

$$\alpha \leq \alpha_{max} = \frac{\hbar k \Gamma L}{2Mv_{\parallel}^2},$$
(2.3)

where $L$ is the length over which the atoms interact with the light field. For $L = 165$ mm and $v_{\parallel} = 1175$ ms$^{-1}$ we find $\alpha_{max} = 56$ mrad. Numerical simulations of such a one-dimensional collimator for He* reveal that values up to $\alpha = 25$ mrad provide good locking [21, 22]. Due to the stronger radiation force and lower beam velocity, capture angles up to 100 mrad have been realized for Ne* [11].

## 9.2   Mirror section

The collimator laser beam is recycled by three mirrors (see Fig. 2.11), providing two orthogonal pairs of counterpropagating beams from one input beam in order to minimize the required laser power. The mirrors are gold coated (98% reflectivity for $\lambda = 1083$ nm) and can be illuminated over a maximum length $L = 165$ mm, given by the size of the AR-coated input window ($165 \times 15$ mm$^2$). The dimensions of the laser beam right outside the vacuum are: $2w_z = 192$ mm and $2w_y = 6$ mm, with the $z$-dimension along the atomic beam axis. For expanding the beam to this $z$-dimension we use two cylindrical lenses. As a high-quality wavefront is not necessary, we use a machined and subsequently polished plexiglass lens for the largest cylindrical lens. In the $y$-dimension we use an anamorphic prism pair (Melles-Griot) to expand the beam.

The laser light is linearly polarized orthogonal to the atomic beam axis, as indicated by the arrows in Fig. 2.11. With 21 mW of laser power in the vacuum we can achieve an average saturation parameter $\langle s \rangle = \langle I \rangle / I_{0,\pi} = 7$, with $I_{0,\pi} = 2.78$ W/m$^2$ for linearly polarized light.

## 9.3   Diagnostics

The performance of the collimator is measured using two wire scanners, both of the type as shown in Fig. 2.7(a). The wire scanners constitute a permanent diagnostic tool and are positioned, respectively, 1.90 m and 3.85 m behind the end of the collimator. This far away from the source, particles that are not captured by the collimator give a negligible contribution to the Auger current. The wire scanners are used to fine-tune the alignment of the light fields in the mirror section, giving optimum collimation.

Figure 2.12(a) shows the measured beam profiles for $\alpha = 12$ mrad and $\Delta_L = -2\Gamma$. Due to the 3 MHz spectral linewidth of the laser, this is the minimum achievable de-
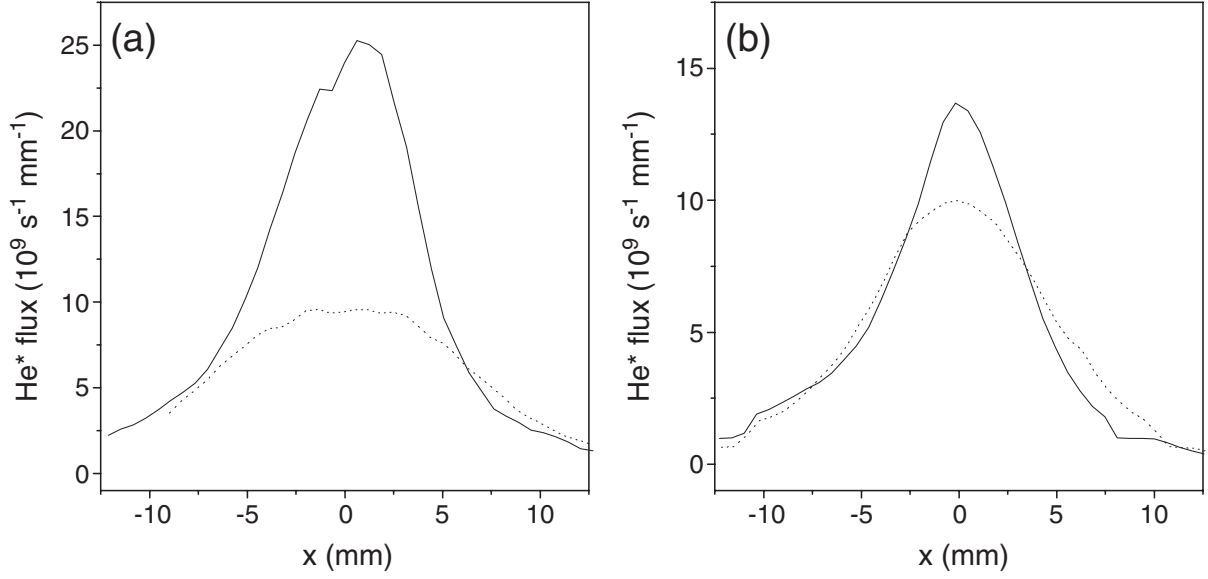
Figure 2.12: One-dimensional beam profile of the collimated atomic beam for $\alpha = 12$ mrad and $\Delta_L = -2\Gamma$ (a) and $\alpha = 0$ mrad and $\Delta_L = -3\Gamma$ (b). The profiles are measured with a wire scanner positioned 1.90 m (solid line) and 3.85 m (dotted line) behind the end of the collimator.

tuning. A smaller detuning results in the presence of blue-detuned light, heating the atomic beam as confirmed by the experiment. Figure 2.12(b) shows the measured beam profiles for $\alpha = 0$ mrad and $\Delta = -3\Gamma$, which was found to be the optimum detuning for a flat wavefront. The properties of the collimated beam are shown in Table I. Although the curved wavefront technique can capture more atoms, the resulting divergence is 2.4 times larger than in the case of the flat wavefront technique. With $v_\parallel = 1175$ ms$^{-1}$ we obtain 2.9 times the Doppler velocity for the flat wavefront and 7.0 times the Doppler velocity for the curved wavefront.

The two-dimensional molasses with a relative large value of $\langle s \rangle$ probably prevents us from reaching the 1D Doppler limit. The high atomic beam divergence in the curved wavefront case is probably caused by the large detuning, imposed by the spectral linewidth of the laser: the relative low decelerating force prevents the atoms with a high transverse velocity from properly locking to the chirped resonance veloc-

Table I: Properties of the collimated atomic beam *with* a curved wavefront ($\alpha = 12$ mrad) and *without* a curved wavefront ($\alpha = 0$ mrad). All numbers represent measured values except $\alpha$ and $\Delta_L$.

| $\alpha$ (mrad) | $\Delta_L$ ($\Gamma$) | $\dot{N}_{1.90m}$ ($10^{11}$ s$^{-1}$) | $\dot{N}_{3.85m}$ ($10^{11}$ s$^{-1}$) | $T = \frac{\dot{N}_{3.85m}}{\dot{N}_{1.90m}}$ | $\theta_c$ (mrad) | $\sigma v_\perp / v_\parallel$ (mrad) |
|---|---|---|---|---|---|---|
| 12 | -2 | 2.6 | 1.5 | 0.58 | 13 | 1.7 |
| 0 | -3 | 1.2 | 1.2 | 0.96 | 9 | 0.70 |

ity. With a narrow-band Nd:LMA laser and a curved wavefront Rooijakkers *et al.* [31] obtained a capture angle of 14 mrad, while reaching 2.5 times the Doppler velocity.

In the fully operational beam setup, the flat wavefront technique gives a slightly higher count rate on the 2D-detector than the curved wavefront technique. Evidently, the Zeeman slower and the compressor benefit more from the lower beam divergence than they suffer from the lower beam flux. Thus, we will use the flat wavefront technique for the collimator in the rest of this thesis.

# 10   Zeeman slower

The atoms, leaving the collimator at thermal velocities, must be decelerated in a controlled way in order to make a slow ($v_\parallel < 400$ ms$^{-1}$) and monochromatic ($\sigma v_\parallel / v_\parallel < 2 \times 10^{-2}$) atomic beam. In all the experiments in this thesis we will use $v_\parallel = 250$ ms$^{-1}$.

When decelerating atoms with resonant laser light one faces the problem that the changing Doppler shift $\Delta_D$ shifts the atom out of resonance after a few absorption/spontaneous emission cycles. Two main techniques have been devised to keep the atoms in resonance during the whole slowing process. In the first one, the laser frequency $\Delta_L$ is chirped in time to match the changing resonance velocity [32]. A disadvantage of this technique is that it generally produces a time structure in the atomic beam. The second technique keeps the atoms in resonance by using a spatial compensation of the atomic transition frequency via the Zeeman effect [14]. It employs a magnetic field that changes along the deceleration path. This technique produces a continuous beam of slow atoms and will be used in this chapter.

## 10.1   Theory of operation

The Zeeman slower uses the resonant radiation force to slow down the atoms by a counterpropagating laser beam. The distance $\Delta z$ required to slow down atoms from an initial longitudinal velocity $v_{\parallel,i}$ to a final velocity $v_{\parallel,f}$ with a constant deceleration can be calculated to be

$$\Delta z = \frac{M(v_{\parallel,i}^2 - v_{\parallel,f}^2)}{\hbar k \Gamma \eta}, \tag{2.4}$$

in which $0 \leq \eta \leq 1$ is the fraction of the maximum radiation force used in the slowing process. Slowing He* atoms from 1300 ms$^{-1}$ down to 250 ms$^{-1}$ using the maximum achievable deceleration ($\eta = 1$) on the $\{2s\}^3S_1 \rightarrow \{2p\}^3P_2$ transition gives $\Delta z = 1.7$ m.

In the Zeeman slower circularly polarized $\sigma^+$-light is used. The atoms are thus pumped to the $|m_g = +1\rangle \leftrightarrow |m_e = +2\rangle$ sublevel system. In order to stay resonant during the whole slowing process they have to fulfill the resonance condition $\Delta_B = \Delta_L + \Delta_D$ for each position $z$, giving

$$kv_\parallel(z) = -\Delta_L + \frac{\mu_B}{\hbar}B(z), \tag{2.5}$$

where $\Delta_B = \mu_B B(z)/\hbar$ is the Zeeman shift due to the magnetic field $B(z)$. In order to achieve a constant deceleration, the magnitude of the magnetic field $B(z)$ has to
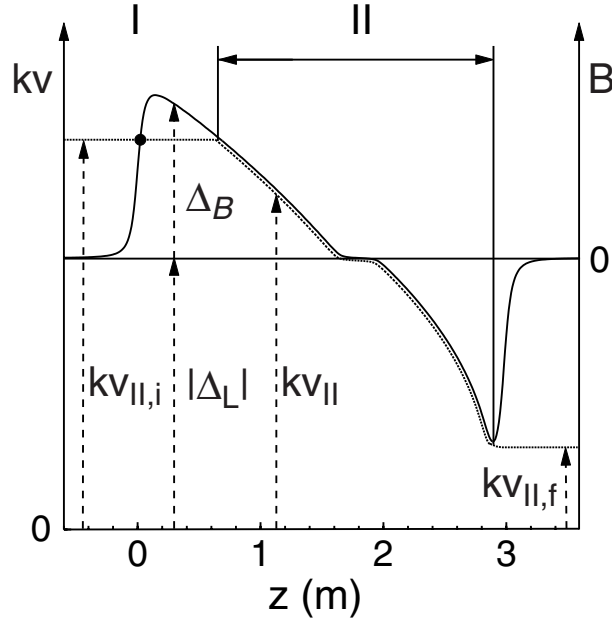
Figure 2.13: Schematic representation of the slowing process in a "mid-field zero" Zeeman magnet. A metastable helium atom with an initial velocity $v_{\parallel,i}$ enters the slower in region I and is optically pumped to the $|m_g = +1\rangle$ state. In region II, the atom follows the resonance velocity $v_\parallel$ dictated by the magnetic field until it reaches the final velocity $v_{\parallel,f}$. Here, the resonance velocity swiftly increases and the atom is no longer decelerated.

follow

$$B(z) = B_0 + B_1\sqrt{1 - \frac{z}{z_0}}, \tag{2.6}$$

where $B_0$ is the offset magnetic field and $B_1$ is the magnetic field range, which determines the maximum initial atomic velocity that is captured: $v_{\parallel,c} = \mu_B B_1/(\hbar k)$. The offset field $B_0$ is related to the laser detuning $\Delta_L$ via: $\mu_B B_0/\hbar = \Delta_L$. Here, $z_0$ is the position where the atomic velocity reaches zero if the deceleration would continue.

The slowing process can be understood from Fig. 2.13. Consider an atom entering the slower with velocity $v_{\parallel,i} < v_{\parallel,c}$ (dotted line). The solid line represents the velocity $v_\parallel$ that is resonant with the laser at position $z$, as given by Eq. 2.5. In region I the atom briefly becomes resonant with the rising edge of the magnetic field. This short interaction pumps the atom to the $|m_g = +1\rangle$ state. Some distance later the atom is resonant again, but will now follow the resonance velocity dictated by the magnetic field. If the gradient of the magnetic field is not too large, the atom is continuously decelerated and is able to follow the decreasing resonance velocity (region II). At the end of region II the magnetic field gradient swiftly changes sign. This way, the atoms will lose resonance very abruptly, which gives a well-defined final velocity $v_{\parallel,f}$.

In a practical setup, the values of $B_1$ and $z_0$ (in Eq. 2.6) are chosen such that atoms can follow the decreasing resonance velocity with a deceleration that is smaller than

Table II: Characteristics of the Zeeman slower.

|  | solenoid 1 | solenoid 2 |
|---|---|---|
| length | 1.6 m | 1.0 m |
| max. number of layers | 20 | 32 |
| wire thickness | 2.0 mm | 2.0 mm |
| inner diameter | 100 mm | 100 mm |
| outer diameter | 180 mm | 228 mm |
| max. field strength/current | $1.06 \times 10^{-2}$ T/A | $-1.53 \times 10^{-2}$ T/A |
| current | 3.0 A | $-2.35$ A |
| maximum B | $3.18 \times 10^{-2}$ T | $-3.59 \times 10^{-2}$ T |
| $\Delta_{\mathrm{L}}/(2\pi)$ | $-740$ MHz | $-740$ MHz |
| capture velocity | 1300 ms$^{-1}$ |  |
| final velocity |  | 250 ms$^{-1}$ |

the maximum achievable deceleration. This provides a safety margin that compensates for statistical fluctuations in the decelerating force, the finite laser intensity, and imperfections in the wavefront of the laser beam [33].

## 10.2  Implementation

In our setup, we create the required magnetic field using two solenoids, producing fields in opposite directions. In between the solenoids, the magnetic field is equal to zero. This "mid-field zero" configuration allows us to decelerate the atoms over a large velocity range using only moderate electrical currents. It also avoids that a substantial amount of atoms are lost at a level crossing between the $\{2\mathrm{p}\}^3\mathrm{P}_2\ |m_e = +2\rangle$ state and the $\{2\mathrm{p}\}^3\mathrm{P}_1\ |m_e = 0\rangle$ state at $B = 5.50 \times 10^{-2}$ T, as reported by Rooijakkers [28].

The dimensions of the solenoids and other characteristics are included in Table II. For the capture velocity and the final velocity we choose 1300 ms$^{-1}$ and 250 ms$^{-1}$, respectively. The length of both solenoids is chosen such that the atoms can follow the magnetic field with a fraction 2/3 of the maximum radiation pressure induced deceleration. This requires that $\Delta z = 2.6$ m. The solenoids are water cooled and dissipate around 450 W in total. The Zeeman slower produces stray magnetic fields in the collimator and in the MOL. These fields are canceled by extra compensating solenoids mounted at the front and at the end of the Zeeman slower. The fields of the compensating magnets lower the maximum axial magnetic fields in the two Zeeman solenoids by less than 5 Gauss. By shunting the appropriate solenoids with a resistor, the whole Zeeman slower, including compensating solenoids, can be operated from a single power supply.

The Zeeman laser is detuned by $\Delta_{\mathrm{L}}/(2\pi) = -740$ MHz. Around 18 mW of $\sigma^+$-polarized laser light is coupled into the Zeeman slower through a mirror with a 1 mm diameter orifice in the center. This mirror is positioned directly behind the

MOL/MOC-combination, which compresses the atomic beam and funnels it through the orifice. Using an anamorphic prism pair and a telescope of spherical lenses the laser beam is given the following dimensions: $2w_z = 2w_y = 50$ mm, resulting in an average saturation parameter of $\langle s \rangle = \langle I \rangle / I_{0,\sigma} = 4$, with $I_{0,\sigma} = 1.67$ W/m$^2$ for circular polarized light. The vacuum entrance window clips the beam to 35 mm diameter. By adjusting the telescope, the laser beam is focused onto the skimmer to match the atomic beam divergence.

## 10.3   Absorption diagnostics

Several techniques can be used to measure the velocity distribution $P(v_{\parallel})$ of the atoms that leave the Zeeman slower. Normal time-of-flight techniques, which require a mechanical chopper behind the Zeeman slower, can not be used since the chopper wheel and the metastable atom detector will inevitably block the Zeeman laser. Rooijakkers [28] places the chopper wheel at the entrance of the Zeeman slower and uses a "transparent" detector. Since the velocity of the atoms is altered after passing the chopper wheel, the resulting TOF-signals are hard to interpret. Mastwijk [24] uses a laser to deflect atoms from the slow beam into a channeltron positioned 0.9 m downstream, 5 mm off-axis. Simulations [21] show that, in our case, the atomic beam will have an rms width of 18 mm at the end of the Zeeman slower. This makes proper use of the deflection technique in our setup virtually impossible.

More promising is the technique in which a probe laser traverses the atomic beam under an angle. By scanning the laser in frequency and detecting the corresponding fluorescence, the velocity distribution can be obtained. The low detection efficiency of photomultipliers at 1083 nm prevents us from measuring the fluorescence directly. Instead, we will measure the absorption of the probe laser, which is equivalent to the total amount of fluorescence emitted by the atoms. Since the relative absorption is only in the order of $10^{-3}$, considerably lower than the relative power variations of the probe laser in time, we use a frequency modulation (FM) technique [34].

Figure 2.14 shows the mirror section that guides the probe laser beam through the setup. The probe laser traverses the atomic beam four times: twice under normal incidence and twice under 45°. This mirror section temporarily replaces the mirror section of the MOL. The ideal geometry, in which the probe laser traverses the atomic beam only twice, could not be implemented in our setup due to limitations in the position and size of the entrance window.

Atoms will absorb light from the probe laser if $\Delta_L = \vec{k} \cdot \vec{v}$. Thus, the two probe laser beams under 45° measure $P(v_{45°})$, with $v_{45°} = (v_{\parallel} + v_{\perp})/\sqrt{2}$. The two probe laser beams under normal incidence measure $P(v_{\perp})$. Since $P(v_{\perp})$ is centered around $v_{\perp} = 0$, atoms with a low transverse velocity will always absorb from both normal incidence beams at the same time. The sign difference in the Doppler shift prevents atoms from absorbing from both 45° beams at the same time. If both $P(v_{45°})$ and $P(v_{\perp})$ are Gaussian distributions and if $v_{\parallel}$ and $v_{\perp}$ are independent random variables, then one can easily calculate $P(v_{\parallel})$. The distribution $P(v_{\parallel})$ will also be Gaussian with
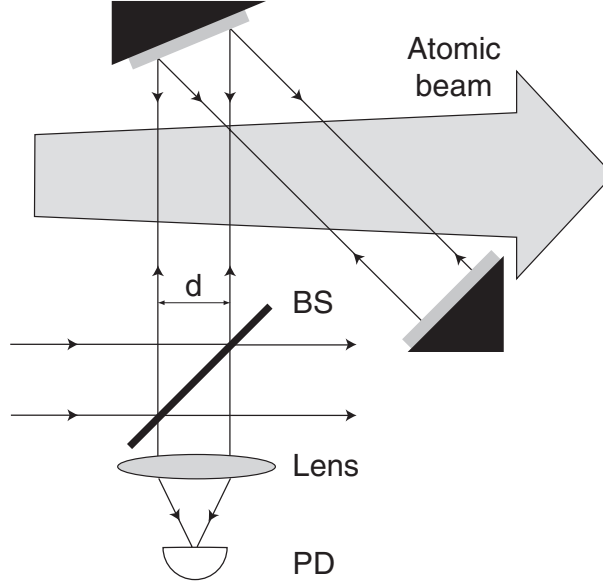
Figure 2.14: Mirror section that guides the probe laser beam through the setup. A beam splitter (BS) splits off the probe laser beam of dimensions $d \times d$. The probe light traverses the atomic beam four times: twice under normal incidence and twice under $45°$. Then, it leaves the vacuum and is focused onto a photo-detector (PD).

$\langle v_\parallel \rangle = \sqrt{2}\langle v_{45°} \rangle$. The rms velocity spread $\sigma v_\parallel$ can be calculated to be:

$$\sigma v_\parallel = \sqrt{2(\sigma v_{45°})^2 - (\sigma v_\perp)^2}. \tag{2.7}$$

The relative absorption $A_R^i(\Delta_L)$ from a single, weak ($s \ll 1$) probe laser beam $i$ ($i \in \{45°, \perp\}$) can be calculated to be

$$A_R^i(\Delta_L) = \frac{\dot{N}\hbar\omega_0 \Gamma \epsilon_i}{2I_0 d \langle v_\parallel \rangle} \int dv_i P(v_i) C(k_i v_i - \Delta_L), \tag{2.8}$$

with $\dot{N}$ the atomic flux that passes the probe beam of dimensions $d \times d$, $\hbar\omega_0$ the photon energy, $I_0$ the saturation intensity and $\epsilon_i$ a constant ($\epsilon_{45°} = \sqrt{2}$ and $\epsilon_\perp = 1$). The function $C(k_i v_i - \Delta_L)$ is the convolution between the Lorentzian shape of the atomic transition and the (known) frequency spectrum of the laser $S(\omega)$. Here, we assume that the probe beam dimension $d$ is smaller than the width of the atomic beam.

The probe laser is frequency modulated with a modulation depth $\widetilde{\Delta}_L$ and modulation frequency $f_{mod}$, giving an instantaneous detuning $\Delta_L = \langle\Delta_L\rangle + \widetilde{\Delta}_L \cos(2\pi f_{mod} t)$. With the use of a lock-in amplifier we can measure the amplitude of the relative absorption signal $\widetilde{A}_R = \sum_i \widetilde{A}_R^i$. For a small modulation depth we effectively measure the derivative of $A_R(\Delta_L) = \sum_i A_R^i(\Delta_L)$ with respect to $\Delta_L$:

$$\frac{\widetilde{A}_R}{\widetilde{\Delta}_L} \approx \frac{\partial A_R(\Delta_L)}{\partial \Delta_L}. \tag{2.9}$$

Integration with respect to $\Delta_L$ immediately gives $A_R(\Delta_L)$. This can then be fitted with the use of Eq. 2.8 to determine $\dot{N}$, $P(v_{45°})$ and $P(v_\perp)$.
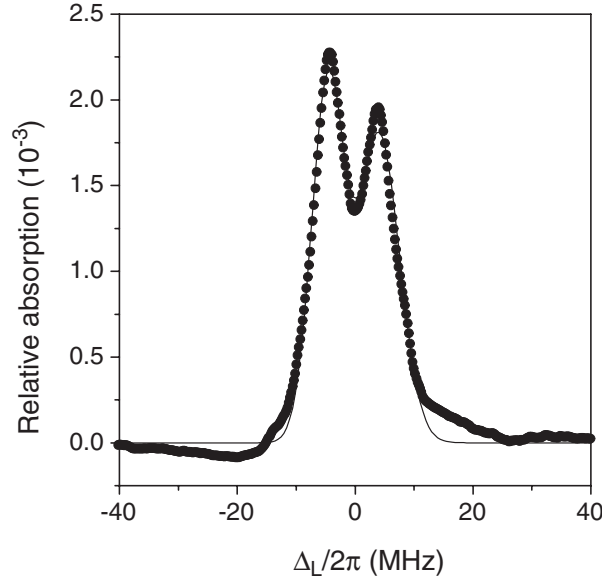
Figure 2.15: Relative absorption profile around resonance when the collimator is turned on and the Zeeman slower is turned off: thermal atoms absorb light from the two perpendicular probe beams. Solid circles: measured data points, solid line: fit using Eq. 2.8.

We use the laser for the MOL/MOC as the probe laser. The probe beam is linearly polarized ($I_0 = I_{0,\pi} = 2.78$ W/m$^2$). We choose $s = 0.033$ and $d = 20$ mm. The laser is modulated with a frequency $f_{\mathrm{mod}} = 1025$ Hz and an amplitude $\tilde{\Delta}_{\mathrm{L}}/(2\pi) = 1.2$ MHz. The probe beam is focused on an InGaAs photo-detector (Hamamatsu G6854-01), equipped with a two-stage pre-amplifier. The detector has both a DC- and an AC-coupled output. The DC-coupled signal is proportional to the total probe laser power. The AC-coupled signal is proportional to the FM-part of the absorption signal and is fed into the lock-in amplifier. The DC-coupled signal and the output of the lock-in amplifier are fed into the computer that also controls the frequency scanning of the probe laser. The computer program uses Eq. 2.9 and a numerical integration routine to calculate $A_{\mathrm{R}}(\Delta_{\mathrm{L}})$.

First, we determine $\dot{N}$ and $P(v_\perp)$ of the collimated, thermal atomic beam. Figure 2.15 shows the relative absorption profile around resonance when the collimator is turned on and the Zeeman slower is turned off. The double peak structure is caused by an 8 mrad angle between the two perpendicular probe beams. This allows us to measure the absorption from both probe beams separately. Fitting the data with Eq. 2.8 gives: $\dot{N}_{\mathrm{thermal}} = 3.6 \times 10^{11}$ s$^{-1}$ and $\sigma v_\perp = 1.6$ ms$^{-1}$. These values are a factor 2 to 3 higher than the ones found with the wire scanners. The limited SNR obtained with this FM absorption technique does not allow for determining the broad forward velocity distribution of the thermal beam.

By turning on the Zeeman slower, the atoms are slowed down and the atomic beam divergence increases. Figure 2.16 shows the relative absorption profiles when both the collimator and the Zeeman slower are turned on. Now, both the absorption from the perpendicular and the 45° probe beams can be measured. Data analysis
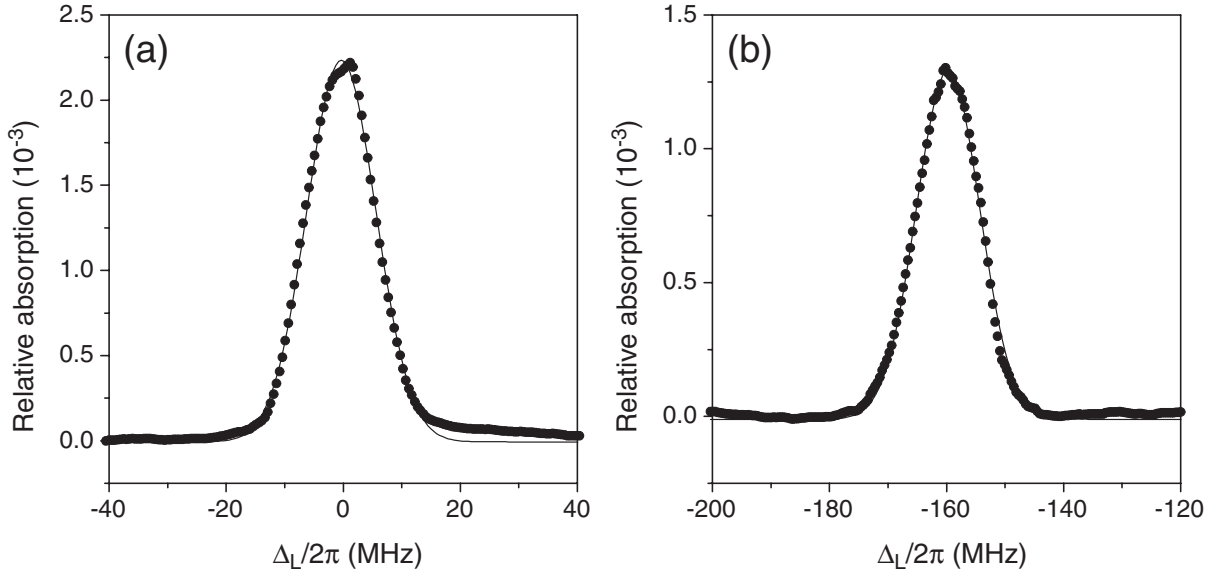
Figure 2.16: Relative absorption profile from the two perpendicular probe beams (a) and one 45° probe beam (b) when both the collimator and the Zeeman slower are turned on. Now, slow atoms absorb probe light. Solid circles: measured data points, solid line: fit using Eq. 2.8.

gives: $\dot{N}_{\text{slow}} = 8 \times 10^{10}$ s$^{-1}$, $\sigma v_\perp = 6.0$ ms$^{-1}$, $\sigma v_\parallel = 4.8$ ms$^{-1}$ and $v_\parallel = 245$ ms$^{-1}$. Due to the finite size of the Zeeman slower laser at the end of the second solenoid, the slow atomic beam can not exceed a diameter of 30 mm. We estimate that the 20 mm probe laser beam addresses 70% of the slow atoms. Thus, the Zeeman slower produces approximately $1.1 \times 10^{11}$ He* s$^{-1}$ at $v_\parallel = 245$ ms$^{-1}$, with $\sigma v_\parallel / v_\parallel = 1.9 \times 10^{-2}$.

In chapter 3 we will use a completely different approach to measure the forward velocity distribution of the slow atomic beam. That method is more accurate than the FM absorption technique, but needs a fully operating beam machine. It gives: $v_\parallel = 247$ ms$^{-1}$ and $\sigma v_\parallel / v_\parallel = 1.5 \times 10^{-2}$.

## 11   Two-stage atomic beam compression

The Zeeman slower produces a rather broad (30 mm diameter) and divergent (25 mrad rms) atomic beam, resulting in a low beam brightness. The beam brightness can be increased significantly by funneling the atoms into a narrow and collimated beam. This is done with a two-stage beam compression technique. Each stage consists of a two-dimensional MOT, operating in its own regime. The first stage, formed by the MOL, captures the broad atomic beam and focuses the atoms into the capture area of the second stage, the MOC. Here, the atoms are funneled into a narrow and collimated atomic beam. The combined system of MOL and MOC is called the compressor. Figure 2.17 shows an overview of the atomic trajectories in the compressor.

MOL          MOC



Figure 2.17: Atomic trajectories in the compressor, that consists of a magneto-optical lens (MOL) and a magneto-optical compressor (MOC).



Figure 2.18: Trapping scheme of a 2D-MOT. The two-dimensional quadrupole field is created by the four permanent magnets. The light field consists of two orthogonal $\sigma^+$-$\sigma^-$ laser pairs.

## 11.1   Theory of operation

A 2D-MOT is schematically depicted in Fig. 2.18. In each trapping dimension a molasses is formed by two counterpropagating $\sigma^+$- and $\sigma^-$-polarized laser beams. The position-dependence of the radiation force is 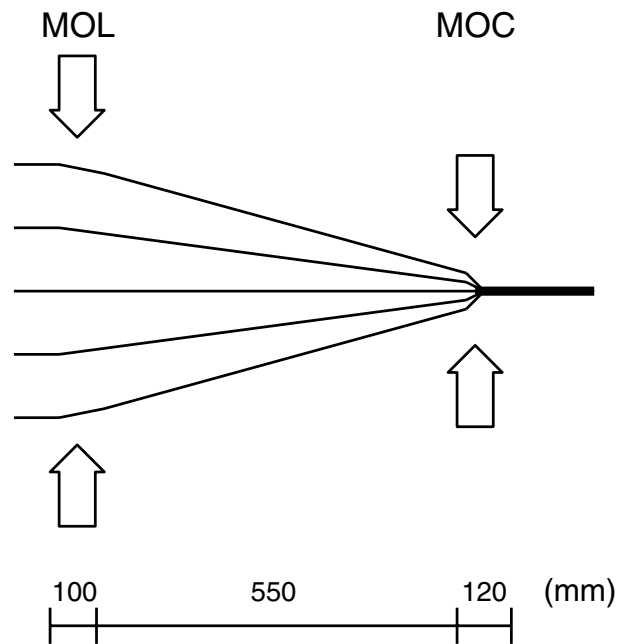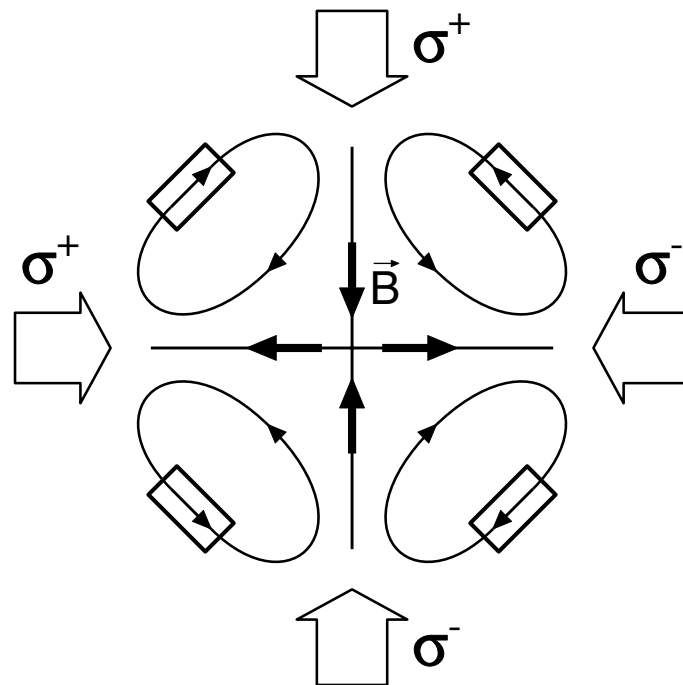produced by a magnetic quadrupole field, which creates a constant magnetic field gradient near the beam axis. At the position of the beam axis the magnetic field is exactly zero.

The essential properties of the 2D-MOT are most easily explained for an atom excited on a $J = 0 \rightarrow J = 1$ transition. In our case ($J = 1 \rightarrow J = 2$) additional optical pumping processes take place, that redistribute the atoms over the available magnetic sublevels. The principle of operation, however, stays the same.

For a single trapping dimension $x$ and a $J = 0 \rightarrow J = 1$ transition, the net radiation force equals [13]

$$F(x, v_x) = F_+(x, v_x) + F_-(x, v_x), \tag{2.10}$$

in which $F_\pm(x, v_x)$ is the force exerted by the $\sigma^\pm$ laser beam with

$$F_\pm(x, v_x) = \pm \frac{\hbar k \Gamma s}{2 \left(1 + s + \{2\Delta_\pm/\Gamma\}^2\right)}, \tag{2.11}$$

$$\Delta_\pm = \Delta_L \mp k v_x \mp \frac{\mu_B}{\hbar} \frac{\partial B}{\partial x} x, \tag{2.12}$$

where the effective detuning $\Delta_\pm$ contains the laser detuning $\Delta_L$, the Doppler shift due to the transverse velocity $v_x$, and the Zeeman shift due to the local magnetic field $B(x) = (\partial B/\partial x)x$. The sign difference in the Zeeman shift is caused by the fact that the $\sigma^+$-beam excites the $m_g = 0 \rightarrow m_e = +1$ magnetic subtransition, while the $\sigma^-$-beam excites the $m_g = 0 \rightarrow m_e = -1$ transition. For each position $x$ there exists an equilibrium velocity $v_{x,\text{eq}} = -(\mu_B/\hbar k)(\partial B/\partial x)x$ towards the beam axis, for which the two forces are balanced. For $\Delta_L < 0$ and $s \ll 1$ the cooling force can be approximated by $F = -\beta(v_x - v_{x,\text{eq}})$, which is very similar to Eq. 2.2. Again, this equation only holds for velocities below the capture velocity: $|v_x - v_{x,\text{eq}}| < v_c = -\Delta_L/k$. Thus, the motion of the atoms is locally "cooled" to the equilibrium velocity $v_{x,\text{eq}}$.

### MOL

The MOL uses a small magnetic field gradient $\partial B/\partial x$ to produce a thin lens for atoms. The lens effect is caused by the fact that the equilibrium transverse velocity $v_{x,\text{eq}}$ is proportional to the distance from the beam axis. The lens is thin, since the atoms hardly change their transverse position during interaction with the light field. The focal distance $f$ of the MOL can be calculated from the expression for $v_{x,\text{eq}}$ and is found to be

$$f = \frac{x v_\parallel}{v_{x,\text{eq}}} = \frac{\hbar k v_\parallel}{\mu_B \left(\frac{\partial B}{\partial x}\right)}, \tag{2.13}$$

with $v_\parallel$ the forward velocity of the atoms. In order to properly "lock" the atoms to $v_{x,\text{eq}}$, the magnetic field gradient $\partial B/\partial x$ is slowly increased from zero, at the beginning of the MOL, to a maximum value at the end of the MOL, which determines the focal length $f$.

**MOC**

In the MOC, the magnetic field gradient increases at a much higher rate along the beam axis $z$, i.e.: $\left(\frac{\partial^2 B_{\text{MOC}}}{\partial x \partial z}\right) \gg \left(\frac{\partial^2 B_{\text{MOL}}}{\partial x \partial z}\right)$. Only atoms relatively close to the beam axis can properly lock to the swiftly changing $v_{x,\text{eq}}$. These atoms are dragged inward and reach the beam axis before the end of the MOC. When they arrive at the beam axis both $x = 0$ and $v_{x,\text{eq}} = 0$. Thus, all the captured atoms pile up at the beam axis with a low transverse velocity. The final velocity spread and the size of the atomic beam produced by the MOC is determined by the velocity- and position-gradient of the force near the axis. A small laser detuning produces a cold atomic beam but results in a small capture velocity $v_{\text{c}}$. A high magnetic field gradient produces a narrow beam but results in a small spatial capture radius $x_{\text{c}}$ at the entrance, as can be seen from Fig. 2.19. This problem is solved by prefocusing the atoms, using the MOL, into the relative small spatial capture range of the MOC. This approach combines the large spatial capture range of the MOL with the strong compression capabilities of the MOC.

## 11.2   Implementation

**Mirror sections**

The two-dimensional $\sigma^+$-$\sigma^-$ configuration of the light fields, as required by a 2D-MOT, is produced by recycling a single $\sigma^+$-polarized laser beam in a special mirror section, as depicted in Fig. 2.20. Each mirror is coated with a HR polarization-maintaining coating for 1083 nm. The mirror section for the MOL is illuminated over a length of 100 mm ($2w_z = 120$ mm, $2w_y = 23$ mm and $\langle s \rangle = \langle I \rangle / I_{0,\sigma} = 2$), while the light field of the MOC extends over a length of 120 mm ($2w_z = 120$ mm, $2w_y = 23$ mm and $\langle s \rangle = \langle I \rangle / I_{0,\sigma} = 4$). The MOL/MOC laser detuning is set to the minimum achievable value of $\Delta_{\text{L}} = -2\Gamma$ (see section 9.3).

**Magnetic fields**

The magnetic quadrupole fields are created by four permanent magnets. The configuration of the magnets is shown in Fig. 2.18 and leaves enough space for the light fields. For the MOL, we use barium ferrite magnets ($40 \times 35 \times 10$ mm$^3$, 0.4 T magnetization). The magnets for the MOC are made of a Nd-Fe-B alloy ($70 \times 60 \times 30$ mm$^3$, 1.15 T magnetization). Figure 2.21 shows the measured on-axis field gradient along the light field for the MOL and the MOC. Up to 15 mm off-axis the field gradients are found to be perfectly constant. The MOL ends with a field gradient of 0.030 T/m, giving a focal length $f = 0.54$ m. The MOC, that starts 0.55 m behind the exit of the MOL, ends with a field gradient of 0.80 T/m.
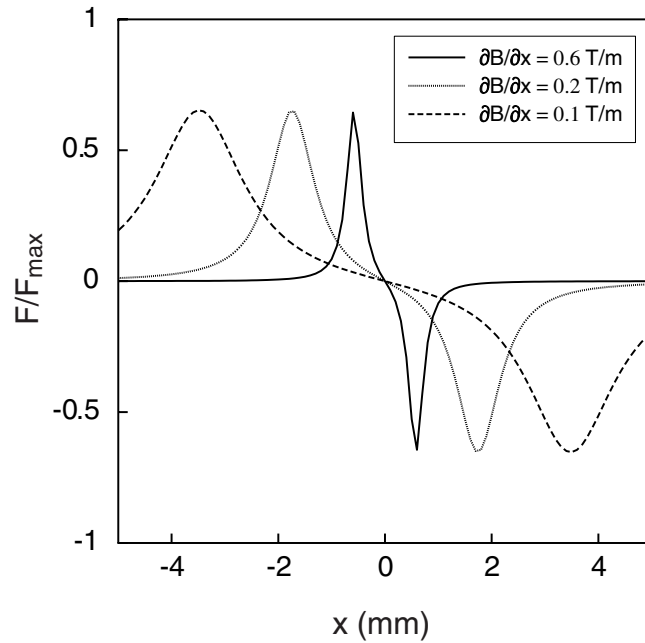
Figure 2.19: Position-dependence of the trapping force on an atom for $v_x = 0$ and different magnetic field gradients.
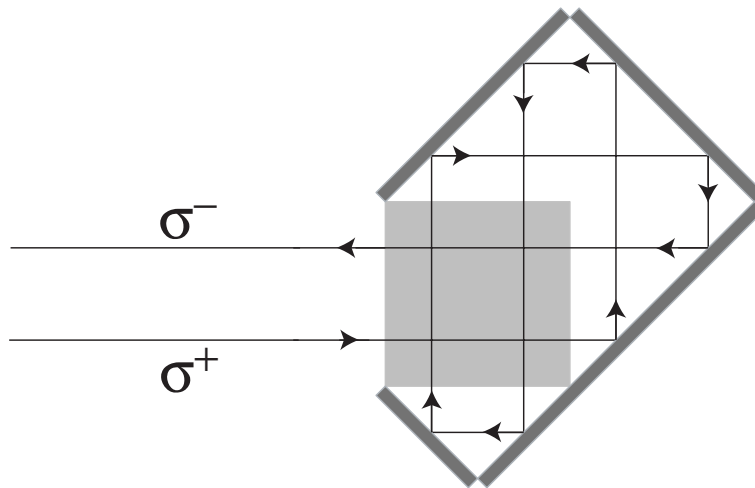


Figure 2.20: Mirror section that produces the two orthogonal $\sigma^+$-$\sigma^-$ laser pairs, required for the MOL and the MOC, from a single circular polarized laser beam. The shaded square indicates the cooling area.
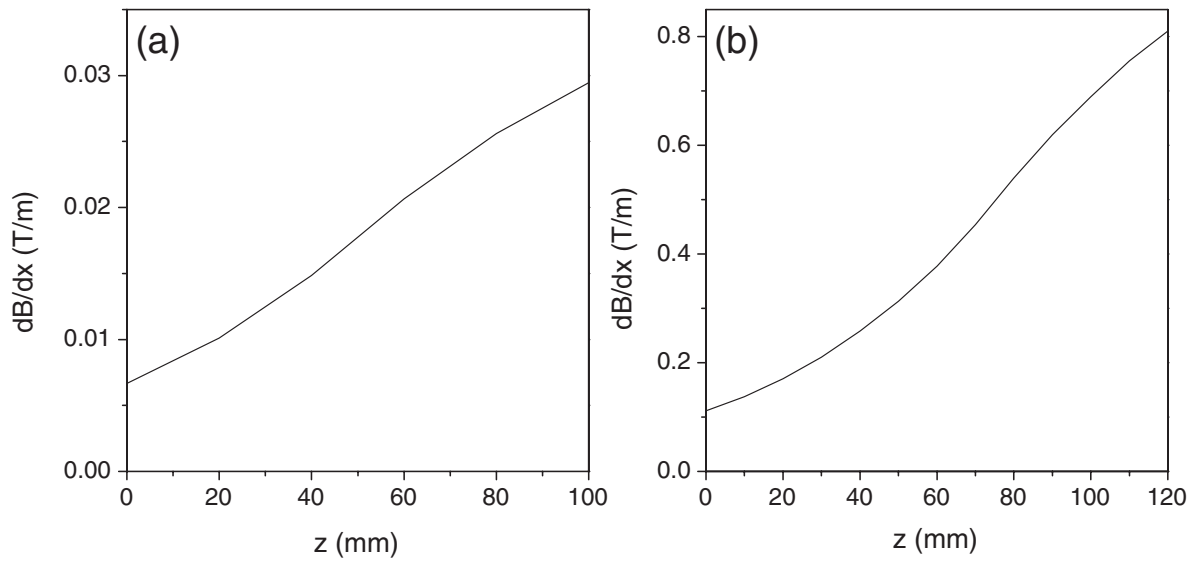
Figure 2.21: Measured on-axis magnetic field gradient in the MOL (a) and in the MOC (b). The light field extends over 100 mm in the MOL and 120 mm in the MOC.
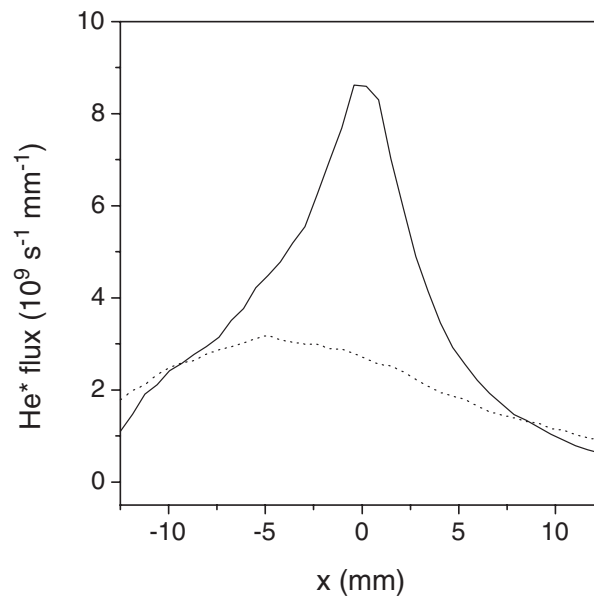


Figure 2.22: One-dimensional beam profile of the atomic beam after being focused by the MOL (solid line) and with the MOL turned off (dotted line). The profile is measured with a wire scanner positioned 0.50 m behind the end of the MOL, i.e., near the entrance of the MOC.

## 11.3   Diagnostics

Numerical simulations [21, 22] reveal that the spatial capture radius of the MOL exceeds 15 mm. Thus, the MOL should be able to capture all the slow atoms that leave the Zeeman slower. For the MOC, the simulations show that a 6 mm diameter beam can be compressed into a 0.2 mm diameter beam. These simulations were done for $\Delta_L = -3\Gamma$, resulting in a relative hot atomic beam that leaves the MOC. In the experiment we achieve the highest count rate on the 2D-detector with $\Delta_L = -2\Gamma$. Evidently, the smaller capture velocity $v_c$ is more than compensated for by the lower beam divergence.

The performance of the MOL is measured with a wire scanner positioned 0.50 m behind the end of the MOL, i.e., near the entrance of the MOC. Figure 2.22 shows the measured beam profiles when the MOL is turned on or off. From the measurement we estimate that the MOL focuses $2 \times 10^{10}$ He* s$^{-1}$ into the 6 mm capture diameter of the MOC. The total flux addressed by the MOL is $9 \times 10^{10}$ s$^{-1}$.

The performance of the MOL/MOC-combination is measured using two orthogonal knife edge scanners that are positioned behind the 1 mm orifice in the mirror of the Zeeman slower, i.e., 10 cm behind the end of the MOC. Both knife edge scanners contain an additional 60 $\mu$m wide slit. By moving both slits into the beam a movable $60 \times 60$ $\mu$m$^2$ aperture can be defined. In the actual experiments this aperture together with a second movable aperture (25 $\mu$m diameter), placed 2 m downstream, is used to obtain the sub-recoil collimated atomic beam.

The total flux $\dot{N}$ of the compressed beam can be measured with the first knife edge scanner. We find: $\dot{N} = 5.0 \times 10^9$ s$^{-1}$. Thus, approximately 4% of the atoms that leave the collimator reach the end of the compressor. By measuring the fraction of atoms that pass the first 60 $\mu$m slit and impinge on the second knife edge scanner we can determine the size of the beam $\Delta x_{MOC}$ behind the MOC. This fraction is found to be 20%, giving: $\Delta x_{MOC} = 0.28$ mm FWHM.

Table III: Atomic beam flux through the 1 mm orifice in the Zeeman mirror and on the 2D-detector for several combinations of operating beam sections. S: source, C: collimator and Z: Zeeman slower.

| Operating section | $\dot{N}$ through 1 mm orifice (He* s$^{-1}$) | $\dot{N}$ on 2D-detector (He* s$^{-1}$) |
|---|---|---|
| S | $2 \times 10^7$ *) | < 1 *) |
| S+C | $7.5 \times 10^8$ *) | $2.0 \times 10^2$ *) |
| S+C+MOC | $1.5 \times 10^9$ *) | < 1 *) |
| S+C+MOL+MOC | $7.5 \times 10^8$ *) | < 1 *) |
| S+C+Z | $9 \times 10^7$ **) | $1.0 \times 10^2$ *) |
| S+C+Z+MOC | $2.0 \times 10^8$ | $0.1 \times 10^2$ |
| S+C+Z+MOL+MOC | $5.0 \times 10^9$ | $2.5 \times 10^2$ |

*) thermal atoms.

**) we estimate: $2 \times 10^7$ s$^{-1}$ slow and $7 \times 10^7$ s$^{-1}$ thermal atoms.

Turning off the MOL decreases the flux of the compressed beam by a factor 25, resulting in: $\dot{N} = 2.0 \times 10^8$ s$^{-1}$. Thus, the MOL increases the effective capture radius of the MOC by a factor $\sqrt{25} = 5$.

Table III shows the beam flux that passes the 1 mm orifice in the Zeeman mirror for several combinations of laser cooling sections. It also shows the observed count rates on the 2D-detector, i.e., the number of atoms per second that pass the two final collimating apertures. Note that the MOL/MOC-combination is aligned in such a way that only slow atoms can reach the 2D-detector, while thermal atoms are blocked by the collimating apertures.

The decrease in beam flux after passing the collimating apertures allows us to determine $\sigma v_\perp$. For the collimated thermal beam we find: $\sigma v_\perp = 0.76$ ms$^{-1}$ ($= 2.7 v_\text{D}$), which is close to the 0.83 ms$^{-1}$ found with the two wire scanners. For the compressed slow beam we find: $\sigma v_\perp = 1.10$ ms$^{-1}$ ($= 3.9 v_\text{D}$). The observed flux of slow atoms behind the collimating apertures, $\dot{N} = 250$ s$^{-1}$, is a factor of 2 below the simulated value of section 3.2.

## 12   Concluding remarks

We have produced a narrow ($d_\text{beam} = 25$ $\mu$m), ultra-collimated ($\sigma v_\perp < 0.1 v_\text{R} = 9 \times 10^{-3}$ ms$^{-1}$), slow ($v_\parallel = 247$ ms$^{-1}$) and monochromatic ($\sigma v_\parallel / v_\parallel = 1.5 \times 10^{-2}$) beam of metastable helium atoms in the $\{2s\}^3S_1$ state. With a flux of 250 He* s$^{-1}$ the beam can be used in any experiment (e.g. atom optics or quantum optics) where a high-resolution study of the transverse momentum change of individual atoms is required.

In chapter 3 we will see that, with proper magnetic guiding and aligning techniques, the high-quality atomic beam is automatically spin-polarized in either the $|m_g = -1\rangle$ or $|m_g = 0\rangle$ magnetic substate. This extra feature, basically "free of charge", can be used to produce an effective two-level atom, when interacting with 1083 nm radiation. Thus, with the beam setup, we not only completely control the external (motional) state of the atom but also the internal (electronic) state.

## References

[1] J. Reichel, F. Bardou, M.B. Dahan, E. Peik, S. Rand, C. Salomon, and C. Cohen-Tannoudji, Phys. Rev. Lett. **75**, 4575 (1995).

[2] H. Hess, Bull. Am. Phys. Soc. **30**, 854 (1985).

[3] M.H. Anderson *et al.*, Science **269**, 198 (1995); K.B. Davis *et al.*, Phys. Rev. Lett. **75**, 3969 (1995); C.C. Bradley *et al.*, Phys. Rev. Lett. **75**, 1687 (1995); D.G. Fried *et al.*, Phys. Rev. Lett. **81**, 3811 (1998).

[4] D.J. Wineland and H. Dehmelt, Bull. Am. Phys. Soc. **20**, 637 (1975).

[5] T.W. Hänsch and A.L. Schawlow, Opt. Comm. **13**, 68 (1975).

[6] S. Chu, L. Hollberg, J.E. Bjorkholm, A. Cable, and A. Ashkin, Phys. Rev. Lett. **55**, 48 (1985).

[7] K. Gibble and S. Chu, Phys. Rev. Lett. **70**, 1771 (1993).

[8] See the special issue on atom optics and interferometry in Appl. Phys. B **54** (1992).

[9] See the special issue on laser cooling and trapping of atoms in J. Opt. Soc. Am. B **6** (1989).

[10] P.D. Lett, W.D. Phillips, S.L. Rolston, C.E. Tanner, R.N. Watts, and C.I. Westbrook, J. Opt. Soc. Am. B **6**, 2084 (1989).

[11] M.D. Hoogerland, J.P.J. Driessen, E.J.D. Vredenbregt, H.J.L. Megens, M.P. Schuwer, H.C.W. Beijerinck, and K.A.H. van Leeuwen, Appl. Phys. B **62**, 323 (1996).

[12] E. Raab, M. Prentiss, A. Cable, S. Chu, and D.E. Pritchard, Phys. Rev. Lett. **59**, 2631 (1987).

[13] J. Nellessen, J. Werner, W. Ertmer, Opt. Comm. **78**, 300 (1990).

[14] J.V. Prodan, W.D. Phillips, and H. Metcalf, Phys. Rev. Lett. **49**, 1149 (1982).

[15] P. Lett, R. Watts, C. Westbrook, W.D. Phillips, P. Gould, and H. Metcalf, Phys. Rev. Lett. **61**, 169 (1988).

[16] J. Dalibard and C. Cohen-Tannoudji, J. Opt. Soc. Am. B **6**, 2023 (1989).

[17] M.D. Hoogerland, H.C.W. Beijerinck, K.A.H. van Leeuwen, P. van der Straten, and H.J. Metcalf, Europhys. Lett. **19**, 669 (1992).

[18] B. Sheehy, S-Q. Shang, P. van der Straten, and H.J. Metcalf, Phys. Rev. Lett. **64**, 858 (1990).

[19] A. Aspect, E. Arimondo, R. Kaiser, N. Vansteenkiste, and C. Cohen-Tannoudji, Phys. Rev. Lett. **61**, 826 (1988).

[20] M. Kasevich and S. Chu, Phys. Rev. Lett. **69**, 1741 (1992).

[21] R.M.S. Knops, *Quantum optics with a cold helium beam*, Ph.D. thesis, Eindhoven University of Technology (1998).

[22] R.M.S. Knops, A.E.A. Koolen, H.C.W. Beijerinck, and K.A.H. van Leeuwen, Laser Physics **9**, 286 (1999).

[23] J.S. Major Jr. and D.F. Welch, Electr. Lett. **29**, 2121 (1993).

[24] H.C. Mastwijk, *Cold collisions of metastable helium atoms*, Ph.D. thesis, Utrecht University (1997).

[25] W. Demtröder, *Laser spectroscopy: basic concepts and instrumentation*, second enlarged edition (Springer, 1996).

[26] We gratefully acknowledge the group of Prof.dr. W. Hogervorst at the Vrije Universiteit of Amsterdam for filling the gas cells.

[27] H. Hotop, *Atomic, molecular and optical physics: atoms and molecules* **29B**, p. 191, eds. F.B. Dunning and R.G. Hulet (Academic Press, New York, 1996).

[28] W.J.M. Rooijakkers, *Laser cooling and trapping of metastable helium atoms*, Ph.D. thesis, Vrije Universiteit of Amsterdam (1997).

[29] H.C.W. Beijerinck, *Molecular beam studies with a time-of-flight machine*, Ph.D. thesis, Eindhoven University of Technnology (1975).

[30] J. Nellessen, J.H. Müller, K. Sengstock, and W. Ertmer, J. Opt. Soc. Am. B **6**, 2149 (1989).

[31] W. Rooijakkers, W. Hogervorst, W. Vassen, Opt. Comm. **123**, 321 (1996).

[32] D. Sesko, C.G. Fan, and C.E. Wieman, J. Opt. Soc. Am. B **5**, 1225 (1988).

[33] C. Salomon and J. Dalibard, C.R. Acad. Sci. Paris **306II**, 1319 (1988).

[34] A. Browaeys (private communication).

# Chapter 3

# Measuring atomic beam properties with a 2D-detector

## 1  Introduction

In chapter 2 we produced a narrow, ultra-collimated, slow and monochromatic beam of metastable helium atoms in the ${2s}^3S_1$ state. There, we used a two-dimensional position-sensitive detector solely to measure the atomic beam flux. We can, however, use the position information of the 2D-detector to further characterize and improve the quality of the atomic beam.  Dipole forces in a light field or even the pull of gravity changes the motional state of an atom in a subtle way, which can be easily observed on the detector.  Not only the external (motional) state of the atoms can be analyzed, but also the internal (electronic) state can be studied.  An inhomogeneous magnetic field can be used to project the magnetic substate, in which an atom resides, onto the motional state.

## 2  Two-dimensional detection of the atomic beam

For the experiments described in this thesis we need a two-dimensional position-sensitive single-atom detector with a high detection efficiency for metastable atoms, and preferably zero detection efficiency for ground state atoms. The spatial resolution of the detector, translated into transverse momentum, should not exceed the transverse momentum spread of the atomic beam. In our setup the 2D-detector is placed 2.05 m behind the interaction region, as shown in Fig. 3.1.

### 2.1  MCP-detector

Figure 3.2 shows a schematic view of the position-sensitive detector. It consists of a Z-stack of microchannel plates (MCP) together with a resistive anode.  A voltage of 3.2 kV is applied across the Z-stack. Each microchannel, 15 $\mu$m in diameter, acts as a small electron-multiplier.  The channels are positioned under an angle of 15°

Apertures     Interaction     2D-detector
region



2.00 m                    2.05 m
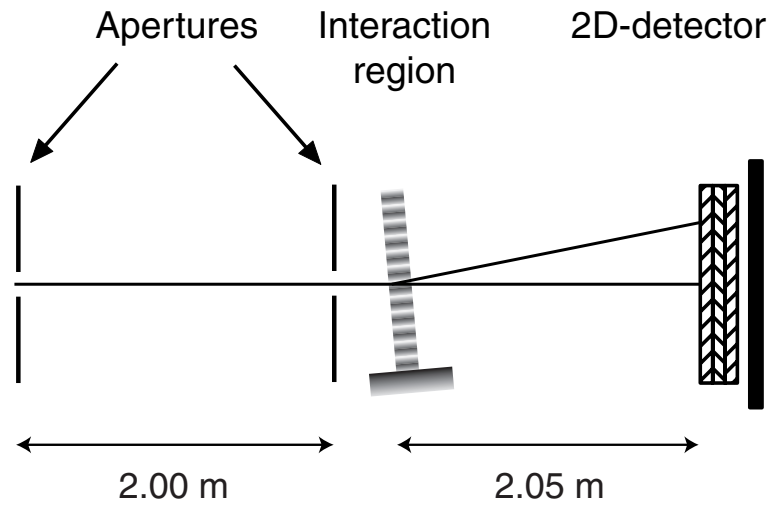
Figure 3.1: Last part of the atomic beam setup. The two apertures (60 $\mu$m and 25 $\mu$m in diameter) perform the final transverse beam collimation. Then, the atoms interact with a light field in the interaction region, after which they travel to the 2D-detector.

MCP's



Anode

Atom

Electrons

10 M$\Omega$   20 M$\Omega$  10 M$\Omega$

3.2 kV
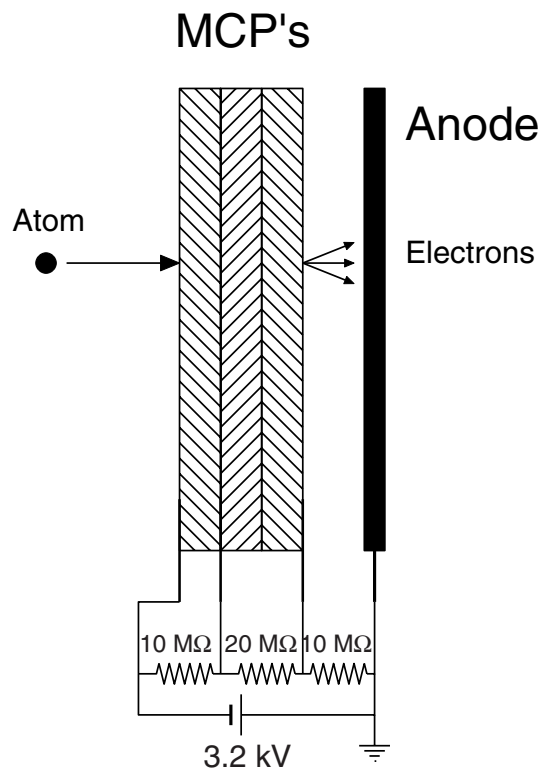
Figure 3.2: Schematic view of the position-sensitive detector, including MCP's and resistive anode.
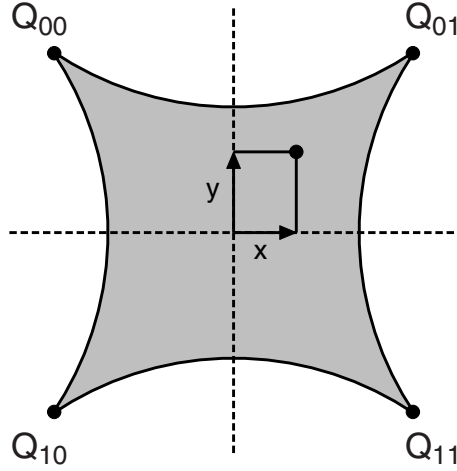
Figure 3.3: Front view of the resistive anode. The branching of the charge cloud towards the four corners is measured. This allows one to derive the position of impact of the atom in two dimensions.

to increase detection efficiency and spatial resolution. A metastable helium atom, impinging on the front surface of the detector, releases an electron from the surface with an efficiency close to unity.

The Z-stack provides an average gain of $4 \times 10^6$. The electron cloud produced by the Z-stack strikes the resistive anode. The electric charge pulse flows through the uniform resistive layer of the anode. It is divided and collected by four electrodes connected to the corners, as shown in Fig. 3.3. From the amount of charge that flows to each of the four electrodes the position of the electron cloud can be calculated:

$$x = \frac{L}{2}\frac{(Q_{01} + Q_{11}) - (Q_{00} + Q_{10})}{Q_{00} + Q_{01} + Q_{10} + Q_{11}}, \tag{3.1}$$

$$y = \frac{L}{2}\frac{(Q_{00} + Q_{01}) - (Q_{10} + Q_{11})}{Q_{00} + Q_{01} + Q_{10} + Q_{11}}, \tag{3.2}$$

where $Q_{ij}$ denote the collected charges and $L$ denotes a length parameter, which was measured to be $L = 34.4$ mm [1]. The pincushion shape of the anode is necessary to obtain the linear relations in Eqs. 3.1 and 3.2. The MCP's used in the Z-stack have a viable area of 25 mm in diameter (equal to $33v_R$ of transverse velocity at $v_\parallel = 247 \, \mathrm{ms}^{-1}$).

## 2.2  Electronics

In order to measure the charges $Q_{ij}$, we use the electronics setup schematically shown in Fig. 3.4. The electric currents at the four corners are amplified in four home-made DC-coupled charge-sensitive amplifiers. Next, the signals are amplified by four spectroscopic shaping amplifiers (EG&G Ortec 855). The amplified signals are processed by four home-made peak detectors that retain the peak height for a few microseconds and produce a trigger signal. An additional discriminator measures the sum of the four peak heights and produces a fifth trigger signal if the sum
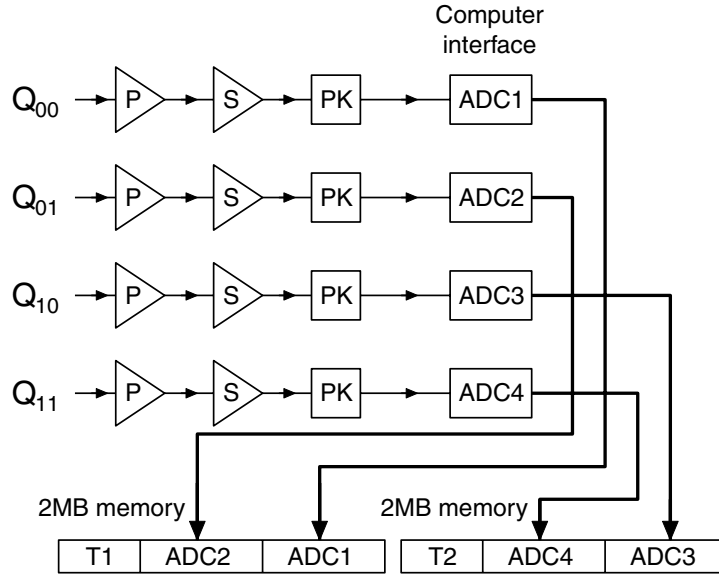
Figure 3.4: Overview of the electronics used to measure the charge pulse at the four corners of the resistive anode. P: charge-sensitive pre-amplifier, S: spectroscopic amplifier, PK: peak height detector. The results of the four AD conversions are stored in the memory of the interface, together with the content of the counters T1 and T2. Additional trigger and the logical circuitry are not shown.

exceeds a preset minimum value. A logical device checks whether all five trigger signals are present and, if so, sends a final trigger to the computer interface. There an AD conversion is performed on the four output signals from the peak detectors. We use two interfaces, which are synchronized, to perform in total four AD conversions simultaneously. Each interface consists of two synchronized 12-bit ADCs, an 8-bit counter, and a 2 MB memory. In the memory, the results of subsequent AD conversions together with the value of the counter are stored. The counter can be used to perform time-resolved measurements. The dedicated computer interfaces are designed and built by the Technical Laboratory Automation group of the Physics Department. The detector electronics can handle a maximum of $30 \times 10^3$ events per second.

## 2.3   Resolution

The inset in Fig. 3.5(a) shows the density image, measured on the 2D-detector, of the thermal atomic beam (only source and collimator operational). Figure 3.5(a) shows the 1D Gaussian line profile through the middle of the peak, measured along the horizontal $x$-dimension: the peak has a 67 $\mu$m rms width. We assume that the width of the thermal beam on the 2D-detector is purely geometrically determined by the two collimating apertures (60 $\mu$m and 25 $\mu$m in diameter, separated by 2 m). Deconvoluting the measured 1D-profile with the trapezium-shaped atomic beam profile, imposed by the two collimating apertures, gives an rms detection resolution of 60 $\mu$m. For 247 ms$^{-1}$ atoms this is equivalent to an rms velocity spread of $0.08v_{\mathrm{R}}$.

Figure 3.5: 1D line profile along the $x$-dimension through the peak on the 2D-detector (solid circles) together with a Gaussian fit (solid line) for a thermal beam (a) and a slow beam (b). The inset shows the corresponding detector image of area $2.5 \times 2.5$ mm$^2$.

The inset in Fig. 3.5(b) shows the density image, measured on the 2D-detector, of the slow atomic beam (source, collimator, Zeeman slower, MOL, and MOC operational). Figure 3.5(b) shows the 1D Gaussian line profile through the middle of the peak, measured along the horizontal $x$-dimension: the peak has a 98 $\mu$m rms width, which corresponds to an rms minimum feature size on the 2D-detector of $0.13v_R$. The increase in width is caused by an increase in beam divergence, which is attributed to a small residual Stern-Gerlach effect [2] in the second collimating aperture, made from copper. The effect is best observed with a slow atomic beam. We will return to this effect in section 4.3. The minimum feature size on the 2D-detector contains both the finite detection resolution and the transverse velocity spread of the slow atomic beam. We find for the rms transverse velocity spread of the slow atomic beam: $\sigma v_\perp = 0.10v_R$.

# 3   Longitudinal atomic velocity imaging

The atomic beam can be deflected by adding transverse momentum to it. The resulting displacement, observed on the 2D-detector, does not only depend on the atomic transverse velocity but also on the longitudinal velocity. This allows one to map the longitudinal velocity distribution of the atomic beam onto the 2D-detector.

## 3.1   Vertical mapping by gravity

All atoms in the atomic beam feel the pull of gravity, which causes them to be accelerated downwards. It takes gravity 10 ms to accelerate an atom to the helium
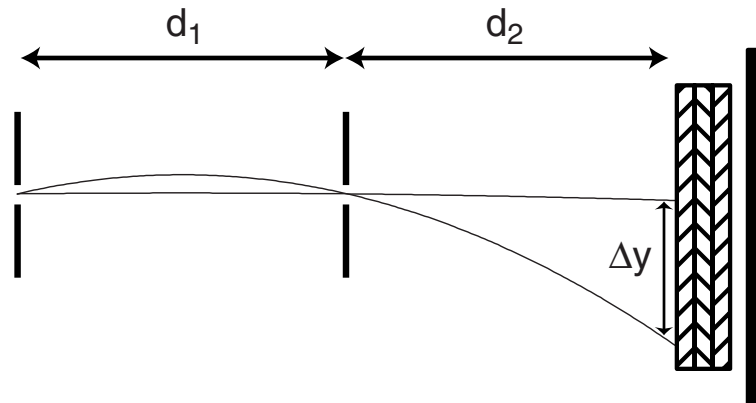
Figure 3.6: Parabolic trajectories, due to gravity, of a thermal and a slow atom towards the 2D-detector. The slow atom hits the detector at a lower $y$-position than the thermal atom.
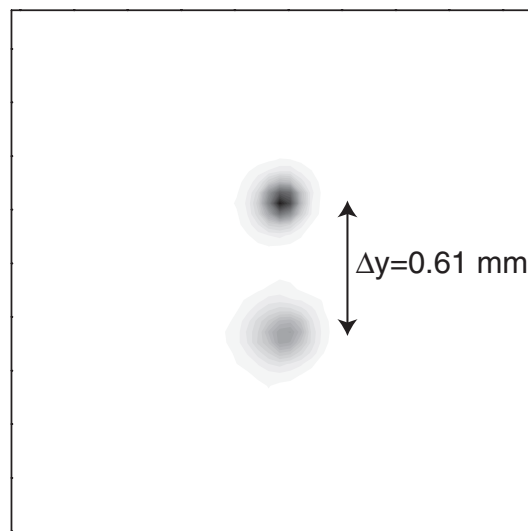


Figure 3.7: Superposition of the detector images of a thermal and a slow atomic beam. Both beams are fully spatially separated on the 2D-detector. The slow atomic beam clearly hits the 2D-detector at a lower $y$-position. The size of the detector image is $2.5 \times 2.5$ mm$^2$.

recoil velocity $v_R = 0.092$ ms$^{-1}$. In our setup, it takes a thermal atom around 3.5 ms to travel from the first collimating aperture to the 2D-detector, while a slow atoms needs 16 ms to accomplish this. Since both atoms have to pass the two narrow collimating apertures, they will travel along different parabolic paths and impinge on the 2D-detector at different $y$-positions (see Fig. 3.6). Thus, gravity maps the velocity distribution of the atomic beam onto the vertical dimension of the 2D-detector.

The separation on the 2D-detector between a thermal and a slow atom, $\Delta y$, can be calculated to be

$$\Delta y = \frac{g(d_1 + d_2)d_2(v_{\parallel,t}^2 - v_{\parallel,s}^2)}{2v_{\parallel,t}^2 v_{\parallel,s}^2}, \tag{3.3}$$

with $d_1$ the distance between the two collimating apertures, $d_2$ the distance between the second collimating aperture and the 2D-detector, $v_{\parallel,t}$ the longitudinal velocity of the thermal atom, $v_{\parallel,s}$ the longitudinal velocity of the slow atom and $g$ the gravitational acceleration.

Figure 3.7 is a superposition of the detector images of the thermal and the slow beam (Fig. 3.5(a) and Fig. 3.5(b)). We find: $\Delta y = 0.61$ mm. With $d_1 = 2.00$ m, $d_2 = 2.07$ m, $v_{\parallel,t} = 1175$ ms$^{-1}$ and $g = 9.81$ ms$^{-2}$, this corresponds to: $v_{\parallel,s} = 252$ ms$^{-1}$. Gravity does not transfer enough transverse momentum to the atomic beam to accurately measure the longitudinal velocity spread.

## 3.2   Horizontal mapping by atomic Bragg scattering

In chapter 5 we will let the slow atomic beam interact with a standing light field in the context of atomic Bragg scattering [3]. Within a few microseconds each atom obtains $2N\hbar k$ of transverse momentum, where $N$ is an integer. Here, we shall specifically focus on 5$^{th}$ order Bragg scattering, where $N = 5$. The standing light field is oriented along the horizontal $x$-dimension. Thus, the atoms will be scattered on the 2D-detector from $x_0 = 0$ to

$$x_5 = \frac{v_\perp d}{v_\parallel} = \frac{10v_R d}{v_\parallel}, \tag{3.4}$$

with $v_R$ the helium recoil velocity and $d = 2.05$ m the distance between the standing light field and the 2D-detector.

Figure 3.8 shows the 1D Gaussian line profile through the middle of the diffracted peak, measured along the horizontal $x$-dimension: the peak is centered around $x_5 = 7.60$ mm and has an rms width $\sigma x_5 = 148$ $\mu$m. Thus, deflection by a single photon momentum $\hbar k$ corresponds to a 0.76 mm displacement on the 2D-detector. The longitudinal velocity spread can be calculated to be

$$\frac{\sigma v_\parallel}{v_\parallel} = \frac{\sqrt{(\sigma x_5)^2 - (\sigma x_0)^2}}{x_5}, \tag{3.5}$$

with $\sigma x_0$ the width of the undeflected beam. With $\sigma x_0 = 98$ $\mu$m, as shown in Fig. 3.5(b), we find: $v_\parallel = 247$ ms$^{-1}$ and $\sigma v_\parallel / v_\parallel = 1.5 \times 10^{-2}$.
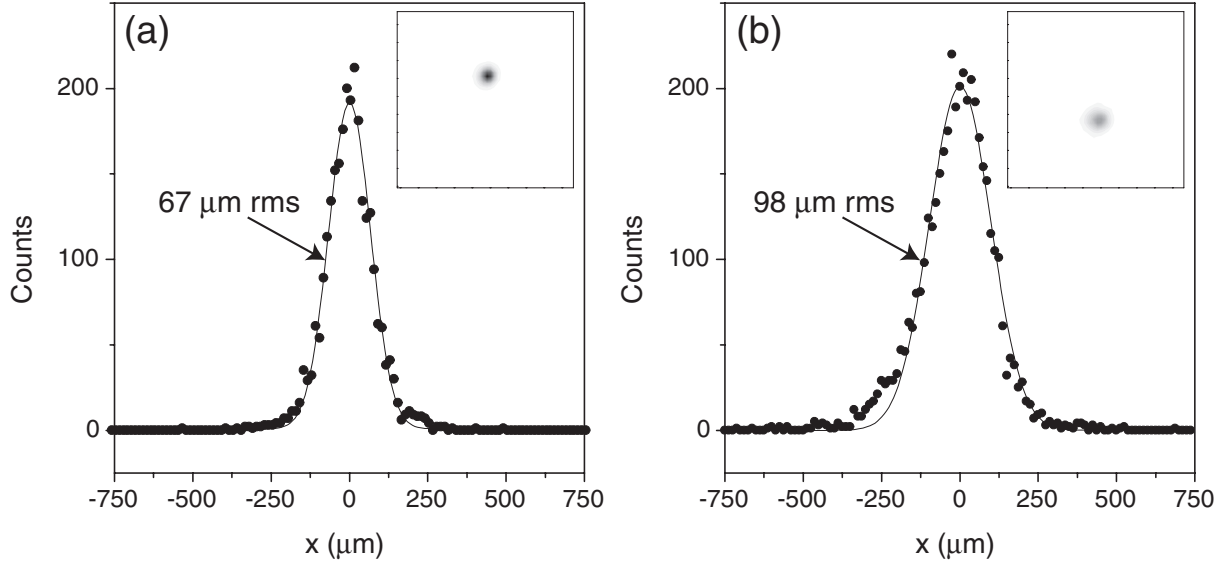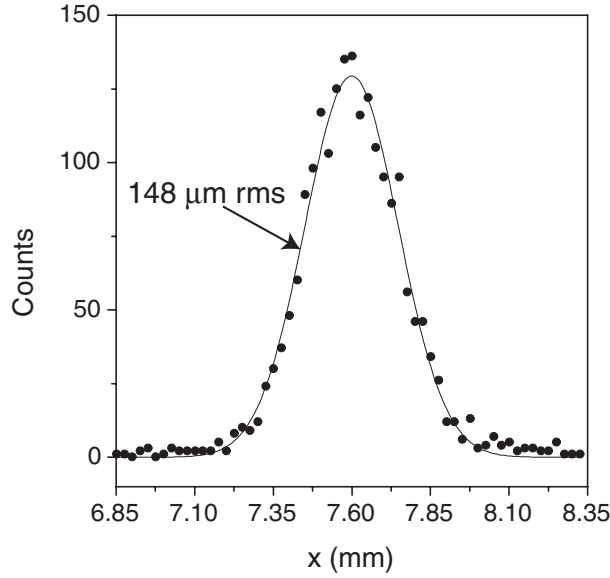
**Figure 3.8:** 1D line profile along the $x$-dimension through the peak on the 2D-detector (solid circles) together with a Gaussian fit (solid line) for a fifth order Bragg diffracted slow atomic beam. The peak has broadened due to the longitudinal velocity spread of the beam.

# 4   Magnetic substate imaging by Stern-Gerlach type of beam deflection

The interaction strength between a helium atom in the $\{2s\}^3S_1$ state and a resonant light field, with a well-defined polarization, strongly depends on the ground state magnetic quantum number $m_g$ $(= -1, 0$ or $+1)$ of the atom. Most of the experiments, described in this thesis, require a well-defined interaction strength for each individual atom that passes through the light field. Thus, it is important to know how the atoms are distributed over the three magnetic substates when they enter the light field.

## 4.1   Stern-Gerlach force

Using an inhomogeneous magnetic field we can spatially separate atoms with a different magnetic quantum number on the 2D-detector. Placing an atom with a magnetic dipole moment $\vec{\mu}$ in an external magnetic field $\vec{B}$ will change its internal energy by $-\vec{\mu} \cdot \vec{B}$. If the atom is moving and it experiences only slow variations in the external field, then the projection of the atom's magnetic dipole moment onto the external magnetic field, $m_g$, will remain constant. During this so-called adiabatic motion [4] the internal magnetic energy of the atom acts as a position-dependent potential. The resulting Stern-Gerlach force [2, 5] is proportional to the gradient of the magnetic field and depends on the magnetic quantum number $m_g$:

$$\vec{F} = \vec{\nabla}(\vec{\mu} \cdot \vec{B}) = -\mu_{\mathrm{B}} g_g m_g \vec{\nabla}|B|, \qquad (3.6)$$
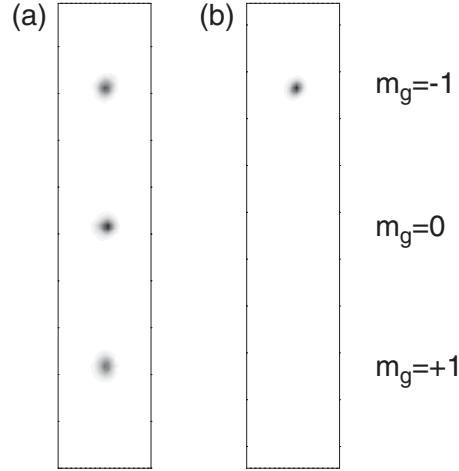
Figure 3.9: Substate dependent deflection by the Stern-Gerlach force of an unpolarized beam (a) and a spin-polarized ($m_g = -1$) beam (b) of metastable helium atoms. The size of each detector image is $2 \times 10$ mm$^2$.

where $\mu_B$ is the Bohr magneton and $g_g$ (= 2 in our case) is the Landé factor.

To test this method we placed a barium ferrite magnet ($40 \times 35 \times 10$ mm$^3$, 0.4 T magnetization) outside the vacuum tube at a distance of 28 mm from the atomic beam axis. The permanent magnet is positioned halfway between the interaction region and the 2D-detector (see Fig. 3.1). With the slow atomic beam we obtain the detector image of Fig. 3.9(a). Thus, just before entering the inhomogeneous magnetic field, the atoms in the beam are approximately equally distributed over all three magnetic substates.

Atoms with $m_g = 0$ are not deflected by the permanent magnet. Placing the magnet halfway between the two final collimating apertures, results in a very low count rate on the 2D-detector. Evidently, most of the atoms are deflected and are consequently blocked by the second collimating aperture. Thus, very few $m_g = 0$ atoms are present halfway between the two collimating apertures. Further analysis shows that the atomic beam is largely spin-polarized up to the second collimating aperture. Evidently, the atoms pass a field free region at this point and get depolarized. By adding a (homogeneous) magnetic guiding field of a few Gauss at this position, the beam retains its spin-polarization. Figure 3.9(b) shows that with the extra guiding field the atomic beam is spin-polarized in the "high-field seeking" $m_g = -1$ substate. The degree of polarization is found to be 92%, and the remaining 8% is polarized in $m_g = 0$. The beam flux is 250 He* s$^{-1}$.

By slightly realigning the light field axis of the MOC, the magnetic quadrupole field axis of the MOC, and the collimating apertures, we are able to produce an atomic beam that is completely spin-polarized in the $m_g = 0$ substate. The beam flux, however, is only 50 He* s$^{-1}$. No "low-field seeking" $m_g = +1$ atoms were ever found with this realigning technique. Thus, it seems that the MOC performs a magnetic substate separation, by steering the $m_g = -1$ atoms into a different direction than the $m_g = 0$ atoms. With the two collimating apertures we can select a single species while blocking the other and hence produce a spin-polarized atomic beam.

## 4.2  Magnetic substate separation behind the MOC

The presence of separate spin-polarized beams of $m_g = -1$ and $m_g = 0$ atoms behind the MOC can be understood by examining the forces that are exerted on the atoms while traversing its light- and magnetic field. Optical pumping processes make sure that no $m_g = +1$ atoms leave the MOC.

In the MOC, where both a light field and an increasing magnetic field gradient are present, the laser cooling force is by far dominant: the atoms are pulled towards the quadrupole axis and compressed into a narrow beam. The magnetic field gradient reaches its maximum at the position of the permanent magnets, as indicated in Fig. 3.10. Whereas the light field ends abruptly, the magnetic field gradient can not be turned off instantly. Thus, behind the MOC, the atoms will experience a gradually decreasing Stern-Gerlach force.

Equation 3.6 shows that the Stern-Gerlach force depends on the magnetic substate $m_g$, which is defined with respect to the local magnetic field direction. The optical pumping processes in the MOC polarize the atoms primarily in the "high-field seeking" $m_g = -1$ substate. This can be understood from Fig. 3.11. It shows a schematic representation of the MOC, that includes both the laser beams and the (on-axis) magnetic fields in the two transverse dimensions. An atom with a small transverse velocity will primarily feel the position-dependence of the laser cooling force, which drives the atom towards the magnetic quadrupole axis. This means that the atom absorbs most photons per unit of time from the laser beam that pushes the atom towards the quadrupole axis. The associated optical pumping processes orients the magnetic dipole moment $\vec{\mu}$ along the component of the local magnetic field in the corresponding dimension. Thus, most of the atoms will be polarized in the "high-field seeking" substate, which is the $m_g = -1$ substate with respect to the local magnetic field direction. Some atoms are left in $m_g = 0$ and hardly any atoms exit in the "low-field seeking" $m_g = +1$ state.

Consider a helium atom that leaves the light field of the MOC at the transverse position $\vec{r} = (x, y)$ (the magnetic quadrupole axis is positioned at $\vec{r} = \vec{0}$) in magnetic substate $m_g$ with respect to the local magnetic field vector $\vec{B}(\vec{r})$. The atom has no initial transverse velocity. The magnetic quadrupole field, $\vec{B}(\vec{r}) = [a(z)x, -a(z)y]$, of the MOC will accelerate the atom to

$$\vec{v}_{\perp,\mathrm{SG}} = -\frac{\mu_{\mathrm{B}} g_g m_g}{M v_{\parallel}} \frac{\vec{r}}{|\vec{r}|} \int |a(z)| \mathrm{d}z, \tag{3.7}$$

with $M$ the atomic mass, $v_{\parallel}$ the forward velocity of the atom and $a(z)$ the transverse magnetic field gradient at longitudinal position $z$. Thus, the motion of the $m_g = 0$ atoms is undisturbed, while the $m_g = -1$ atoms experience a radial Stern-Gerlach force that points away from the magnetic quadrupole axis. Thus, in transverse velocity space the $m_g = -1$ atoms end up on a circle with radius $v_{\perp,\mathrm{SG}} = |\vec{v}_{\perp,\mathrm{SG}}|$. From the measured magnetic field gradient profile of Fig. 3.10 we estimate that $v_{\perp,\mathrm{SG}} = 0.6 \text{ ms}^{-1}$ for the $m_g = -1$ atoms. Presumably, this effect contributes to the measured rms transverse velocity spread of $1.10 \text{ ms}^{-1}$ behind the MOC (see chapter 2).
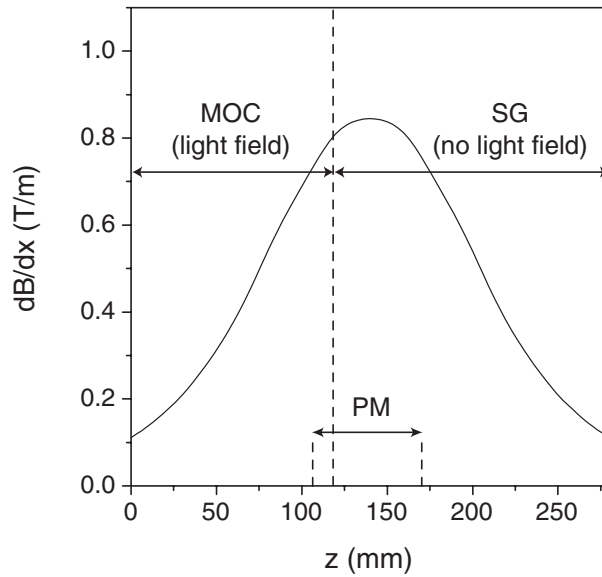
Figure 3.10: In the MOC, the laser cooling force is by far dominant and the influence of the Stern-Gerlach force can be neglected. Behind the MOC, the light field disappears while the magnetic field gradient remains. This will cause substate-dependent Stern-Gerlach (SG) deflection of the atomic beam. The amount of deflection is proportional to the area under the gradient curve in this region. PM: position of the permanent magnets that create the quadrupole field.
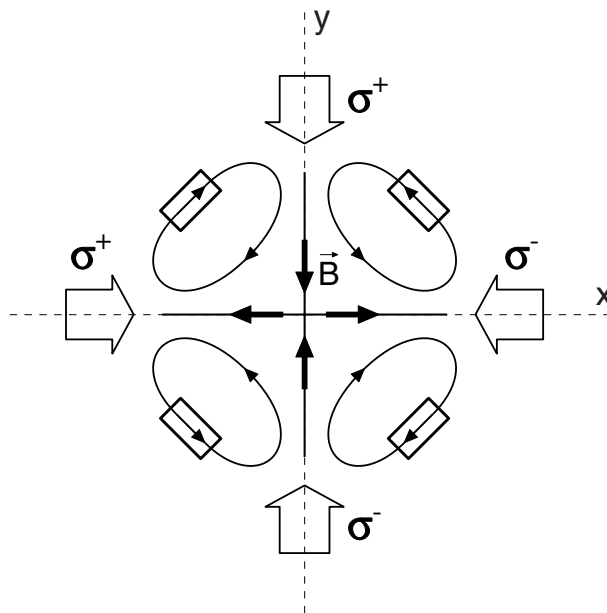


Figure 3.11: The light fields in the "trap-configuration" of the MOC try to polarize the metastable helium atoms in the "high-field seeking" $m_g = -1$ substate.
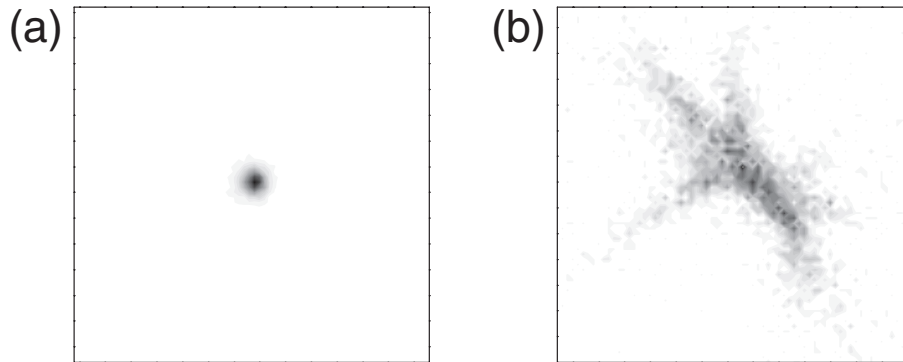
Figure 3.12: Transverse heating of the slow atomic beam while passing the second collimating aperture. For a copper aperture (a) the heating effect is relatively small, while a stainless steel aperture (b) increases the beam divergence to above the recoil limit. The size of each detector image is $3.5 \times 3.5 \text{ mm}^2$.

Only atoms within a small area of transverse phase-space can pass the two colli-mating apertures. The Stern-Gerlach effect sufficiently separates the $m_g = 0$ atoms from the $m_g = -1$ atoms in phase-space, such that one can select only a single species at the same time.

## 4.3 Stern-Gerlach dispersion introduced by a stainless steel aperture

The second collimating aperture (25 $\mu$m diameter) is made from copper. Previously, we used a stainless steel aperture (30 $\mu$m diameter). Figure 3.12 shows the 2D-detector images of the slow atomic beam for both situations. The slow beam shows significant anisotropic "heating" when passing the stainless steel aperture. Magnetic substate analysis shows that both beams are spin-polarized in the $m_g = -1$ substate. When using the stainless steel aperture, no additional guiding field is required to get spin-polarization. We believe that a small residual magnetization of the stainless steel causes large and irregular magnetic field gradients over the small area of the aperture. The resulting strong Stern-Gerlach force deflects the $m_g = -1$ atoms in several directions, since it is highly position-dependent. Copper shows a much smaller residual magnetization, resulting in a much smaller dispersion.

A thermal atomic beam and a slow beam of $m_g = 0$ atoms produce peaks of identical widths on the 2D-detector, independent of whether a stainless steel or a copper aperture is used. Any Stern-Gerlach dispersion added to the thermal atomic beam evidently stays well within the 2D-detector resolution.

Two orthogonal knife edge scanners, each equipped with a 60 $\mu$m wide slit, serve as the first collimating aperture. Each scanners consists of a glass plate coated with a conducting ITO-layer. The Stern-Gerlach dispersion introduced by these slits should be negligible.

Schmiedmayer *et al.* [6] observe that a spin-polarized beam of sodium atoms is significantly depolarized when passing a stainless steel slit (10 $\mu$m wide) at thermal

velocities (1000 ms$^{-1}$). The loss of polarization is attributed to nonadiabatic transitions, also known as "Majorana flops", due to the rapid transit of the atoms through the collimating slit. Up to thermal velocities we observe adiabatic passage of the metastable helium atoms through the stainless steel aperture. At low velocities, however, the beam divergence is dramatically increased due to the Stern-Gerlach dispersion.

## 5  Concluding remarks

With the aid of the 2D-detector we now have complete control over both the electronic and motional properties of the atomic beam. High quality ($d_{beam} = 25$ $\mu$m, $\sigma v_\perp = 0.1 v_R = 9 \times 10^{-3}$ ms$^{-1}$, $v_\parallel = 247$ ms$^{-1}$ and $\sigma v_\parallel / v_\parallel = 1.5 \times 10^{-2}$) beams of either $m_g = -1$ (250 He* s$^{-1}$) or $m_g = 0$ (50 He* s$^{-1}$) atoms can be obtained. In the rest of this thesis, we will use the $m_g = -1$ beam together with the 2D-detector to study both the radiation- and the dipole force on atoms with sub-recoil precision.

## References

[1] T.E.F.M. Standaert, internal report, Eindhoven University of Technology (1995).

[2] W. Gerlach and O. Stern, Z. Phys. **8**, 110 (1922).

[3] P.J. Martin, B.G. Oldaker, A.H. Miklich, and D.E. Pritchard, Phys. Rev. Lett. **60**, 515 (1988).

[4] L.I. Schiff, *Quantum mechanics*, third edition (McGraw-Hill, New York, 1968), p. 289.

[5] W.J. Rowlands, D.C. Lau, G.I. Opat, A.I. Sidorov, R.J. McLean, P. Hannaford, Opt. Comm. **126**, 55 (1996).

[6] J. Schmiedmayer *et al.*, *Atom interferometry*, p. 7, ed. P.R. Berman (Academic Press, New York, 1997).

# Chapter 4

# Angular distributions of spontaneous emission observed in atomic recoil

## 1 Introduction

The process of spontaneous emission plays an important role in most laser cooling mechanisms. Atoms are cooled by many consecutive absorption/spontaneous emission cycles, during which the atomic kinetic energy is gradually reduced. Although essential for laser cooling, the stochastic nature of spontaneous emission also introduces lower bounds to the temperatures that can be reached in the atomic samples. Well-known milestones are the Doppler temperature [1] and the recoil limit [2, 3]. Temperatures below the recoil limit can only be reached by turning off the spontaneous emission process for atoms that are already cold enough. This had led to the development of techniques such as velocity-selective coherent population trapping (VSCPT) [4] and stimulated Raman cooling [5].

Allowing spontaneous emission in systems with sub-recoil temperatures will not only lead to heating, but will also change the motional state of the atoms in an irreversible way. This can be particularly annoying in systems where the motional state of the atoms is carefully being prepared by coherent laser-atom interactions. The process of spontaneous emission can then be interpreted as a diffusion process in momentum space. The gradual influence of such a diffusion process on atomic diffraction was first studied by Gould *et al.* [6].

Few experiments deal with the influence of just a single spontaneously emitted photon [7]. This regime was first studied experimentally by Pfau *et al.* [8]. They diffracted and excited metastable helium atoms with a standing light wave. After interaction, the excited atoms decayed by a single spontaneously emitted photon. The resulting transverse momentum distribution was mapped on a one-dimensional detector. This way they were able to measure the loss of spatial coherence of the atomic de Broglie wave.

Using a Bose-Einstein condensate of sodium atoms, of which the momentum distribution could be displayed with an optical imaging technique, Kozuma *et al.* [9] were able to map an angular radiation distribution, produced by spontaneous emission, into a two-dimensional atomic pattern. This was done in the context of atomic
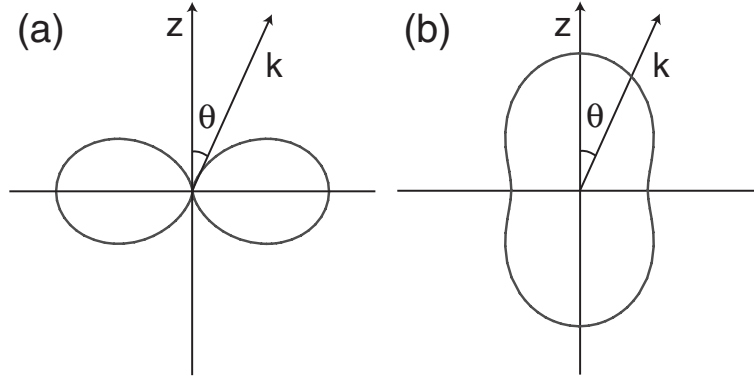
Figure 4.1: Polar representation of the radiation distribution functions $F_1^M(\theta)$ for (a) $M=0$ and (b) $M=\pm1$. The $z$-axis represents the quantization axis.

Bragg diffraction and no further effort was made to study these patterns in more detail.

The combination of a spin-polarized ($m_g = -1$) beam of metastable helium atoms in the $\{2s\}^3S_1$ state, the Stern-Gerlach force that deflects atoms according to their magnetic substate [10], and the use of a two-dimensional position-sensitive detector allows a more detailed investigation of these patterns. The shape of the patterns should depend on the polarization of the emitted photon. Two main types of emission patterns, associated with decay via either a $\pi$- or a $\sigma$-transition, can be identified. In this chapter we will show that both patterns can be independently measured. By carefully orienting the quantization axis $z$ of the atom, the symmetry properties of the atomic patterns can be resolved.

## 2   Angular distributions of spontaneous emission

Consider an atom undergoing spontaneous decay from an excited state $|J_e m_e\rangle$ to a ground state $|J_g m_g\rangle$ with respect to the quantization axis $z$. In general, this is an optical multipole ($2^J$) transition, described by the order $J$ and the change in magnetic quantum number $M = m_e - m_g$. The angular radiation distribution function $F_J^M$ for such a transition depends only on $J$ and $M$: it is independent of whether the transition produces magnetic or electric multipole radiation. For electric dipole transitions ($J = 1$ and $M = 0, \pm1$), which have by far the highest decay rates, the two possible normalized distribution functions in spherical coordinates are [11]

$$F_1^0(\theta) \;\;=\;\; \frac{3}{8\pi}\sin^2\theta, \tag{4.1}$$

$$F_1^{\pm1}(\theta) \;\;=\;\; \frac{3}{16\pi}\left(1 + \cos^2\theta\right), \tag{4.2}$$

in which $\theta$ is the angle between the quantization axis $z$ and the wavevector $\vec{k}$ of the emitted photon. There is no dependence on the azimuthal angle $\varphi$.

A polar representation of the distribution functions is given in Fig. 4.1. In the $M = 0$ case, the component of the angular momentum of the emitted photon along

the quantization axis is zero. The atom does not change its magnetic quantum number $m$: this is called a $\pi$-transition. If $M = \pm 1$, the component of the angular momentum of the emitted photon along the quantization axis is $\pm \hbar$. Now $m$ changes with $\mp 1$: this is called a $\sigma$-transition.

The polarization of the emitted photon can only be measured with respect to the wavevector $\vec{k}$, which is usually not oriented along the quantization axis $z$. Thus, the polarization of the emitted radiation can, in general, be anything between linear and circular, depending on the transition involved ($M = 0, \pm 1$) and the orientation of the wavevector $\vec{k}$ with respect to the quantization axis $z$.

A simple classical interpretation can be used to understand the angular radiation distributions for electric dipole transitions. In the case of a $\pi$-transition the atom can be seen as a linear dipole oscillator that oscillates along the quantization axis. Such an oscillator does not emit radiation in the direction of oscillation. Observing the linear oscillator from the side ($\theta = \pi/2$) reveals the full oscillation amplitude. Hence, the linear oscillator emits most of its radiation in this direction. For each angle of observation the emitted radiation is linearly polarized in the plane that includes both the quantization axis and the wavevector.

An atom undergoing a $\sigma$-transition can be seen as a rotor, that rotates in the plane perpendicular to the quantization axis. The rotor can be thought of as a superposition of two orthogonal linear dipole oscillators, that oscillate with a phase difference of $\pi/2$. When looking along the quantization axis both linear oscillators reveal their full oscillation amplitude. Thus, the maximum amount of radiation is emitted in this direction. Because of the $\pi/2$ phase difference this radiation is circularly polarized. Observation under $\theta = \pi/2$ reveals just a single linear oscillator, thus giving a factor of two less radiation. This radiation is linearly polarized in the plane perpendicular to the quantization axis. For all other angles $\theta$ the emitted radiation is elliptically polarized.

# 3   Imaging techniques

## 3.1   Optical detection

Observing the radiation distributions $F_1^M(\theta)$ can in principle be done using optical techniques. For this purpose, one should prepare an atomic sample that emits radiation from a fixed point in space. A photomultiplier is used to detect the radiation that is emitted in a certain direction. A magnetic field and/or the technique of optical pumping [12,13] can be used to orient the angular momentum and the quantization axis of the atomic sample with respect to the photomultiplier.

Take, e.g., an atomic sample excited on a $J = 0 \to J = 1$ transition. By using either linearly or circularly polarized light, the atom will only decay via a $\pi$- or a $\sigma$-transition, respectively. This allows one to measure the radiation distributions $F_1^0(\theta)$ and $F_1^{\pm 1}(\theta)$ separately, provided that the orientation of the quantization axis with respect to the photomultiplier can be freely changed.

Most of the experiments done with optical detection techniques were concerned
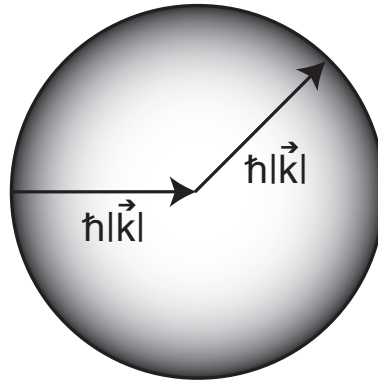
Figure 4.2: Profile on the 2D-detector of atoms undergoing a single absorption/spontaneous emission cycle.

with the properties of resonance fluorescence [14]. In early experiments [15–19] the polarization properties of the resonance fluorescence from large atomic samples were studied. Subsequent refining finally led to the observation of resonance fluorescence (showing sub-Poissonian photon-statistics) from a single ion stored in a rf trap [20]. All these experiments were done for a limited set of orientations of the quantization axis with respect to the photomultiplier.

## 3.2   Principle of recoil imaging

Instead of detecting each emitted photon, one can also study its effect on the motional state of the atom. Consider atoms, that have a well-defined momentum $\vec{p}$, interacting with a single running wave: absorption of a photon followed by spontaneous emission will change the atomic momentum $\vec{p}$ into $\vec{p} + \hbar\vec{k} - \hbar\vec{k}_r$, in which $\vec{k}$ is the wavevector of the running wave that excites the atom, and $\vec{k}_r$ is the wavevector of the spontaneously emitted photon. Although $|\vec{k}_r| = |\vec{k}|$, the direction of the spontaneously emitted photon can not be predicted but follows the angular radiation distribution functions given in Eqs. 4.1 and 4.2. Hence, after a single absorption/spontaneous emission cycle the atoms will be oriented on a sphere in momentum space. The center of the sphere is $\vec{p} + \hbar\vec{k}$ and the radius is $\hbar|\vec{k}|$. In a running wave no momentum can be transferred from the light field to the atom by absorption/stimulated emission cycles.

   In a beam experiment, the running wave is placed orthogonal to the atomic beam axis. The interaction can be made sufficiently weak, such that only a negligible fraction of the atoms spontaneously emit a photon more than once. The two recoils, obtained in the single absorption/spontaneous emission cycle, change the transverse momentum $\vec{p}_\perp$ of the atom. Before interaction: $\vec{p}_\perp = \vec{0}$. After the cycle: $\vec{p}_\perp = \hbar(\vec{k} - \vec{k}_{r,\perp})$, in which $\vec{k}_{r,\perp}$ is the transverse projection of $\vec{k}_r$. The 2D-detector is placed far behind the interaction region. With a short lifetime of the excited state the atoms will decay almost instantaneously. Thus, the transverse momentum distribution of the atomic beam, right behind the interaction region, is mapped onto a position distribution that is observed on the 2D-detector. Evidently, the atomic beam

has to be monochromatic, narrow, and sub-recoil collimated for this to work. Since $|\vec{k}_{r,\perp}| \leq |\vec{k}|$ the atoms that undergo spontaneous emission will produce a disc on the 2D-detector. The radius of the disc in momentum space is $\hbar|\vec{k}|$. This is depicted in Fig. 4.2.

The angular radiation distributions of Eqs. 4.1 and 4.2 are defined with respect to the quantization axis $z$. The exact distribution of the atoms over the disc in Fig. 4.2 will therefore depend on the orientation of the quantization axis with respect to the atomic beam axis. One is free to choose the orientation of the quantization axis, but two particular choices exploit the symmetry properties of Eqs. 4.1 and 4.2. By choosing the orientation of the quantization axis $z$ either parallel or perpendicular to the atomic beam axis, each point on the disc corresponds to two points on the sphere that have the same value of $F_1^M$. The corresponding discs should then reflect the symmetry properties of Eqs. 4.1 and 4.2. In general, the orientation of the quantization axis $z$ is chosen by applying a weak magnetic field $\vec{B}$ in the desired direction.

The next problem one faces, is to separate atoms that decayed via $M = 0$ from atoms that decayed via $M = \pm 1$. This is most easily done with an atomic beam, that is initially spin-polarized, and a Stern-Gerlach type of magnetic substate separation [10]. By carefully choosing both the direction of the wavevector $\vec{k}$ and the polarization of the laser light, the atoms can be excited into a single excited state $|J_e m_e\rangle$ with respect to the quantization axis $z$ defined by the magnetic field $\vec{B}$. By using Stern-Gerlach magnetic substate separation, as discussed in chapter 3, the different ground states $|J_g m_g\rangle$ are directed towards different detector positions. In general, this will produce $2J_g+1$ discs on the detector. The selection rules for electric dipole transitions allow that at most three of these discs are populated. Each disc will be a two-dimensional projection of $F_1^{m_e-m_g}$.

# 4   Experimental setup

In this experiment we use the atomic beam of metastable helium atoms in the ${2s}^3S_1$ state, described in chapters 2 and 3: $d_{\text{beam}} = 25$ $\mu$m, $\sigma v_\perp = 0.1 v_R = 9 \times 10^{-3}$ ms$^{-1}$, $v_\parallel = 247$ ms$^{-1}$ and $\sigma v_\parallel / v_\parallel = 1.5 \times 10^{-2}$. The beam contains 92% of the atoms in $|m_g = -1\rangle$ and 8% in $|m_g = 0\rangle$. The beam flux is 250 s$^{-1}$. The rms minimum feature size on the 2D-detector was determined to be $0.13\hbar k$. The experimental setup is schematically depicted in Fig. 4.3.

A small magnetic field $\vec{B}$ of a few Gauss is used to orient the quantization axis $z$ either parallel or perpendicular to the atomic beam axis. Stern-Gerlach substate deflection is achieved by positioning a barium ferrite magnet ($40 \times 35 \times 10$ mm$^3$, 0.4 T magnetization) outside the vacuum tube at a distance of 28 mm from the atomic beam axis. The permanent magnet is positioned halfway between the interaction region and the 2D-detector. On the 2D-detector, atoms with consecutive magnetic quantum numbers $m_g$ are separated by an equivalent of 3.9 photon recoils.

The laser is tuned to the ${2s}^3S_1 \rightarrow {2p}^3P_2$ transition with a detuning $\Delta_L/(2\pi) = -120$ MHz and a power of 3 mW in the vacuum. The laser is chosen to be either lin-
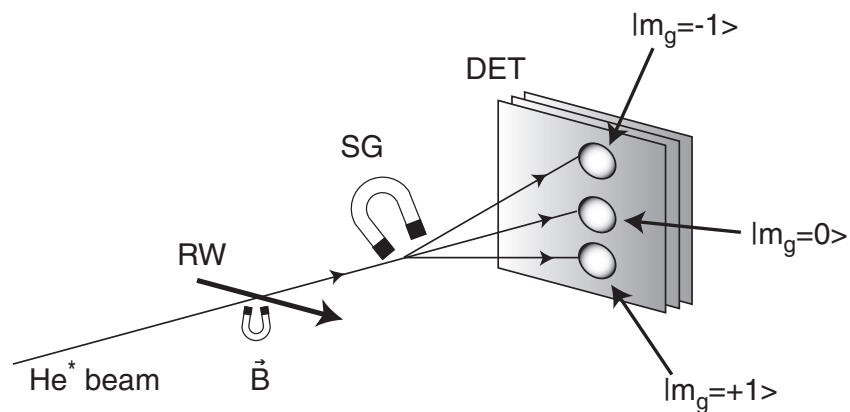
Figure 4.3: Schematic representation of the experimental setup. RW: running laser wave (tuned to $\{2s\}^3S_1 \rightarrow \{2p\}^3P_2$ transition, $\pi$- or $\sigma^+$-polarized), $\vec{B}$: weak magnetic field to orient the quantization axis $z$, SG: Stern-Gerlach state separating magnetic field and DET: single-atom 2D-detector.
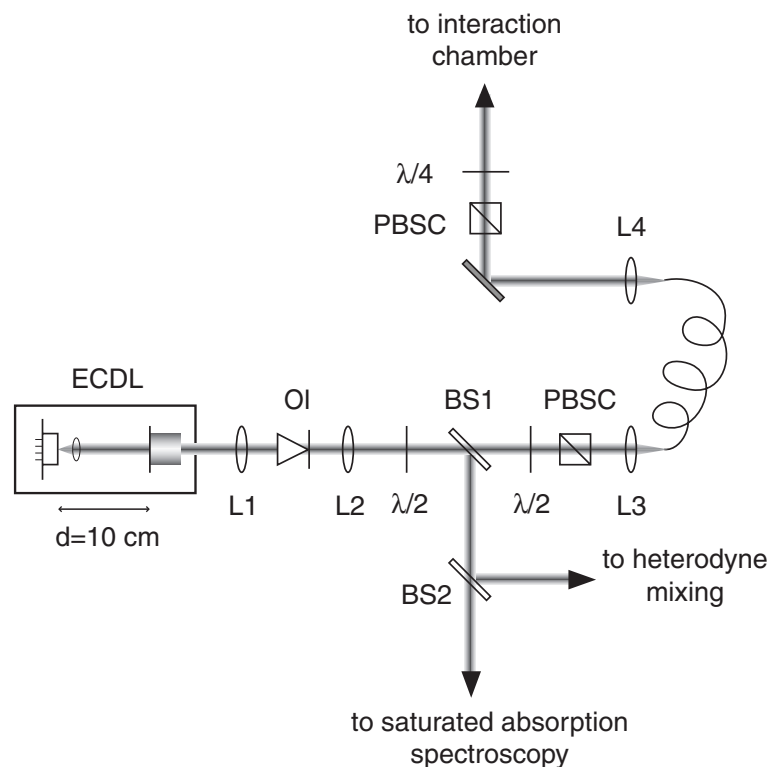


Figure 4.4: Laser setup for the running wave. ECDL: extended-cavity diode laser, L1-L4: spherical lenses, OI: optical isolator, $\lambda/2$: half wave plate, $\lambda/4$: quarter wave plate, BS1-BS2: non-polarizing beam splitters, PBSC: polarizing beam splitter cube.

early or circularly polarized, depending on the excitation scheme and the orientation of the weak magnetic field $\vec{B}$.

The laser setup for the running wave is shown in Fig. 4.4. The light for the running wave is provided by an extended-cavity diode laser (ECDL). The diode (SDL-6702H1) can give 50 mW maximum output power and has a 3 MHz free running linewidth. The output coupler of the extended cavity (10 cm length) is mounted on a tubular piezo and reflects 24% back into the diode, narrowing its linewidth down to 300 kHz [21]. The transmitted light passes an optical isolator (OFR IO-D-1083, 47 dB isolation, 75% transmission) and provides the output beam for the experiment. Part of the output power is redirected towards a standard saturated absorption spectroscopy setup, used for frequency stabilization of the laser. The laser frequency is stabilized by controlling the extended-cavity length via the piezo. Another part of the output power is optically heterodyned with light from the MOL/MOC-laser on a photodiode with integrated amplifier (200 MHz bandwidth). The resulting beat signal is displayed on a spectrum analyzer and is used for visual inspection of the laser detuning. The rest of the output beam is coupled into a single-mode polarization maintaining fiber (Thorlabs, FS-PM5121) via a variable attenuator and a $25\times$ microscope objective (Melles-Griot, $f = 7.2$ mm). The variable attenuator consists of a $\lambda/2$-plate (Eksma, quartz, low order) and a polarizing beam splitter cube (PBSC, Newport). The fiber transports the beam from the optical table to the setup and provides spatial filtering of the wavefront. The light at the output of the fiber is recollimated with a $10\times$ microscope objective (Melles-Griot, $f = 16.9$ mm) into a circular beam with waist $w_0 = 1.35$ mm. If linear light is needed, the beam passes only a final PBSC and enters the interaction chamber. In the case of circular light, an extra $\lambda/4$-plate (Eksma) is added.

# 5   Recoil imaging of spontaneous emission distributions

Because of the highly spin-polarized nature of the atomic beam, almost all atoms will be deflected to the $|m_g = -1\rangle$-spot in the absence of laser light. Even if the laser is turned on, the majority of the atoms will reach the $|m_g = -1\rangle$-spot, since the probability for spontaneous decay is well below one. These atoms will produce a high peak in the two-dimensional mapping of the detector signal. One would like to measure the discs for $M = 0$ and $M = \pm 1$ in the absence of such a high peak. This can in most cases be achieved by choosing such an excitation scheme that the atoms of interest end up at the $|m_g = 0\rangle$-spot. Still, a small peak of $|m_g = 0\rangle$ atoms will be present due to the imperfect initial spin-polarization of the beam.

Figure 4.5 shows the two-dimensional projections of $F_1^M$ for both $M = 0$ and $M = -1$ and for the two most interesting orientations of the quantization axis $z$. Discs for $M = +1$ were measured as well. As they were found to be identical to the $M = -1$ discs, they were omitted from the figure. This is in agreement with Eq. 4.2. The figure also shows the transition schemes used to observe the discs: either $\pi$- or $\sigma^+$-light was used to excite the atoms in the $|m_g = -1\rangle$-state.

Each detector image consists of 1600 bins of size $0.10\hbar k \times 0.10\hbar k$. The approx-

Table I: Total number of atoms $N_{-1,i}$ initially in state $|m_g = -1\rangle$, approximate number of atoms $N_d$ in each disc, and estimated total probability of spontaneous emission $P_s$ for each subfigure in Fig. 4.5.

| Subfigure | $N_{-1,i}$ | $N_d$ | $P_s$ |
|-----------|-----------|-------|-------|
| (a) | $85.4 \times 10^3$ | $11.5 \times 10^3$ | 0.27 |
| (b) | $85.4 \times 10^3$ | $11.0 \times 10^3$ | 0.26 |
| (c) | $84.6 \times 10^3$ | $19.0 \times 10^3$ | 0.45 |
| (d) | $83.3 \times 10^3$ | $15.5 \times 10^3$ | 0.28 |

imate number of atoms $N_d$ in each disc was determined by binning only its right half and multiplying the resulting number by two. In this way, the atoms in the bright peak were excluded from the count. Together with the number of atoms $N_{-1,i}$ initially in state $|m_g = -1\rangle$ and the Clebsch-Gordan coefficients, an estimate can be made of the total probability of spontaneous emission $P_s$. The results are shown in Table I. Note that the number of atoms $N_d$ in discs (a) and (b) are nearly equal. This agrees with the fact that the Clebsch-Gordan coefficients for both decay processes are equal.

Also, a Monte-Carlo simulation was performed to produce the simulated projections in Fig. 4.5. The program simulates the position of impact on the 2D-detector of consecutive incoming atoms by using the distributions of Eqs. 4.1 and 4.2 and a Gaussian distribution that emulates the rms minimum feature size on the 2D-detector of $0.13\hbar k$. Simulated and measured discs contain the same number of atoms and are binned in the same way.

The simulated distributions show excellent agreement with the measured distributions. In order to test the quantitative agreement, vertical strip profiles were taken through the measured discs of Fig. 4.5. Figure 4.6 shows the measured one-dimensional profiles through the center of each disc along the vertical dimension. The width of each strip was chosen to be $0.30\hbar k$. These profiles were also simulated using a large number of Monte-Carlo shots to achieve better statistics. Both profiles were plotted on top of each other with the same area under both curves. Again, the measured profiles show excellent agreement with theory. The slightly sharper features in the simulated curves are caused by the larger bin size of the measurement data.

# 6   Concluding remarks

Using atomic recoil imaging, the angular radiation distributions of spontaneous emission via electric dipole decay were measured. Both the distributions for $\pi$- and $\sigma$-transitions were observed independently for the first time. The excellent properties of our atomic beam allow us to test theory in high detail.

The detector images clearly show that atoms, which have undergone spontaneous
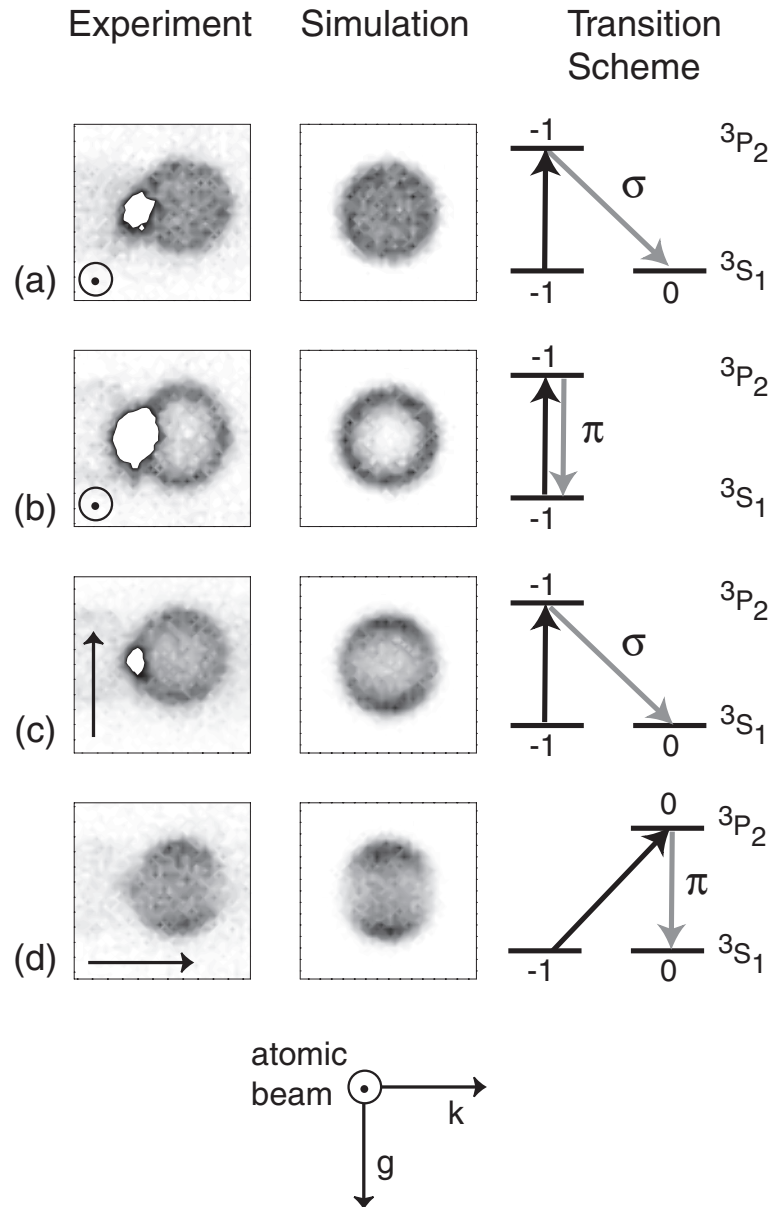
Figure 4.5: Two-dimensional projections of $F_1^M$. The size of each detector image is $4\hbar k \times 4\hbar k$. The arrow indicates the direction of the quantization axis $z$. Projections in which $z$ is parallel to the atomic beam axis are $M = -1$ (a) and $M = 0$ (b). Projections in which $z$ is perpendicular to the atomic beam axis are $M = -1$ (c) and $M = 0$ (d). The direction of the running wave is indicated by arrow $k$ and the direction of gravity by $g$. The bright spots in the experimental plots constitute atoms that did not spontaneously decay.
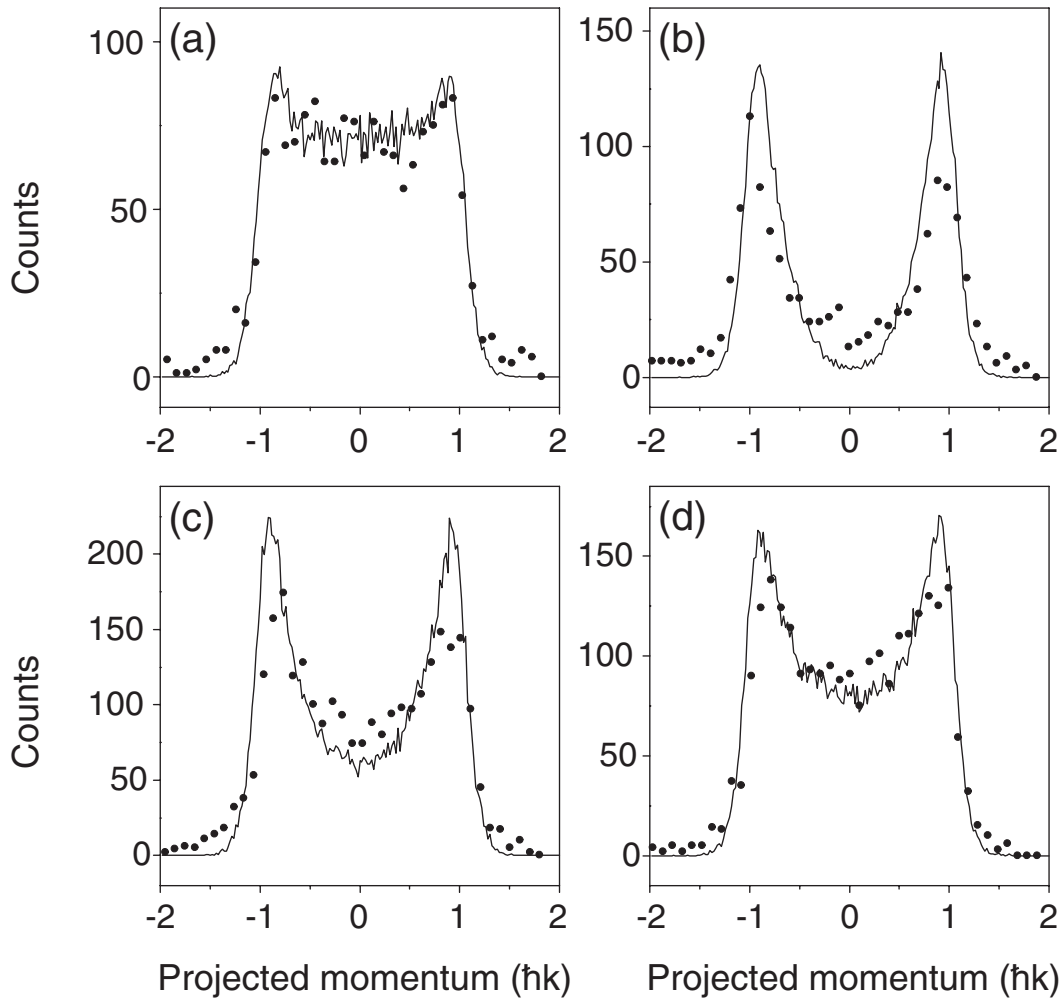
Figure 4.6: Closed circles: one-dimensional profiles taken through the center of the measured discs along the vertical dimension. The width of each strip is $0.30\hbar k$. Solid lines: simulated one-dimensional profiles of $0.30\hbar k$ strip width. Projections in which $z$ is parallel to the atomic beam axis are $M = -1$ (a) and $M$=0 (b). Projections in which $z$ is perpendicular to the atomic beam axis are $M = -1$ (c) and $M$=0 (d).

emission, can quite easily be distinguished from atoms that have not. This allows us to selectively "remove" these atoms from the data in experiments where only coherent laser-atom interactions are studied, as predicted by Knops [22]. We will use this feature extensively in chapter 5.

# References

[1] S. Chu, L. Hollberg, J.E. Bjorkholm, A. Cable, and A. Ashkin, Phys. Rev. Lett. **55**, 48 (1985).

[2] P. Lett, R. Watts, C. Westbrook, W.D. Phillips, P. Gould, and H. Metcalf, Phys. Rev. Lett. **61**, 169 (1988).

[3] J. Dalibard and C. Cohen-Tannoudji, J. Opt. Soc. Am. **B6**, 2023 (1989).

[4] A. Aspect, E. Arimondo, R. Kaiser, N. Vansteenkiste, and C. Cohen-Tannoudji, Phys. Rev. Lett. **61**, 826 (1988).

[5] M. Kasevich and S. Chu, Phys. Rev. Lett. **69**, 1741 (1992).

[6] P.L. Gould, P.J. Martin, G.A. Ruff, R.E. Stoner, J.L. Picqué, and D.E. Pritchard, Phys. Rev. A **43**, 585 (1991).

[7] L. Mandel, J. Opt. **10**, 51 (1979).

[8] T. Pfau, S. Spälter, Ch. Kurtsiefer, C.R. Ekstrom, and J. Mlynek, Phys. Rev. Lett. **73**, 1223 (1994).

[9] M. Kozuma, L. Deng, E.W. Hagley, J. Wen, R. Lutwak, K. Helmerson, S.L. Rolston, and W.D. Phillips, Phys. Rev. Lett. **82**, 871 (1999).

[10] W. Gerlach and O. Stern, Z. Phys. **8**, 110 (1922).

[11] A.S. Davydov, *Quantum mechanics* (Pergamon Press Ltd., Oxford, 1976).

[12] A. Kastler, J. Phys. et Radium **11**, 250 (1951); A. Kastler, Physica **17**, 191 (1951); A. Kastler, Proc. Phys. Soc. **67A**, 853 (1954).

[13] J. Brossel, A. Kastler, and J. Winter, J. Phys. et Radium **13**, 688 (1952).

[14] Rayleigh, Proc. Roy. Soc. **102**, 190 (1922); Rayleigh, Nature **104**, 276 (1919).

[15] R.W. Wood, Phil. Mag. **44**, 1107 (1922).

[16] R.W. Wood and A. Ellett, Proc. Roy. Soc. **103**, 396 (1923); R.W. Wood and A. Ellett, Phys. Rev. **249**, 243 (1924).

[17] W. Hanle, Zs. f. Phys. **30**, 93 (1924); W. Hanle, Ergebn. d. exakt. Naturwiss. **4**, 214 (1925).

[18] W. Hanle, Zs. f. Phys. **35**, 346 (1926); W. Hanle, Zs. f. Phys. **41**, 164 (1927); W. Hanle, Zs. f. Phys. **85**, 300 (1933); W. Hanle, Acta. Phys. Polon. **5**, 21 (1936).

[19] W. Hanle and E.F. Richter, Zs. f. Phys. **54**, 811 (1929).

[20] F. Diedrich and H. Walther, Phys. Rev. Lett. **58**, 203 (1987).

[21] M. Prevedelli, P. Cancio, G. Giusfredi, F.S. Pavone, M. Inguscio, Opt. Comm. **125**, 231 (1996).

[22] R.M.S. Knops, *Quantum optics with a cold helium beam*, Ph.D. thesis, Eindhoven University of Technology (1998).

# Chapter 5

# A coherent beam splitter for atoms by Bragg scattering

## 1 Introduction

The task of splitting a light beam in two separate parts, traveling in different directions, is an extremely easy one. Whenever light encounters an interface, defined by a change in the index of refraction, part of the light is reflected and the remainder is transmitted. If the separate parts are recombined and the difference in optical paths is less than the coherence length of the light, interference effects can be observed. This behavior can easily be understood in terms of the classical wave nature of light.

Trying to show that atoms can also behave as waves, Stern produced the first beam splitter for atoms using a diffraction technique [1]. In this 1929-experiment he diffracted an atomic beam from a periodic structure. With the advent of coherent atomic samples, produced in numerous BEC experiments [2] nowadays, it is important to note that the beam splitters addressed in this chapter, like in Stern's experiment, work for single atoms. No coherence is required between atoms that pass the beam splitter consecutively.

Since the first experiment by Stern, many techniques were explored to produce a coherent beam splitter for atoms. A formal distinction can be made between two different types of beam splitters. In the first type, the atom is prepared in a coherent superposition of internal (electronic) states. This can then be followed by a mechanism that spatially separates the different internal states. The other type of beam splitters does not change the internal state of the atom, but uses diffraction to produce a coherent superposition of external (motional) states. This second type immediately produces spatially separated paths.

In the last few years several techniques were used to produce a coherent beam splitter for atoms, such as: diffraction from free standing transmission structures [3], the magnetic Stern-Gerlach effect [4], splitting with running waves [5] or by stimulated Raman transitions [6], the optical Stern-Gerlach effect [7], a magneto-optical beam splitter [8], diffraction from a blazed phase-grating [9], and splitting by an evanescent standing wave [10].

71

Although very useful, the techniques mentioned above often have difficulties with producing two well-defined and spatially separated output beams. It is this feature that enables a beam splitter to be used in a flexible high-precision interferometer for atoms [11]. In this chapter we will show that diffracting an atomic beam under the right conditions from a standing light wave can lead to the much desired two-output coherent beam splitter. This is an optical technique for producing a coherent beam splitter. Optical techniques have the advantage that the fine tuning of the beam splitter is relatively easy. The tuning is accomplished by adjusting the laser power, frequency, polarization, and/or dimensions.

Diffraction of an atomic beam from an orthogonal standing light wave was first studied by Moskowitz *et al.* [12]. Their experiment was performed in the thin-grating or Raman-Nath regime. In this regime, the interaction time between the atom and the light field is shorter than the oscillation period of the atom in the effective potential well of the optical standing wave. The light field can then be seen as a diffracting phase-grating for the atomic wave [13]. This allows many different momentum states to be populated at the same time. Obviously, this is undesirable if one wants to make a two-port beam splitter. Recently, a Bose-Einstein condensate of sodium atoms together with a pulsed standing light wave was used to study the transition from the thin-grating to the thick-grating regime [14]. The transition shows strong oscillations in the occupation of the different momentum states as a function of the pulse duration. Still, in general, more than two momentum states are occupied, which limits its application as a two-port beam splitter.

More promising is a combination of the thick grating regime and an atomic beam that impinges on the standing light wave under a small angle. If the angle of incidence satisfies the so-called Bragg condition [13], unidirectional scattering of atoms into a single diffraction order can occur. This regime was first studied by Martin *et al.* [15] with a thermal beam of sodium atoms. Again, a sodium condensate together with a pulsed moving optical potential was recently used to study the Bragg scattering process in high resolution [16]. It was afterwards used as a tool to produce coherent four-wave mixing in which three sodium matter waves mix to produce a fourth [17]. Finally, with some minor modifications it was used to produce a quasi-continuous output coupler for the BEC, also known as an atom laser [18].

Several aspects of Bragg diffraction have been studied in the last few years. A number of experiments deal with achieving high diffraction orders, therefore producing beam splitters with large splitting angles. Up to sixth order Bragg scattering was observed in these experiments [16, 19]. For atomic beams [19] the main bottleneck for going to arbitrary high diffraction orders is usually the finite width of the longitudinal velocity distribution. At some point this will lead to spatial overlap between consecutive diffraction orders. In this chapter we will show that even higher diffraction orders can be addressed with our setup, since the atomic beam is highly monochromatic. Since condensates [16] have no initial longitudinal velocity, they have to rely on an output coupling mechanism [18] whenever a specific splitting angle is to be achieved.

Using metastable argon atoms, Oberthaler *et al.* [20] studied Bragg scattering from optical potentials that contain imaginary components. With the same setup

the influence of a time-modulated standing light wave on the diffraction process was investigated [21] and the violation of Friedel's law in atom optics was observed [22].

A number of experiments deal with the so-called Pendellösung effect [23] in atomic Bragg scattering. This effect shows the oscillatory dependence of the occupation of the diffracted momentum state on either the interaction strength or the interaction time. It was previously studied for both first and second order Bragg scattering [24–26]. The theoretical description of the effect in terms of a two-level approximation [19, 27] is expected to fail dramatically for a combination of high order Bragg scattering and strong interaction. For this purpose, we will investigate the Pendellösung effect in fifth order Bragg scattering in this chapter.

Almost all experiments, mentioned above, try to get rid of spontaneous emission during the Bragg scattering process. By increasing both laser detuning and laser power, the amount of spontaneous emission can be made arbitrarily small. In this chapter, we will allow a substantial amount of spontaneous emission during the diffraction process. As we have seen from chapter 4, atoms that undergo spontaneous emission once will be positioned on discs in transverse momentum space. The shape of and density distribution over these discs were accurately measured and found to be in excellent agreement with theory. Atoms undergoing pure Bragg scattering will be positioned on a one-dimensional grid in transverse momentum space. Two-dimensional detection of the momentum distribution after Bragg scattering allows us to separate the atoms that have spontaneously emitted a photon from those that had only coherent interaction with the standing light wave. This last group of atoms is also called the coherent fraction. With our detection technique we can therefore study the dynamics of the coherent fraction in the regime where there is a finite possibility of spontaneous emission.

In the remainder of this chapter we will first use a simple analytical model that gives insight into the basic features of atomic Bragg scattering. Then, we will use a more complex numerical approach to calculate the Bragg scattering process under experimentally realistic conditions. These calculations will be compared with the experimental results in the last part of the chapter.

## 2   Analytical analysis of atomic Bragg scattering

The theoretical description of $N^{\text{th}}$ order Bragg scattering can only be done analytically for arbitrary order $N$ if rather crude approximations are made [19]. It is very difficult to stay within these approximations in experiments where $N > 1$. A better description was given by Dürr *et al.* [25], which can produce analytical results for $N \leq 2$. Although we are not primarily interested in low order Bragg scattering in this chapter, we will give a summarized version of this description, since it clearly shows the essential properties of higher order ($N > 1$) Bragg scattering.

Consider a two-level atom with angular transition frequency $\omega_0$ interacting with a classical standing light wave with wavevector $k$ along the $x$-axis, angular frequency $\omega_L$, and electric field $E(x, t) = 2E_0 \cos(kx) \cos(\omega_L t)$. In a basis rotating with angular frequency $\omega_L$, and using the rotating-wave approximation (RWA), the Hamiltonian

reads

$$\hat{H} = -\frac{\hbar^2}{2M}\frac{\partial^2}{\partial x^2} - \hbar\Delta|e\rangle\langle e| + \hbar\Omega\{|e\rangle\langle g| + |g\rangle\langle e|\}\cos(kx), \tag{5.1}$$

in which ground and excited state are denoted by $|g\rangle$ and $|e\rangle$, respectively, and $M$ is the mass of the atom. The detuning between the light field and the atom is given by $\Delta = \omega_L - \omega_0$. The running-wave Rabi frequency is $\Omega = \mu E_0/\hbar$, where $\mu$ is the electric dipole matrix element between states $|g\rangle$ and $|e\rangle$. By demanding that $\Delta \gg \max\{\Omega, \Gamma\}$, in which $\Gamma$ is the spontaneous linewidth of the excited state, only a negligible fraction of the atoms will be in the excited state during interaction.

Furthermore, we would like to get rid of the operators that represent the internal degrees of freedom. For this purpose, consider the Hamiltonian of Eq. 5.1 in which the position-dependent terms have been neglected:

$$\hat{H} = -\hbar\Delta|e\rangle\langle e| + \hbar\Omega\{|e\rangle\langle g| + |g\rangle\langle e|\}. \tag{5.2}$$

For large detuning, $\Delta \gg \Omega$, the energy eigenstates of this Hamiltonian can be approximated by [28]

$$|g'\rangle \approx |g\rangle + (\Omega/\Delta)|e\rangle \quad \text{and} \quad |e'\rangle \approx |e\rangle - (\Omega/\Delta)|g\rangle, \tag{5.3}$$

with corresponding eigenenergies:

$$E_{g'} \approx \hbar\Omega^2/\Delta \quad \text{and} \quad E_{e'} \approx -\hbar\Delta - \hbar\Omega^2/\Delta. \tag{5.4}$$

Most experiments use a light field that has a Gaussian beam profile in the transverse direction. If the beam diameter is large enough or the atom is slow enough, the interaction between the atom and the light turns on slowly enough to ensure adiabatic passage. This requires that $\frac{d\Omega(t)}{dt} \ll \Delta^2$. In this case the light field will not induce any transitions between eigenstates $|g'\rangle$ and $|e'\rangle$. An atom entering in ground state $|g\rangle$ will adiabatically follow state $|g'\rangle$ during the interaction. The light field only shifts the energy of the ground state by $\hbar\Omega^2/\Delta$, usually referred to as the dynamical Stark shift. This way, the Hamiltonian of Eq. 5.1 can be replaced by a version in which the internal degrees of freedom have been replaced by a position-dependent light shift. This so-called adiabatic elimination of the excited state results in:

$$\hat{H} = -\frac{\hbar^2}{2M}\frac{\partial^2}{\partial x^2} + \frac{\hbar\Omega^2}{\Delta}\cos^2(kx). \tag{5.5}$$

Consider a plane atomic wave with momentum $p_x = n\hbar k$ along the standing wave. From now on, we denote such a momentum state by $|n\rangle$. We find

$$\hat{H}|n\rangle = \hbar\omega_{\text{rec}}n^2|n\rangle + \hbar\chi\{2|n\rangle + |n-2\rangle + |n+2\rangle\}, \tag{5.6}$$

in which $\omega_{\text{rec}} = \hbar k^2/(2M)$ is the recoil frequency and $\chi = \Omega^2/(4\Delta)$ is the light-shift parameter. The term $2\hbar\chi|n\rangle$ can be dropped from Eq. 5.6, since it represents a constant energy shift for all momentum states. Thus, we end up with:

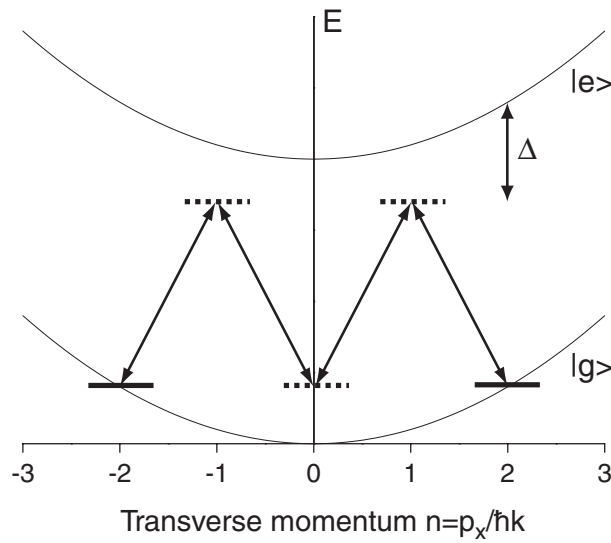$$\hat{H}|n\rangle = \hbar\omega_{\text{rec}}n^2|n\rangle + \hbar\chi\{|n-2\rangle + |n+2\rangle\}. \tag{5.7}$$

Figure 5.1: Energy of the momentum states $|n\rangle$ as a function of $n = p_x/\hbar k$, including the transition scheme for second order Bragg scattering.

## 2.1 Momentum conservation

The atomic diffraction process can be understood by examining the Hamiltonian of Eq. 5.7. The first term represents the kinetic energy of momentum state $|n\rangle$. The interaction term shows that neighboring momentum states, that differ by two photon momenta, are coupled by the light field. This just reflects momentum conservation: an atom that absorbs a photon from one running wave can re-emit it into the other running wave by stimulated emission. The total momentum of the system is conserved, since the atomic momentum changes by two photon recoils. Absorbing a photon from one running wave and re-emitting it into the same running wave by stimulated emission does not transfer any net momentum from the light field to the atom. This relatively uninteresting process is covered by the $2\hbar\chi|n\rangle$ term in Eq. 5.6.

## 2.2 Energy conservation

Figure 5.1 displays the energy of the momentum states $|n\rangle$ as a function of $n$. Atoms entering the light field in either $|n\rangle$ or $|-n\rangle$ have the same kinetic energy $\hbar\omega_{\mathrm{rec}}n^2$. Suppose the atom enters in momentum state $|n\rangle$. If the atom conserves its energy, i.e., leaves the light field with the same kinetic energy then it must leave in a coherent superposition of $|n\rangle$ and $|-n\rangle$ only. Momentum conservation further demands that $n$ must be an integer, since the atomic momentum can only be scattered over even multiples of $\hbar k$. This process is called $n^{\mathrm{th}}$-order Bragg scattering.

Whether the atom conserves its kinetic energy depends on the value of the atom-field interaction time $\tau$. For large values of $\tau$ the corresponding energy uncertainty $\Delta E_\tau = \hbar/\tau$ during interaction is relatively small. As long as it is smaller than the energy difference between the incoming momentum state and its neighboring momentum states, which is of the order of $\hbar\omega_{\mathrm{rec}}$, the atom will conserve its energy.

## 2.3   Scattering probabilities

Calculating the occupation of the Bragg diffracted momentum state analytically requires a few more considerations. These considerations turn out to be essential for understanding the exact mechanism of the Pendellösung oscillations, i.e., the dependence of the scattered fraction on the maximum light-shift parameter $\chi_0$ and the interaction time $\tau$, where:

$$\chi(t) = \chi_0 \exp(-2t^2/\tau^2). \tag{5.8}$$

Atomic population that initially occupies a single momentum state $|n\rangle$ will *during* the interaction redistribute itself over several momentum states including off-resonant states. To avoid that these off-resonant states remain occupied after interaction, the external state vector of the atom must evolve adiabatically while traversing the light field. This can be accomplished by demanding that the time-dependence of the light-shift parameter $\chi(t)$ is slow enough. For second order Bragg scattering we find [25]: $\frac{d\chi(t)}{dt} \ll \chi^2(t) + \omega_{\text{rec}}^2$. For all other orders of Bragg scattering, the criterium for adiabatic evolution of the external state vector is less stringent.

The degree of occupation of an off-resonant state $|m\rangle$ during interaction is determined by the difference in kinetic energy $\Delta E_{\text{kin}}$ between this state and the incoming state $|n\rangle$, as given by Eq. 5.7:

$$\Delta E_{\text{kin}} = \hbar\omega_{\text{rec}}(m^2 - n^2). \tag{5.9}$$

In the limit of small a light-shift parameter $\chi$, i.e., $\chi \ll \Delta E_{\text{kin}}/\hbar$, the off-resonant state $|m\rangle$ will hardly be occupied during interaction. Such a momentum state can easily be omitted from the calculation. A large light-shift parameter $\chi$, however, requires the inclusion of this momentum state in the calculation.

Take for instance second order Bragg scattering, in which $|n\rangle = |+2\rangle$. For $\chi_0 = 3\omega_{\text{rec}}$, Dürr *et al.* [25] derive that at least the states $\{|-2\rangle, |0\rangle, |+2\rangle\}$ have to be included in the calculation to obtain an accurate expression for the scattered fraction $P(-2) = |\langle -2|\Psi_{\text{out}}\rangle|^2$. They then find

$$P(-2) = \sin^2 \left[ \int_{-\infty}^{\infty} \left( -\omega_{\text{rec}} + \sqrt{\omega_{\text{rec}}^2 + \chi^2(t)/2} \right) dt \right], \tag{5.10}$$

whereas using only the resonant states $\{|-2\rangle, |+2\rangle\}$ (two-level approximation) results in [19, 27]:

$$P(-2) = \sin^2 \left[ \int_{-\infty}^{\infty} \frac{\chi^2(t)}{4\omega_{\text{rec}}} dt \right] = \sin^2 \left[ \frac{\sqrt{\pi}\chi_0^2\tau}{8\omega_{\text{rec}}} \right]. \tag{5.11}$$

Equation 5.11 can be extracted from Eq. 5.10 by expanding the root of Eq. 5.10 in a Taylor series for $\chi(t) \ll \omega_{\text{rec}}$. The difference between both equations comes from the occupation of state $|0\rangle$. Instead of only four-photon transitions that couple states $|\pm 2\rangle$, also two-photon transitions that couple states $|0\rangle$ and $|\pm 2\rangle$ have to be taken into account for $\chi_0 \sim \omega_{\text{rec}}$. In other words, state $|0\rangle$ mixes significantly into the eigenstate that is adiabatically followed during interaction. This influences the dynamics of the Pendellösung oscillations dramatically. For even higher values of

$\chi_0$ more states $|m\rangle$ with $|m| = \{4, 6, \ldots\}$ have to be included to obtain an accurate expression for $P(-2)$.

For higher order ($n > 2$) Bragg scattering, approximations beyond the two-level approximation quickly become intractable. The general expression for the scattered fraction $P(-n)$ in $n^{\text{th}}$ order Bragg scattering is given in the two-level approximation by [19]:

$$P(-n) = \sin^2 \left[ \frac{\sqrt{\frac{\pi}{2n}} \chi_0^n \tau}{2^{2n-2} [(n-1)!]^2 \omega_{\text{rec}}^{n-1}} \right]. \tag{5.12}$$

In the next section we will compare the two-level approximation with a realistic numerical calculation of fifth order Bragg scattering.

# 3   Numerical model of atomic diffraction

No analytical solution can be found for a system described by the Hamiltonian of Eq. 5.1, without using a rather large number of approximations. For this reason, we have devised an approach to solve numerically the time-dependent Schrödinger equation based on the Hamiltonian of Eq. 5.1. This approach does not require the adiabatic elimination of the excited state and can also accommodate the process of spontaneous emission.

## 3.1   Numerical approach

In first approximation, we ignore the process of spontaneous emission. The projection of the state vector $|\Psi(t)\rangle$ of the system on the $x$-axis can be written as

$$|\Psi(x,t)\rangle = \langle x|\Psi(t)\rangle = \sum_{i=g,e} |i\rangle \psi_i(x,t), \tag{5.13}$$

in which $\psi_i(x,t)$ denotes the spatial wave function for internal state $|i\rangle$. Since $\cos(kx)$ is a periodic function and the incoming de Broglie wave strongly resembles a plane atomic wave, the spatial wave function $\psi_i(x,t)$ is assumed to be periodic. This allows $\psi_i(x,t)$ to be written as

$$\psi_i(x,t) = \sum_n \phi_{i,n}(t) \exp(inkx), \tag{5.14}$$

in which $\phi_{i,n}(t)$ is the $n^{\text{th}}$ coefficient in the Fourier series expansion. Normalization is demanded by the initial condition:

$$\langle \Psi(-\infty)|\Psi(-\infty)\rangle = \sum_{i=g,e} \sum_n |\phi_{i,n}(-\infty)|^2 = 1. \tag{5.15}$$

Inserting Eqs. 5.13 and 5.14 into the time-dependent Schrödinger equation and using the orthogonality relations $\int_{-\pi/k}^{+\pi/k} \exp\{i(n-m)kx\} dx = \frac{2\pi}{k} \delta_{n,m}$ and $\langle g|e\rangle = 0$,

the following system of coupled differential equations can be derived:

$$\frac{d}{dt}\phi_{g,n}(t) = -i\{n^2\omega_{rec}\}\phi_{g,n}(t) - i\frac{\Omega(t)}{2}\{\phi_{e,n-1}(t) + \phi_{e,n+1}(t)\}, \qquad (5.16)$$

$$\frac{d}{dt}\phi_{e,n}(t) = -i\{n^2\omega_{rec} - \Delta\}\phi_{e,n}(t) - i\frac{\Omega(t)}{2}\{\phi_{g,n-1}(t) + \phi_{g,n+1}(t)\}, \quad (5.17)$$

in which the time-dependence of the Rabi frequency $\Omega(t)$ can be freely chosen: adiabatic evolution of neither the internal nor the external state vector of the atom is required. This system is implemented in a FORTRAN/77 program and is solved numerically on a Pentium PC for arbitrary initial state $|\Psi_{in}(x)\rangle$ that satisfies Eqs. 5.13, 5.14, and 5.15. The program implements a total of 64 Fourier components for the ground state and another 64 for the excited state. It uses integration and FFT routines from the NAG FORTRAN library. An additional transformation to time-dependent basis functions ensures numerical stability of the integration routine.

## 3.2   Including spontaneous emission

The coupled system of differential equations can easily be extended to include spontaneous emission. Under the assumption that a spontaneously emitted photon can not be reabsorbed, we can account for the spontaneous emission by adding a damping term to the right hand side of Eq. 5.17 [29]. This damping term, $-\phi_{e,n}(t)\Gamma/2$, gradually reduces the population of both the ground state and the excited state. At the end of the interaction region, where no laser light is present, any remaining excited state population quickly decays.

The distribution $P_{coh}(n)$ of the coherent fraction $P_{coh}$ over the momentum states $|n\rangle$ equals

$$P_{coh}(n) = |\langle n|\langle g|\Psi_{final}\rangle|^2 = |\{\phi_{g,n}\}_{final}|^2, \qquad (5.18)$$

and we define $P_{coh} = \sum_n P_{coh}(n)$.

In the general case of diffraction, both the momentum states $|g\rangle|n\rangle$ and $|e\rangle|n\rangle$ can be populated simultaneously. In the special case in which the atom enters the light field in the initial state $|g\rangle|n\rangle$, only the states $|g\rangle|n \pm 2m\rangle$ and $|e\rangle|n+1 \pm 2m\rangle$ (with $m$ being an integer) can be occupied. Figure 5.1 shows that in the case of even order Bragg scattering even values of $n$ represent diffraction of the ground state $|g\rangle$ and odd values of $n$ represent diffraction of the excited state $|e\rangle$. For odd order Bragg scattering this is exactly opposite.

Thus, the distribution $P_{coh}(n)$ produces a one-dimensional array of peaks on the 2D-detector, spaced by $2\hbar k$. These atoms have not undergone spontaneous emission, so we will use the following notations: $P_0(n) = P_{coh}(n)$ and again $P_0 = \sum_n P_0(n)$. Atoms undergoing a single spontaneous emission occupy discs located between the array of peaks. Chapter 4 showed that these discs represent the random recoil due to spontaneous emission and have a radius of $\hbar k$. The occupation of such a disc is denoted by $P_1(n)$. Again: $P_1 = \sum_n P_1(n)$. Atoms undergoing spontaneous emission more than once while traversing the light field produce even more complex patterns

on the 2D-detector. Their combined occupation will be denoted by $P_{>1}$. Normalization is ensured by: $P_0 + P_1 + P_{>1} = 1$.

## 3.3   Pendellösung behavior in fifth order Bragg scattering

To analyze the differences between the two-level approximation of Eq. 5.12 and the numerical solution of Eq. 5.18, both are plotted as a function of the running wave power $P_L$ in Figs. 5.2(a-b) for a realistic set of experimental parameters. Note that $\chi_0 \propto P_L$. The parameter set is chosen such that it ensures adiabatic evolution of both the internal and external state vector of the atom. Both plots represent the Pendellösung effect in fifth order Bragg scattering. To allow a direct comparison between both models, spontaneous emission is prevented in the numerical approach by setting $\Gamma = 0$.

The figure clearly shows differences between both models. The Pendellösung oscillations of the analytical model (a) start at a certain value of $\chi_0$ and show a rapidly increasing oscillation frequency for increasing $\chi_0$. In the exact model (b) the Pendellösung oscillations start at a slightly higher value of $\chi_0$ and the oscillation frequency saturates for high values of $\chi_0$.

This behavior can be understood by comparing Eqs. 5.10 and 5.11 in the case of second order Bragg scattering. In Eq. 5.11 the phase of the Pendellösung oscillations depends quadratically on $\chi_0$. Equation 5.10 shows a quadratic dependence for small $\chi_0$ that changes into a linear dependence for large $\chi_0$. Numerical calculations show that this result can be generalized for $N^{\text{th}}$ order Bragg scattering: the phase of the Pendellösung oscillations is proportional to $\chi_0^N$ for small $\chi_0$ and evolves into a linear dependence on $\chi_0$ for large $\chi_0$. Evidently, off-resonant states, coupled by two-photon transitions, start to mix in for large $\chi_0$.

The damping of the coherent fraction $P_0$ by spontaneous emission as a function of the running wave power $P_L$ is shown in Fig. 5.2(c). Apart from including spontaneous emission ($\Gamma/(2\pi) = 1.6$ MHz) the calculations are done for the same parameter set as used in figures 5.2(a-b). The numerical model shows that using a red-detuned standing wave ($\Delta/(2\pi) = -180$ MHz, dashed line) initially results in less spontaneous emission than using a blue-detuned standing wave ($\Delta/(2\pi) = +180$ MHz, dotted line). Both curves cross at a certain value of $P_L$.

The amount of spontaneous emission increases with increasing value of $\chi_0$. Its dependence on laser power can easily be calculated analytically if Eq. 5.5 holds and diffraction occurs in the Raman-Nath regime (short interaction time $\tau$): the light field merely acts as a phase-grating on the atomic wave [13]. Now: $P_0 = \exp(-n_s)$, in which $n_s$ is the average number of spontaneously emitted photons by a single atom traversing the light field. Using Eqs. 5.1, 5.3 and 5.8 we find

$$P_0 = \exp\left(-\int_{-\infty}^{\infty} \frac{2\Gamma\chi(t)}{\Delta}\mathrm{d}t\right) = \exp(-\chi_0\tau_c), \tag{5.19}$$

in which $\tau_c = \tau\Gamma\sqrt{2\pi}/\Delta$. The solid line in Fig. 5.2(c) represents Eq. 5.19, which is invariant under changing the sign of the detuning $\Delta$. Evidently, in the Bragg regime
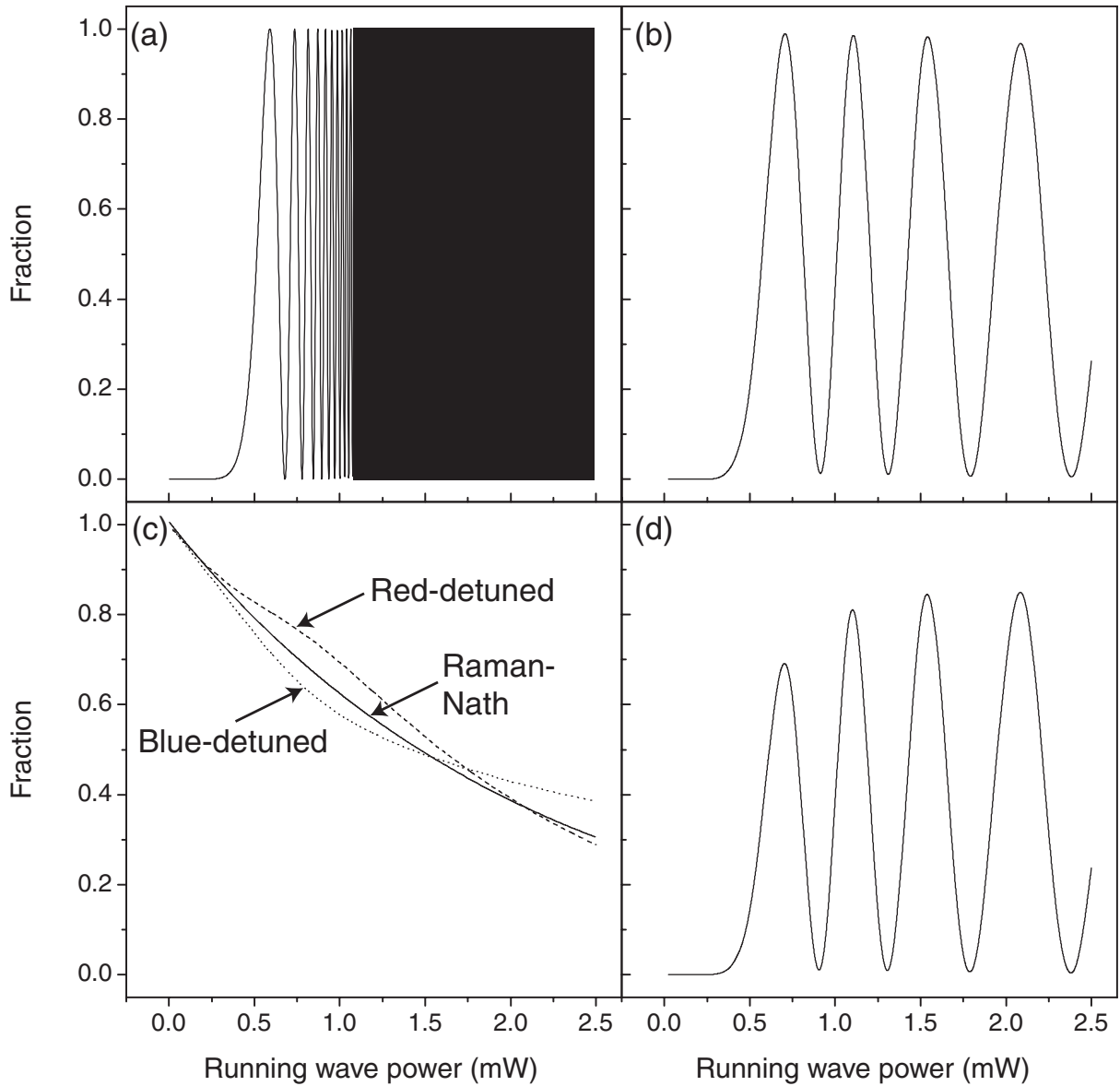
Figure 5.2: Calculated occupation of the Bragg diffracted momentum state $P_0(-5)$ as a function of the running wave power $P_L$. All calculations are done for the $\{2s\}^3S_1\,|m_g = -1\rangle \rightarrow \{2p\}^3P_2\,|m_e = -2\rangle$ transition in helium at 1083 nm. The rest of the parameters are: interaction time $\tau = 3.4\ \mu s$, waist of the Gaussian laser profile $w = 0.85$ mm and detuning $\Delta/(2\pi) = -180$ MHz. The Pendellösung behavior was calculated in the absence of spontaneous emission using (a) the two-level approximation of Eq. 5.12 and (b) the numerical model of Eq. 5.18. The solid line in (c) shows the exponential decay of the coherent fraction $P_0$ by spontaneous emission ($\Gamma/(2\pi) = 1.6$ MHz) in the Raman-Nath diffraction regime. In the Bragg regime, the decay depends on the sign of the detuning: $\Delta/(2\pi) = -180$ MHz (dashed line) and $\Delta/(2\pi) = +180$ MHz (dotted line). In (d) the atoms enter with a mismatch $\Delta n = 0.15$ from exact Bragg resonance and experience no spontaneous emission.

(large $\tau$), the dynamics of the atomic wave in the light-shift potential causes deviations from Eq. 5.19. A minimum in the light-shift potential corresponds to either a node (blue-detuned case) or an anti-node (red-detuned case) in the standing light field. Consequently, a maximum in the light-shift potential corresponds to either an anti-node (blue-detuned case) or a node (red-detuned case) in the standing light field. At relatively low laser powers, the atoms are never bound by the light-shift potential. For higher laser powers, the light-shift potential wells become deeper and the atoms enter a bound state. In the calculation of Fig. 5.2(c), where the atoms have $25\hbar\omega_{\mathrm{rec}}$ of incoming kinetic energy, this bound state is first encountered (in the center of the light field) when the laser power is tuned to produce an effective $\pi$-pulse. In the corresponding classical trajectory, these atoms spend a lot of time near the maxima in the light-shift potential. In the red-detuned case, each maximum corresponds to a node in the light field: the atoms spend a lot of their time in the "dark", leading to a relatively low amount of spontaneous emission.

Finally, we want to study the Pendellösung oscillations of atoms that enter the light field in a momentum state $|n + \Delta n\rangle$, i.e., not exactly under a Bragg angle. Figure 5.2(d) shows the Pendellösung effect in fifth order Bragg scattering for $\Delta n = 0.15$ and no spontaneous emission. The mismatch from the exact Bragg resonance reduces the maximum deflection efficiency. This effect increases with increasing $|\Delta n|$ until no Bragg scattering occurs for $|\Delta n| = 0.5$. Note that the deflection efficiency increases for increasing $\chi_0$. It shows the increasing width of the Bragg resonance in momentum space with increasing $\chi_0$.

# 4   Experimental setup

The setup for the experiment is nearly the same as the one used in chapter 4. Hence, we will only describe the differences between both situations.

The light at the output of the fiber is now recollimated with a $16\times$ microscope objective (Melles-Griot, $f = 10.8$ mm) into a circular beam with waist $w = 0.85$ mm. The light passes a polarizing beam splitter cube (PBSC) and a quarter wave plate before entering the interaction chamber with circular polarization.

For Bragg scattering a standing light wave is required. For this purpose the running wave is retroreflected by a mirror (flatness: $\lambda/4$ over 25 mm) outside the vacuum chamber. Since the windows of the interaction chamber are not anti-reflection (AR) coated this will create a 15% imbalance between the two running waves. The intensity of the standing wave component will therefore be reduced by 8%. Due to the large laser detuning ($\Delta/(2\pi) = -111\Gamma = -180$ MHz) used, the influence of the small remaining running wave component on the atomic beam can be neglected.

Figure 5.3 shows the experimental setup. The incoming atomic beam moves along the $z'$-axis. The standing light wave makes a (small) variable angle $\theta$ with the $x'$-axis and is oriented along the $x$-axis . A small magnetic field $\vec{B}$ of a few Gauss is applied along the $x'$-axis to define the quantization axis. The direction of gravity is along the $y$-axis. Rotating both the $x'$ and $z'$-axis around the $y$-axis over an angle $\theta$ results in the $x$ and $z$-axis. Special care was taken to avoid that light reflected from the non-
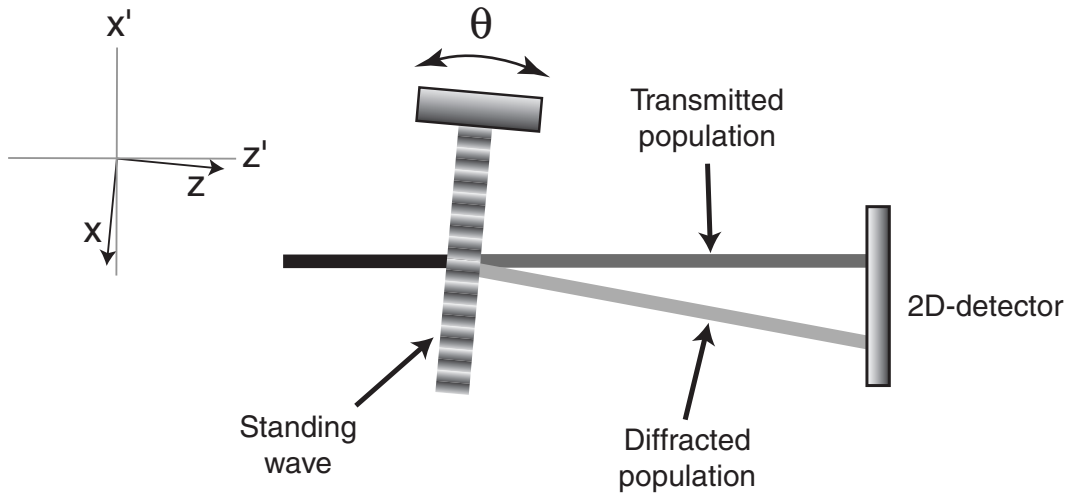
Figure 5.3: Experimental setup for atomic Bragg scattering.

AR coated windows could interfere with the standing wave. This kind of interference distorts the smooth shape of the optical potential and kills off the process of Bragg scattering.

During the Bragg scattering experiments the degree of spin-polarization of the atomic beam was not as high as in chapter 4, due to an imperfect magnetic guiding field. The beam consists of 75% $|m_g = -1\rangle$ atoms and 25% $|m_g = 0\rangle$ atoms, which was measured by a Stern-Gerlach type of magnetic substate analysis. The combination of an $|m_g = -1\rangle$ atom and $\sigma^-$-polarized laser light, tuned to the $\{2s\}^3S_1 \rightarrow \{2p\}^3P_2$ transition, produces an effective two-level system for the internal state of the atom. In the rest of the chapter we will therefore use the notation in which $|g\rangle = |1, -1\rangle$ and $|e\rangle = |2, -2\rangle$. We will see in the next sections that the motion of the $|m_g = 0\rangle$ atoms is hardly affected by the light field due to the relatively small Clebsch-Gordan coefficient of the $|1, 0\rangle \rightarrow |2, -1\rangle$ transition.

# 5   Data analysis

Determining $P_i(n)$ and $P_{>1}$ from the experimental data is not trivial due to the overlap of the coherent diffraction peaks and the incoherent discs. Two approaches have been applied. In the first approach, the data corresponding to a measured detector pattern is binned and fitted with the theoretical detector pattern. This two-dimensional fit function assumes that a coherent diffraction peak can be described by a 2D Gaussian. This constitutes an approximation, as the actual peaks show distinct non-Gaussian tails. The width of each coherent diffraction peak was determined from the detector images shown in section 7. These widths are kept fixed during the whole fit procedure. The degree of spin-polarization of the atomic beam and the use of $\sigma^-$-polarized light will result in 93% of the atoms decaying via the angular radiation distribution $F_1^{\pm 1}(\theta)$. The quantization axis is oriented along the standing wave. A disc, between two coherent diffraction peaks, can therefore be

modeled by a radial convolution between the appropriate 2D-projection of $F_1^{\pm 1}(\theta)$ and a Gaussian, representing the rms minimum feature size on the 2D-detector, of $0.13\hbar k$. The whole procedure is implemented in a PASCAL program running on a Pentium PC.

Since the fitting program is optimized for recognizing only zero and one-photon events, its output is $P_i'(n) = P_i(n)/(P_0 + P_1)$ for all $n$ and $i = \{0, 1\}$. The program is not suited for determining $P_{>1}$. We can, however, correct for multiple photon events by using the property that spontaneous emission is a Poisson process in the limit of low excitation. Thus, $P_i = \sum_n P_i(n)$ follow a Poisson distribution

$$P_i = \frac{\exp(-n_s)n_s^i}{i!}, \tag{5.20}$$

in which $n_s$ is the average number of spontaneously emitted photons by a single atom traversing the light field. Using $P_1'/P_0' = n_s$ one can derive:

$$P_i(n) = P_i'(n) \left(1 + \frac{P_1'}{P_0'}\right) \exp\left(-\frac{P_1'}{P_0'}\right). \tag{5.21}$$

We can also use a completely different fit procedure that is optimized for recognizing only zero-photon events. The approach divides the detector area into strips of width $0 \leq d_x \leq 2\hbar k$, centered around each coherent diffraction peak $n$. We then determine the fraction of atoms occupying each strip $n$ as a function of the width $d_x$, denoted by $G_n(d_x)$. Evidently, $\sum_n G_n(2\hbar k) = 1$. Each curve $G_n(d_x)$ is then fitted with a model function $G_{n,\text{fit}}(d_x) = A_n G_{0,n}(d_x) + B_n G_{>0,n}(d_x)$, in which $A_n$ and $B_n$ are fit coefficients. The model function $G_{0,n}(d_x)$ is the cumulative distribution function of population in the coherent diffraction peak $n$. $G_{>0,n}(d_x)$ is a model function for the cumulative distribution function of population in the strip $n$ that has undergone spontaneous emission. From examining the data we find that $G_{0,n}(d_x)$ can be accurately approximated by: $G_{0,n}(d_x) = \text{erf}(d_x/w_{n,1}) + (2/\pi)\alpha \times \arctan(d_x/w_{n,2})$, in which $\alpha$ is independent from $n$ and is determined from the peak produced by the incoming momentum state. This corresponds to a non-cumulative distribution function which consists of a Gaussian of width $w_{n,1}$ and a Lorentzian of width $w_{n,2}$. These widths are determined from the detector images shown in section 7 and are also kept fixed during fitting. Furthermore, we use $G_{>0,n}(d_x) = d_x$.

This last approach is capable of immediately determining $P_0(n)$ for all $n$ by evaluating $P_0(n) = A_n(\alpha + 1)$. When fitting detector patterns we always use both approaches and have found that they give the same values of $P_0(n)$ to within 4%.

# 6   Pendellösung oscillations in fifth order Bragg scattering

Since our atomic beam is monochromatic ($\sigma v_{\parallel}/v_{\parallel} = 1.5 \times 10^{-2}$), slow ($v_{\parallel} = 247$ ms$^{-1}$), narrow ($d_{\text{beam}} = 25$ $\mu$m), and well-collimated ($\sigma v_{\perp} = 0.10 v_R = 9 \times 10^{-3}$ ms$^{-1}$) we are able to make an accurate two-port beam splitter with a large splitting angle $2\theta$.
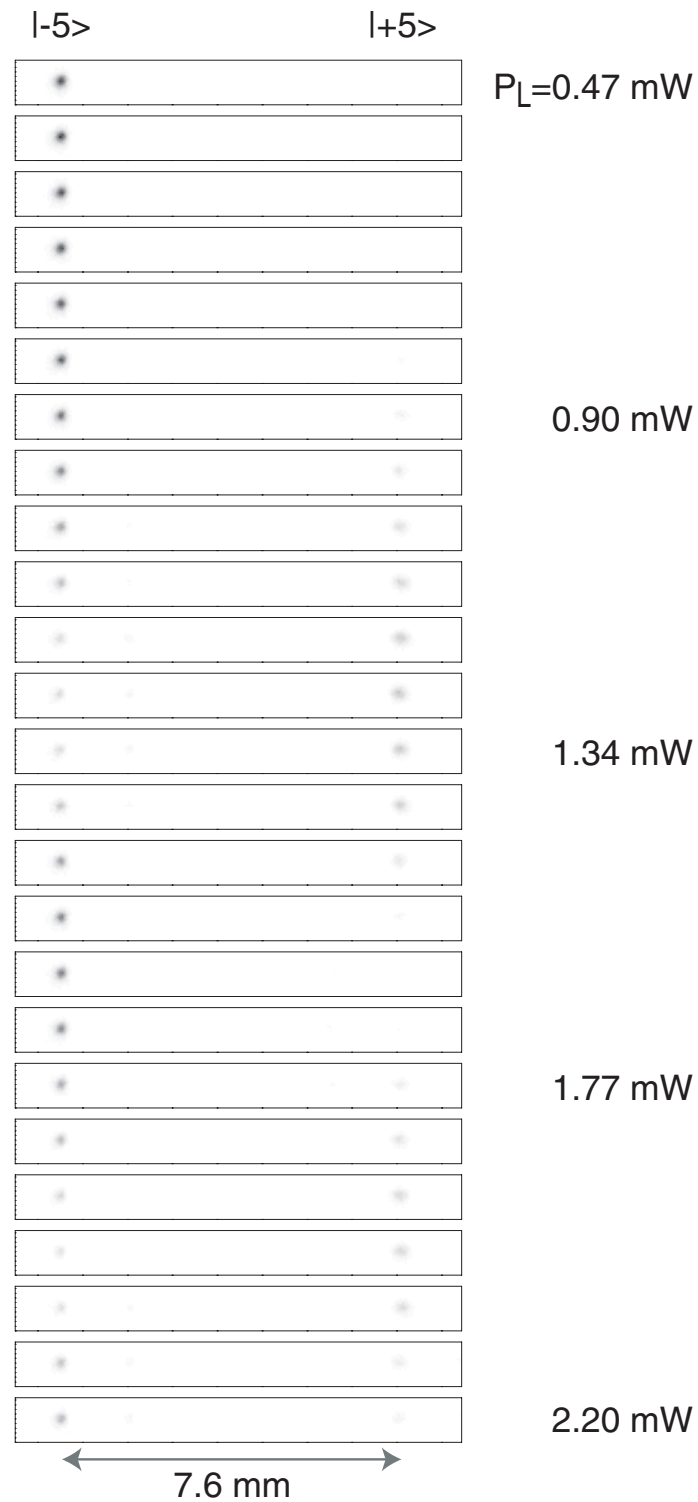
Figure 5.4: Pendellösung oscillations in fifth order Bragg scattering. Each image contains 10000 atoms distributed over $0.07\hbar k \times 0.07\hbar k$ sized bins. The incoming momentum state is $|-5\rangle$ and the Bragg diffracted momentum state is $|+5\rangle$.

By freely varying all the experimental parameters that determine the exact shape of the Pendellösung oscillations, we could produce a beam splitter with any desired value of the reflection coefficient $R$, transmission coefficient $T$, and absorption coefficient $A$, where $R + T + A = 1$. The absorption coefficient $A$ describes the loss by spontaneous emission. Because of experimental simplicity we only vary the laser power $P_L$. In other words, we only change the maximum light-shift parameter $\chi_0$. Even by varying just this single parameter most of the the interesting properties of Bragg scattering can be extracted from the data. The time-dependence of the light-shift parameter is, in the rest frame of the atom defined by $t = z/v$, given by

$$\chi(t) = \chi_0 \exp(-2(y^2 + v^2 t^2)/w^2) = \frac{P_L \Gamma^2}{4\pi w^2 I_0 \Delta} \exp(-2y^2/w^2) \exp(-2t^2/\tau^2), \quad (5.22)$$

in which $I_0$ is the saturation intensity of the atomic transition ($I_0 = 1.67$ W/m$^2$ for $|1,-1\rangle \rightarrow |2,-2\rangle$), $\tau = w/v$, $\Gamma/(2\pi) = 1.6$ MHz, $\Delta/(2\pi) = -180$ MHz, $w = 0.85$ mm and $y$ is the $y$-position of the atomic beam with respect to the center of the light field. Ideally, $y = 0$. A non-zero value of $|y|$ can therefore accommodate a slight alignment error between the atomic beam and the standing wave.

For $y = 0$ and maximum laser power ($P_{L,max} = 3$ mW), adiabatic elimination of the excited state is allowed and the evolution of the system should follow the Hamiltonian of Eq. 5.5, since $\Delta/\Omega_{0,max} = 4.0$ and $|\frac{d\Omega}{dt}|_{max}/\Delta^2 = 5.6 \times 10^{-5}$. It is estimated that for maximum laser power we need $\tau \gg 0.3$ $\mu$s to ensure adiabatic evolution of the external state vector. In the experiment $\tau = 3.4$ $\mu$s. Since $\chi_{0,max}/\omega_{rec} = 69$, off-resonant momentum states are expected to be populated during interaction as shown in section 2.3.

In this section we will present experimental results for fifth order Bragg scattering. Pendellösung oscillations are studied by varying the laser power from zero to the maximum of 3 mW. The measured detector images for individual laser powers are depicted in Fig. 5.4. Each image contains 10000 atoms. The area of each bin is $0.07\hbar k \times 0.07\hbar k$. The grayscale range is the same for all of the images. The oscillations between the population in the incoming momentum state $|-5\rangle$ and the resonant momentum state $|+5\rangle$ are clearly visible in the data. The influence of increasing spontaneous emission can also be seen in the images: the total coherent population decreases with increasing laser power.

The data markers in Fig. 5.5(a) show the measured occupation of both momentum states as a function of the laser power $P_L$. It also shows the total occupation of the odd diffraction orders, i.e., the total coherent fraction $P_0$. Here we define that $T = P_0(-5)$ and $R = P_0(+5)$.

We observe that $T$ does not go to zero. This is mainly caused by the low deflection efficiency of the 25% $|m_g = 0\rangle$ atoms. The $|1,0\rangle \rightarrow |2,-1\rangle$ transition has a saturation intensity of 3.34 W/m$^2$: the $|m_g = 0\rangle$ atoms will therefore only see half the light-shift. They will obtain a lower Pendellösung phase and will experience a lower loss due to spontaneous emission. Figure 5.5(b) shows the transmission efficiency, $T/P_0$, and the reflection efficiency, $R/P_0$, as a function of $P_L$.

The solid lines in Figs. 5.5(a-b) represent the calculated curves, based on Eq. 5.18. The calculation has only two free parameters: the $y$-position of the atomic beam
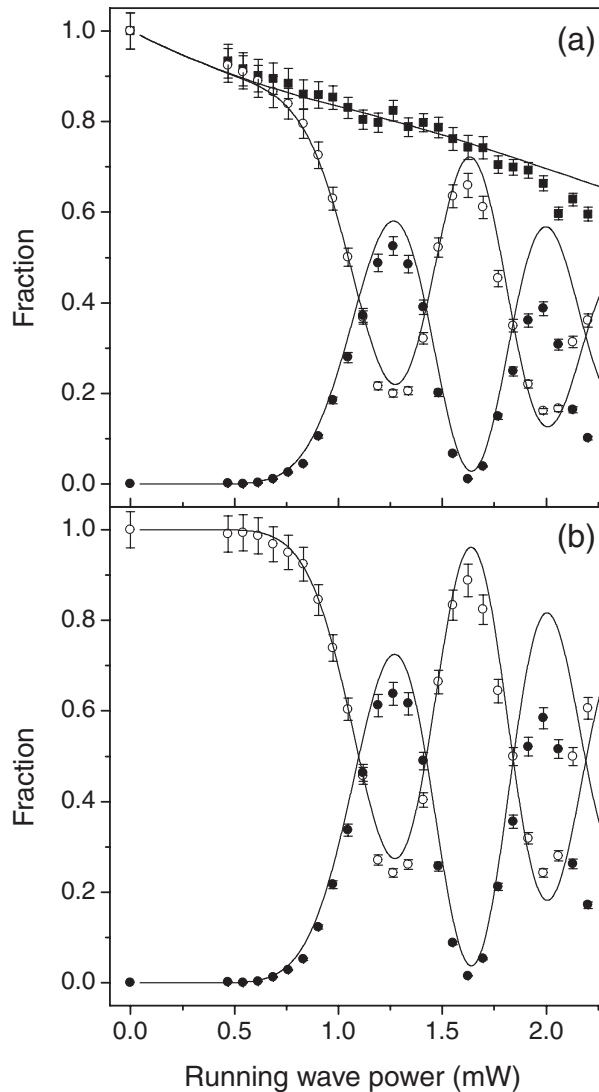
Figure 5.5: Pendellösung oscillations in fifth order Bragg scattering. (a) Measured occupation of the incoming momentum state $|-5\rangle$ ($T$, open circles), the Bragg diffracted momentum state $|+5\rangle$ ($R$, full circles) and the total coherent fraction ($P_0$, full squares) as a function of the laser power $P_L$. (b) Measured values of the transmission efficiency $T/P_0$ (open circles) and the reflection efficiency $R/P_0$ (full circles) as a function of the laser power $P_L$. The solid lines are the calculated curves for $|y| = 0.46$ mm and $\Delta n = 0$.

while traversing the light field and a possible mismatch from the exact Bragg resonance $\Delta n$, both of which are very difficult to determine accurately a priori. The rest of the parameters are taken from the experiment, including the observed degree of spin-polarization of the atomic beam. For $|y| = 0.46$ mm and $\Delta n = 0$ a good agreement between theory and experiment is achieved.

For high laser power the measured reflection efficiency $R/P_0$ is significantly lower than the calculated value. The transmission efficiency $T/P_0$, however, accurately follows the calculated behavior. For these powers, population is transferred to off-
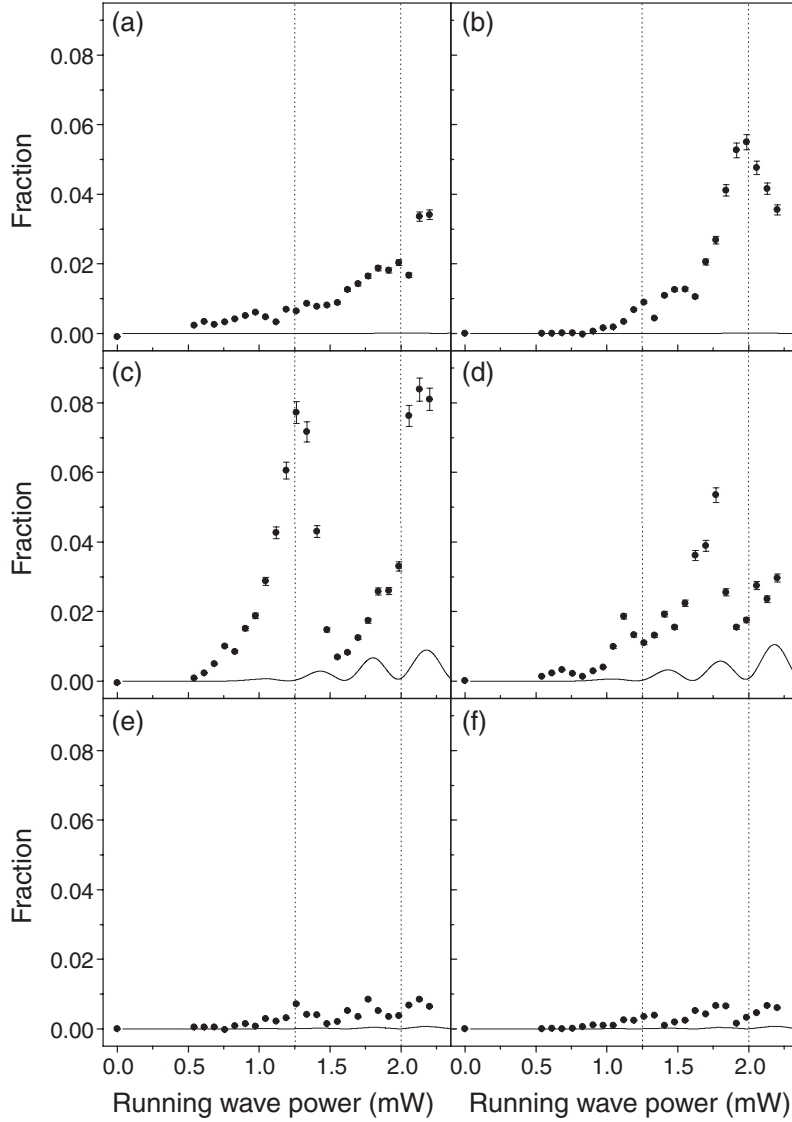
Figure 5.6: Scaled occupation of the off-resonant odd diffraction orders, $P_0(n)/P_0$, as a function of $P_L$. The full circles are the measured data points and the solid lines represent the calculated curves for $|y| = 0.46$ mm and $\Delta n = 0$. The dotted lines mark the position of the maxima in $R/P_0$. (a) $n = -7$, (b) $n = +7$, (c) $n = -3$, (d) $n = +3$, (e) $n = -1$ and (f) $n = +1$.

resonant odd momentum states.

The data markers in Fig. 5.6 show the scaled occupation of the off-resonant odd diffraction orders, $P_0(n)/P_0$, as a function of $P_L$. Only the odd diffraction orders with $|n| \leq 7$ show significant occupation. The numerical calculations show that the occupation of each of these off-resonant states should still be below 1%. We observe much higher values of $P_0(n)/P_0$ in the measurements. We attribute the high degree of occupation of the off-resonant states to imperfections in the wavefront of the standing light field, causing non-adiabatic transitions in the external state vector.

# 7    Bragg scattering up to eighth order

By tuning the angle of incidence $\theta$ one can determine the order of Bragg scattering $N$. For first order ($N = 1$) Bragg scattering $\theta = 0.37$ mrad. As long as consecutive diffraction orders do not merge on the 2D-detector and one can produce a sufficiently high value for the Pendellösung phase, the Bragg scattering order $N$ can be increased. These measurements are shown in Fig. 5.7. Each detector image contains 25000 atoms. The area of each bin is $0.10\hbar k \times 0.10\hbar k$. The grayscale ranges are different for each individual image. They are scaled to the bin with the highest number of atoms.

For $1 \leq N \leq 5$ the value of $R = P_0(+N)$ was maximized, i.e., $\chi_0$ was tuned to the first maximum of $R$ in the Pendellösung oscillations. Figure 5.7 shows that $T = P_0(-N) \neq 0$. Analysis of the data shows that $T/P_0$ increases from 0.15 for $N = 1$ to 0.25 for $N = 5$. We believe that this is caused by the low deflection efficiency of the 25% $|m_g = 0\rangle$ atoms, as discussed in the previous section. An approximate expression of $T/P_0$ can be derived to be

$$T/P_0 = \frac{\left(1 - \sin^2\left[\left(\frac{1}{2}\right)^N \frac{\pi}{2}\right]\right) f_0}{f_0 + f_{-1} \exp\left(-\frac{1}{2}\chi_0 \exp(-2y^2/w^2)\tau_c\right)}, \tag{5.23}$$

in which $f_0 = 0.25$ and $f_{-1} = 0.75$.

The approximation uses the $\chi_0^N$-dependence of the initial part of the Pendellösung oscillation. It also assumes that the $|m_g = -1\rangle$ atoms have experienced an effective $\pi$-pulse, which completely removes them from the incoming momentum state. Furthermore, $|m_g = 0\rangle$ atoms are expected to undergo less spontaneous emission due to the lower Clebsch-Gordan coefficient. Equation 5.23 predicts that $T/P_0 = 0.13$ for $N = 1$ and 0.27 for $N = 5$. This agrees with the observed values.

The beam splitter for $N = 2$ shows some population of intermediate off-resonant states. By moving to higher orders, the kinetic energy difference between the incoming momentum state and its neighboring momentum states increases, which lowers the occupation of the off-resonant states *during* interaction. This will also allow the external state vector to evolve more adiabatically. High order beam splitters show negligible occupation of the off-resonant states. The data thus shows increasing adiabatic behavior of the external state vector for increasing Bragg order.

The maximum laser power $P_{L,max} = 3$ mW prevents us from providing an effective $\pi$-pulse for $N > 5$. Thus, beam splitters with $R \approx T$ are made for sixth, seventh and eighth order Bragg scattering. This gives a maximum splitting angle of 5.9 mrad between both ports of the beam splitter. With an atomic beam diameter of 25 $\mu$m the atom only has to travel 4.2 mm before both momentum states of the coherent superposition are spatially separated.

Since the diffracted beam stays well within its own diffraction order on the 2D-detector, even for eighth order Bragg scattering, we could in principle go further if we had more laser power. The width of the eighth order diffraction peak on the 2D-detector is 203 $\mu$m rms. This is still considerably smaller than the projection of $\hbar k$ on the detector, which is 760 $\mu$m. The incoming momentum state produces a 98 $\mu$m
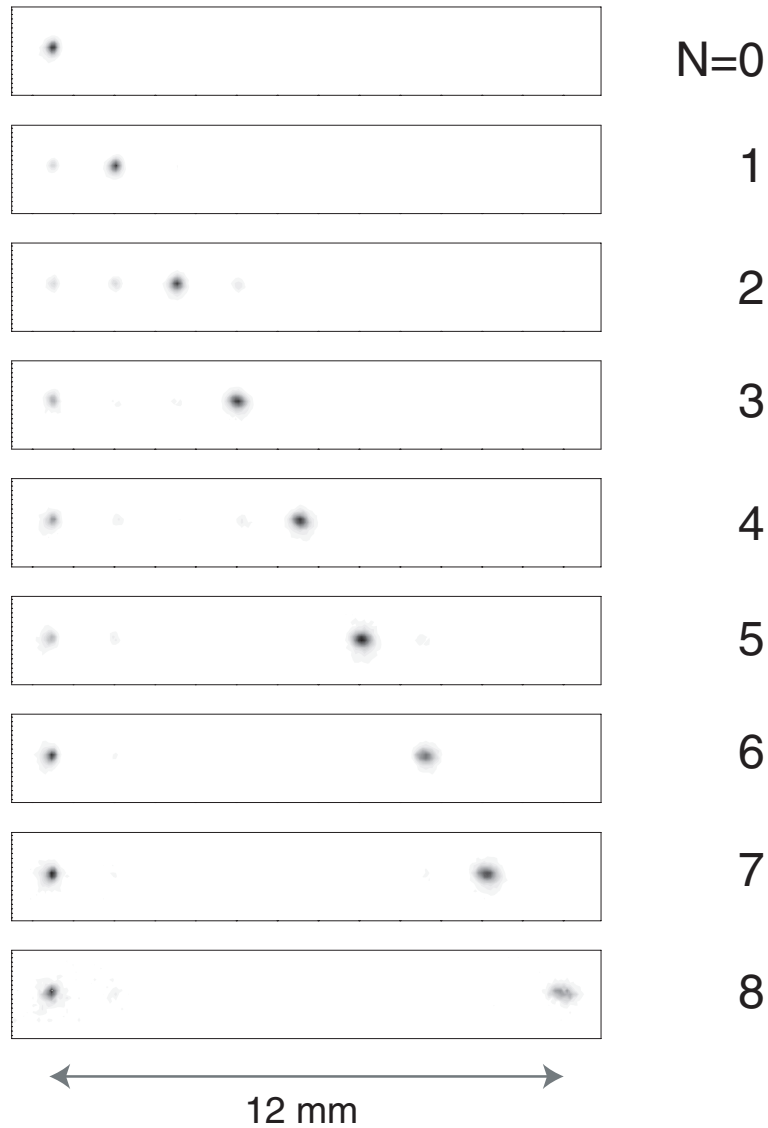
Figure 5.7: Bragg scattering for increasing order $N$. Each image contains 25000 atoms distributed over $0.10\hbar k \times 0.10\hbar k$ sized bins.

rms peak on the detector. Note that the real width of the beams is actually smaller, since the detector has a finite resolution of 60 $\mu$m rms. Extrapolating these results one could theoretically go up to $34^{\text{th}}$ order Bragg scattering before diffraction orders start to overlap. This would produce a 25 mrad angle between the two output ports!

The power limitation is primarily caused by a low coupling efficiency of the laser light into the single-mode polarization maintaining fiber. We obtain a coupling efficiency of 28%. This low efficiency is primarily caused by the elliptical shape of the laser beam and the astigmatism in the wavefront when entering the coupling lens. Better mode-matching should improve the coupling efficiency. In the past, values up to 70% were obtained with the same coupling optics and a different single-mode polarization maintaining fiber [30].

Note that at $N = 8$ the non-linear behavior in the position determination on

the 2D-detector becomes visible. Although the incoming momentum state hits the detector exactly in the center, the diffracted momentum state is displaced 12 mm towards the edge of the resistive anode, causing a non-linear charge distribution over the four corner points of the anode. Going to $N > 8$ requires that either the detector is moved closer to the interaction chamber or that the detector is placed off-axis.

## 8   Concluding remarks

We have produced a coherent two-port beam splitter for He* with a variable splitting ratio $R/T$ by atomic Bragg scattering. The splitting ratio can be efficiently tuned by altering the laser power $P_L$. Under the current conditions we achieve a maximum splitting angle of 5.9 mrad by allowing approximately 40% spontaneous emission. Due to the monochromaticity of the atomic beam, both the splitting angle and the splitting ratio are very well defined. Using more laser power $P_L$ and a higher detuning $\Delta$, the angle could be increased and the amount of spontaneous emission could be made smaller.

With three of these accurate beam splitters (two 50/50-beam splitters and one 100/0-beam splitter) one can make an accurate atom interferometer with a high fringe contrast. Using tenth order Bragg scattering and the current setup we should be able to make an interferometer with an enclosed area of 5400 mm$^2$ and a maximum path separation of 6 mm. This allows macroscopic objects to be inserted into the interferometer.

Since most interferometers require only one-dimensional collimation of the atomic beam, collimating slits of 1 mm $\times$ 25 $\mu$m can be used. This should provide an atomic beam flux of $2 \times 10^5$ s$^{-1}$. A high beam flux reduces the amount of shot-noise in the readout port of the interferometer. The high degree of monochromaticity of the atomic beam ensures a relatively large longitudinal coherence length of the atoms. This gives the interferometer a large dynamic range.

By using better magnetic guiding, as done in chapter 4, we can produce a nearly perfectly spin-polarized atomic beam of $|m_g = -1\rangle$ atoms. Due to the low deflection efficiency, any remaining $|m_g = 0\rangle$ atoms will not be reflected by the 100/0-beam splitter of the interferometer. This effectively removes them from the interferometer.

## References

[1] O. Stern, Naturwissensch. **17**, 391 (1929).

[2] M.H. Anderson *et al.*, Science **269**, 198 (1995); K.B. Davis *et al.*, Phys. Rev. Lett. **75**, 3969 (1995); C.C. Bradley *et al.*, Phys. Rev. Lett. **75**, 1687 (1995); D.G. Fried *et al.*, Phys. Rev. Lett. **81**, 3811 (1998).

[3] O. Carnal and J. Mlynek, Phys. Rev. Lett. **66**, 2689 (1991); D.W. Keith, C.R. Ekstrom, Q.A. Turchette, and D.E. Pritchard, Phys. Rev. Lett. **66**, 2692 (1991).

[4] Ch. Miniatura, J. Robert, S. Le Boiteux, J. Reinhardt, and J. Baudon, Appl. Phys. B **54**, 347 (1992).

[5] Ch. J. Bordé, N. Courtier, F. du Burck, A.N. Goncharov, and M. Gorlicki, Phys. Lett. A **188**, 187 (1994).

[6] M. Kasevich and S. Chu, Phys. Rev. Lett. **67**, 181 (1991); D.S. Weiss, B.C. Young, and S. Chu, Phys. Rev. Lett. **70**, 2706 (1993).

[7] T. Sleator, T. Pfau, V. Balykin, O. Carnal, and J. Mlynek, Phys. Rev. Lett. **68**, 1996 (1992).

[8] T. Pfau, Ch. Kurtsiefer, C.S. Adams, M. Sigel, and J. Mlynek, Phys. Rev. Lett. **71**, 3427 (1993).

[9] K.S. Johnson, A.P. Chu, K.K. Berggren, M. Prentiss, Opt. Comm. **126**, 326 (1996).

[10] R. Brouri, R. Asimov, M. Gorlicki, S. Feron, J. Reinhardt, V. Lorent, H. Haberland, Opt. Comm. **124**, 448 (1996).

[11] David M. Giltner, Roger W. McGowan, and Siu Au Lee, Phys. Rev. Lett. **75**, 2638 (1995).

[12] P.E. Moskowitz, P.L. Gould, S.R. Atlas, and D.E. Pritchard, Phys. Rev. Lett. **51**, 370 (1983); P.L. Gould, G.A. Ruff, and D.E. Pritchard, Phys. Rev. Lett. **56**, 827 (1986).

[13] A.P. Kazantsev, G.I. Surdutovick, and V.P. Yakovlev, *Mechanical action of light on atoms* (World Scientific, Singapore, 1990).

[14] Yu. B. Ovchinnikov, J.H. Müller, M.R. Doery, E.J.D. Vredenbregt, K. Helmerson, S.L. Rolston, and W.D. Phillips, Phys. Rev. Lett. **83**, 284 (1999).

[15] P.J. Martin, B.G. Oldaker, A.H. Miklich, and D.E. Pritchard, Phys. Rev. Lett. **60**, 515 (1988).

[16] M. Kozuma, L. Deng, E.W. Hagley, J. Wen, R. Lutwak, K. Helmerson, S.L. Rolston, and W.D. Phillips, Phys. Rev. Lett. **82**, 871 (1999).

[17] L. Deng, E.W. Hagley, J. Wen, M. Trippenbach, Y. Band, P.S. Julienne, J.E. Simsarian, K. Helmerson, S.L. Rolston, and W.D. Phillips, Nature **398**, 218 (1999).

[18] E.W. Hagley, L. Deng, M. Kozuma, J. Wen, K. Helmerson, S.L. Rolston, and W.D. Phillips, Science **283**, 1706 (1999).

[19] David M. Giltner, Roger W. McGowan, and Siu Au Lee, Phys. Rev. A **52**, 3966 (1995).

[20] M.K. Oberthaler, R. Abfalterer, S. Bernet, J. Schmiedmayer, and A. Zeilinger, Phys. Rev. Lett. **77**, 4980 (1996).

[21] S. Bernet, M.K. Oberthaler, R. Abfalterer, J. Schmiedmayer, and A. Zeilinger, Phys. Rev. Lett **77**, 5160 (1996).

[22] C. Keller, M.K. Oberthaler, R. Abfalterer, S. Bernet, J. Schmiedmayer, and A. Zeilinger, Phys. Rev. Lett. **79**, 3327 (1997).

[23] P.P. Ewald, Ann. Phys. **54**, 519 (1917).

[24] S. Kunze, S. Dürr, and G. Rempe, Europhys. Lett. **34**, 343 (1996).

[25] S. Dürr, S. Kunze, and G. Rempe, Quantum Semiclass. Opt. **8**, 531 (1996).

[26] S. Dürr and G. Rempe, Phys. Rev. A **59**, 1495 (1999).

[27] A.F. Bernhardt and B.W. Shore, Phys. Rev. A **23**, 1290 (1981).

[28] C. Cohen-Tannoudji, B. Diu, and F. Laloë, *Quantum mechanics* (Wiley, New York, 1977).

[29] B.R. Mollow, Phys. Rev. A **12**, 1919 (1975).

[30] M.D. Hoogerland, Ph.D. thesis, Eindhoven University of Technology, 1993.

# Summary

Over the last two decades the field of laser cooling has produced numerous techniques to efficiently manipulate the quantum state of atoms. This enables the experimental verification of many textbook cases in which a single atom, residing in a specific initial quantum state, interacts with a well-defined light field. The interaction changes the atomic state and this can be observed with the proper detection technique. In this thesis we have implemented some of these laser cooling techniques to produce a beam of helium atoms in the metastable $\{2s\}^3S_1$ state (denoted by He*), which is then used to perform atom optics experiments. The setup is designed in such a way that it can be used in the future for a whole range of quantum optics and atom optics experiments. This research was carried out in the Atomic Physics and Quantum Electronics group at the Physics Department of the Eindhoven University of Technology.

The experiments described in this thesis require a very high-quality He* beam. For this purpose, we have constructed a beam setup that uses one longitudinal and three two-dimensional transverse laser cooling sections, combined with a mechanical collimating section, to produce the desired atomic beam. Atoms emerging from a metastable helium source are collimated, slowed, focused, and compressed by the laser cooling sections. The final mechanical collimation is taken care of by a pair of small apertures. This way, we produce a narrow (25 $\mu$m diameter), slow (247 ms$^{-1}$), monochromatic (1.5% rms velocity spread) and ultra-collimated (36 $\mu$rad rms divergence) He* beam. We achieve a beam flux of 250 s$^{-1}$, which is sufficient for the experiments described in this thesis. Without the three transverse laser cooling sections the beam flux would be in the order of two atoms per hour. Experiments that now require 5 minutes of data-acquisition time would then take about 4 years or 1 Ph.D.-period to complete! In this thesis we use the helium $\{2s\}^3S_1 \rightarrow \{2p\}^3P_2$ transition, at the optical wavelength $\lambda$ = 1083 nm, for both atom optics and laser cooling. The laser light is generated by diode lasers.

A metastable helium atom absorbing or emitting a 1083 nm photon changes its velocity by the recoil velocity $v_R$ = 0.092 ms$^{-1}$. This leads to a change in the motional state of the atom. We use a two-dimensional position-sensitive single-atom detector, placed 2 m behind the light field, to measure the change in transverse atomic velocity with an overall rms resolution of $0.13v_R$. The 2D-detector is also used to fully characterize the atomic beam: both the initial electronic and motional state of the atoms is measured with high precision. Information on the electronic state is obtained by a state-selective deflection technique based on the Stern-Gerlach effect. These measurements show that the initial atomic beam is spin-polarized if sufficient magnetic guiding is used. Either a pure beam of $m$ = 0 atoms, in which $m$ is the magnetic quantum number, or a pure beam of $m$ = −1 atoms can be produced. The latter is of considerable importance, as it constitutes a beam of effective two-level atoms when combined with $\sigma^-$-polarized laser light.

An atom experiencing spontaneous emission will emit a photon in a random direction. The angular distributions of dipole radiation are expected to be anisotropic. Furthermore, they depend on the polarization of the emitted photon. Two distinct distributions, associated with decay via either a $\pi$- or a $\sigma$-transition, are predicted by theory. In this thesis we show that both distributions can, for the first time, be independently measured. For this purpose, we let the atoms in the beam interact with a weak running wave, which causes some of the atoms to spontaneously emit a photon. The recoil associated with the emitted photon causes the atoms to be deflected. The corresponding deflection patterns are measured on the 2D-detector and immediately reflect the angular distributions of spontaneous emission. A state-selective deflection technique, based on the Stern-Gerlach effect, is used to distinguish between $\pi$- and $\sigma$-transitions.

In addition to studying the spontaneous radiation force, we also perform an experiment in which the dipole force is dominant. Here, we let the the atomic beam interact with an off-resonant standing light wave. The cold atoms in the beam, which behave like plane atomic waves, are diffracted by the periodic dipole potential. By tuning the experimental parameters into the Bragg regime, the motional state of each atom is prepared into a coherent superposition of only two momentum states. Thus, the standing light wave acts as a coherent beam splitter for atoms: each "splitted" atomic wavepacket moves along two spatially separated paths at the same time. The splitting ratio of the beam splitter is tuned with the intensity of the standing light wave. We achieve up to eighth order Bragg scattering and produce a tunable, coherent beam splitter for atoms with two well-defined output ports and a maximum splitting angle of 5.9 mrad. This leads to a macroscopic path separation of up to 12 mm on the 2D-detector. Atoms that undergo spontaneous emission during the Bragg scattering process can easily be identified on the 2D-detector due to the acquired random photon recoil. This allows us to selectively remove them from the measurement. A possible future experiment could use three of these Bragg beam splitters to produce an atom interferometer with a very large enclosed area between the arms and a macroscopic path separation.

The experiments performed in this thesis show that our high-quality atomic beam setup can be used to perform atom optics experiments with a resolution comparable to BEC experiments. Being a beam setup, it is especially suited for future cavity QED experiments in which the atom has to traverse the light field in less than the cavity damping time.

# Samenvatting

Gedurende de afgelopen twee decennia zijn vele laserkoelingstechnieken ontwikkeld om de quantumtoestand van atomen op efficiënte wijze te manipuleren. Hiermee worden allerlei experimenten mogelijk waarin één enkel atoom, dat zich in een goed gedefinieerde quantumtoestand bevindt, wisselwerkt met een lichtveld. Met de juiste detectietechnieken kan de resulterende verandering in the atomaire toestand waargenomen worden. Sommige van deze laserkoelingstechnieken worden in dit proefschrift gebruikt om een bundel van helium atomen in de $\{2s\}^3S_1$ toestand (ook wel He* genoemd) te maken, die vervolgens in verschillende atoomoptica experimenten gebruikt wordt. De opstelling is zo ontworpen dat hij, in de toekomst, voor een hele reeks quantumoptica en atoomoptica experimenten gebruikt kan worden. Dit onderzoek is uitgevoerd in de capaciteitsgroep Atoomfysica en Quantumelektronica van de faculteit Technische Natuurkunde aan de Technische Universiteit Eindhoven.

De experimeten beschreven in dit proefschrift vereisen een hoge-precisie He* bundel. Daarom is een bundelopstelling gebouwd waarin één longitudinale en drie transversale laserkoelingssecties (werkend in twee dimensies) gebruikt worden. De uiteindelijke bundel wordt gedefinieerd door een mechanische collimatiesectie, bestaande uit twee kleine diafragma's. Atomen uit een metastabiele helium bron worden achtereenvolgens gecollimeerd, afgeremd, gefocusseerd en gecomprimeerd door de laserkoelingssecties. Dit resulteert in een smalle (25 $\mu$m diameter), langzame (247 ms$^{-1}$), monochromatische (1.5% rms snelheidsspreiding) en ultra-gecollimeerde (36 $\mu$rad rms divergentie) He* bundel. De bundelflux bedraagt doorgaans zo'n 250 s$^{-1}$, hetgeen genoeg is voor de experimenten die in dit proefschrift beschreven worden. Zonder de drie transversale laserkoelingssecties zou de bundelflux op ongeveer 2 atomen per uur uitkomen. Dan zouden experimenten, die nu maar 5 minuten duren, zo'n 4 jaar oftewel een volledige promotieduur in beslag nemen! In dit proefschrift gebruiken we de helium $\{2s\}^3S_1 \rightarrow \{2p\}^3P_2$ overgang, bij een golflengte van $\lambda = 1083$ nm, voor zowel de atoomoptica als ook voor het laserkoelen. Het 1083 nm licht wordt geproduceerd door laserdiodes.

Een metastabiel helium atoom dat een 1083 nm foton absorbeert of uitzendt, zal zijn snelheid met de recoilsnelheid $v_R = 0.092$ ms$^{-1}$ veranderen. Hierdoor verandert de bewegingstoestand van het atoom. De resulterende afbuiging van het atoom wordt, met een rms resolutie van $0.13v_R$, waargenomen op een twee-dimensionale positiegevoelige enkele-atoom detector. Deze is 2 m achter het lichtveld geplaatst. De 2D-detector wordt ook gebruikt om de interne toestand van de atomen in de bundel met hoge nauwkeurigheid te meten. Hierbij wordt gebruik gemaakt van een toestandsafhankelijke afbuigingstechniek, gebaseerd op het Stern-Gerlach effect. Het blijkt dat de atoombundel spin-gepolariseerd is zolang de atomen in voldoende mate "magnetisch geleid" worden. Het is mogelijk om zowel een pure bundel van $m = 0$ atomen maken als ook een pure bundel van $m = -1$ atomen, waarin $m$ het magnetisch quantumgetal is. Het combineren van de $m = -1$ bundel met $\sigma^-$-gepolariseerd laserlicht resulteert in een effectief twee-niveau systeem.

Een atoom dat spontane emissie ondergaat, zal een foton in een willekeurige richting uitzenden. De hoekverdelingsfuncties voor dipoolstraling zijn volgens de theorie anisotroop. Bovendien hangen ze af van de polarisatie van het uitgezonden foton. Een $\pi$-overgang heeft een andere verdelingsfunctie dan een $\sigma$-overgang. In dit proefschrift worden beide verdelingsfuncties, voor het eerst, onafhankelijk van elkaar gemeten. In het experiment wisselwerkt de atoombundel met een zwakke lopende lichtgolf, waardoor een gedeelte van de atomen spontaan een foton uitzendt. De terugslag door het uitgezonden foton zorgt ervoor dat de atomen afgebogen worden. De resulterende afbuigingspatronen worden gemeten met behulp van de 2D-detector. De afbuigingspatronen geven eenduidig de ruimtelijke hoekverdelingsfuncties voor dipoolstraling weer. Om de $\pi$- en de $\sigma$-overgangen van elkaar te scheiden, wordt gebruik gemaakt van een toestandsafhankelijke afbuigingstechniek, gebaseerd op het Stern-Gerlach effect.

In het laatste experiment is niet de spontane emissie kracht maar de dipoolkracht dominant. Nu wisselwerkt de atoombundel met een van resonantie verstemde staande lichtgolf. De koude atomen in de bundel, die zich als vlakke atomaire golven gedragen, ondervinden diffractie aan de periodieke dipoolpotentiaal. Hierdoor wordt elk atoom in een coherente superpositie van twee bewegingstoestanden gebracht, mits het experiment in het Bragg-regime uitgevoerd wordt. De staande lichtgolf gedraagt zich dan als een coherente bundelsplitser voor atomen: elk "gesplitst" atomair golfpakket beweegt langs twee ruimtelijk gescheiden paden tegelijkertijd. The vertakkingsverhouding kan geregeld worden met de intensiteit van de staande golf. In het experiment wordt Bragg scattering tot en met de achtste orde gerealiseerd. Dit resulteert in een regelbare coherente bundelsplitser voor atomen met een maximale splitsingshoek van 5.9 mrad. Op de 2D-detector zijn de beide paden dan zo'n 12 mm gescheiden. Atomen die spontane emissie ondergaan gedurende Bragg scattering kunnen op de 2D-detector worden herkend door de willekeurig gerichte terugslag. Zij kunnen dan selectief uit de metingen verwijderd worden. In de toekomst zou men drie van deze Bragg bundelspliters kunnen gebruiken om een atoominterferometer te bouwen met een groot omvat oppervlak tussen de armen en een macroscopische scheiding van de paden.

De experimenten die in dit proefschrift beschreven worden, laten zien dat de He* bundelopstelling gebruikt kan worden voor atoomoptica experimenten. Hierbij wordt een resolutie gerealiseerd die vergelijkbaar is met die van BEC experimenten. Bovendien is de bundelopstelling bijzonder geschikt voor toekomstige cavity QED experimenten, waarin het atoom het lichtveld moet passeren binnen de cavity-dempingstijd.

# Dankwoord

Hier wil ik alle mensen bedanken die aan de totstandkoming van dit proefschrift hebben bijgedragen en die de afgelopen 4 jaar tot zo'n gezellige tijd hebben gemaakt. Als ex-Delftenaar/Limburger kon ik geen betere vakgroep treffen dan AQT/B (het voormalige AOW) in Eindhoven. De informele sfeer en de Brabantse gezelligheid staan hier nog hoog in het vaandel en maken deze groep tot een fantastische werkomgeving.

Allereerst bedank in mijn promotoren en copromotor, Herman Beijerinck, Boudewijn Verhaar en Ton van Leeuwen.

Van Ton van Leeuwen heb ik de afgelopen jaren het meest op het gebied van de natuurkunde (en computers) geleerd. Hij lijkt over een onuitputtelijke hoeveelheid (fysisch en non-fysisch) inzicht te beschikken, zodat elk probleem simpel leek nadat ik er met Ton over gediscussieerd had. Ook wanneer de fysica een beetje tegenzat, wist hij altijd met zijn enthousiasme het tij weer te keren. Voor deze zeer aangename samenwerking ben ik hem veel dank verschuldigd.

Ook wil ik Herman Beijerinck bedanken voor zijn vele hulp. Zijn brede kijk op zowel fysica als ook non-fysica heeft mij enorm gestimuleerd gedurende de afgelopen 4 jaar.

Verder ben ik Edgar Vredenbregt dankbaar voor al zijn advies, waardoor veel werk een stuk sneller ging.

Veel dank ben ik verschuldigd aan Rien de Koning, voor zijn uiterst kundige CAD-tekenwerk en hulp bij vele technische problemen, en Louis van Moll voor de algemene technische ondersteuning. De jaarlijkse barbecue bij Rien is een begrip geworden binnen de groep.

Jo Hermans bedank ik voor zijn kundige en originele kijk op veel fysische problemen. Simon Kuppens bedank ik voor zijn vele waardevolle opmerkingen tijdens de werkbesprekingen.

Herman Batelaan's enorme enthousiasme en vermogen om ingewikkelde fysica doeltreffend en eenvoudig te verwoorden heb ik zeer op prijs gesteld.

I would also like to thank Luxian Tian for the work she did on our setup during her stay in Holland.

Ook ben ik onze secretaresses Rina Boom en Marianne van den Elshout zeer dankbaar voor alle administratieve rompslomp die ze mij uit handen genomen hebben.

Hierbij wil ik tevens Ad Kemper bedanken, voor zijn hulp bij het bedenken en maken van vele elektronische schakelingen, en de mannen van de werkplaats voor de vele onderdelen die zij vervaardigd hebben voor de bundelmachine.

In het lab ben ik bijgestaan door de afstudeerders Boris Habets, Ronald Cornelussen en Geert Jansen. Ik ben hen zeer dankbaar voor het vele werk dat zij verricht hebben en de plezierige tijd tijdens het samenwerken. Datzelfde geldt ook voor de stagiairs Abdel Nnafie, Bart Smeets en Henk Vocks.

Zonder de volgende AIO's/OIO's was onze groep nooit zo gezellig geweest:
Roel Knops, QND'er vanaf het allereerste begin, die mij met de charmes van Stratum-seind bekend maakte.
Kamergenoot Sjef Tempelaars, alias dj Sjef Pils, die bij het woord beatfrequentie niet meteen aan lasers denkt.
Patrick Sebel, die een verdieping lager de Scepter zwaaide.
Roel Bosch, meest recente lid van het "AIO-overleg", waarbij we nooit aan overleggen toegekomen zijn.

Tenslotte wil ik Brigitte, mijn ouders en de ouders van Brigitte bedanken voor hun steun gedurende de afgelopen 4 jaar.

# Curriculum Vitae

**2 juni 1973**      Geboren te Heerlen

**1985-1991**      Ongedeeld VWO,
Coriovallum College te Heerlen

**1991-1996**      Studie Technische Natuurkunde,
Technische Universiteit Delft,
doctoraal examen (cum laude) mei 1996

**1996-2000**      Onderzoeker-In-Opleiding bij Stichting FOM,
werkgroep AQ-E-a,
Experimentele Atoomfysica en Quantumelektronica,
Faculteit Technische Natuurkunde,
Technische Universiteit Eindhoven